ELASTIC AND INELASTIC SCATTERING OF FAST NEUTRONS BY ^{6}Li, ^{7}Li, ^{9}Be, AND ^{12}C

by

Henry Harlan Hogue

Department of Physics
Duke University

Date: _____

Approved:

_____
Henry W. Newson, Supervisor

_____

_____

_____

_____

Dissertation submitted in partial fulfillment of the requirements for the degree of Doctor of Philosophy in the Department of Physics in the Graduate School of Duke University

1977

ABSTRACT

(Physics-Nuclear)

ELASTIC AND INELASTIC SCATTERING OF FAST NEUTRONS BY ^{6}Li, ^{7}Li, ^{9}Be, AND ^{12}C

by

Henry Harlan Hogue

Department of Physics
Duke University

Date: _____

Approved:

_____
Henry W. Newson, Supervisor

_____

_____

_____

_____

An abstract of a dissertation submitted in partial fulfillment of the requirements for the degree of Doctor of Philosophy in the Department of Physics in the Graduate School of Duke University

1977

Differential neutron cross section data for elastic and discrete inelastic scattering by ^{6}Li, ^{7}Li, ^{9}Be, and ^{12}C in the 7-15 MeV energy range have been obtained. These data are of importance for nuclear fusion reactor design. Most of the data have been analysed in potential scattering models.

Optical model analyses of the ^{6}Li, ^{7}Li, and ^{9}Be elastic scattering data were performed to obtain the symmetry-energy terms in the optical model potential strengths for light nuclei. These terms are related to the isospin dependence of the nuclear force. The results were shown to be consistent with the symmetry terms extracted from nucleon scattering by heavier nuclei. However, a direct comparison of neutron and proton scattering by ^{9}Be indicated either that the Coulomb-energy terms in the potential strengths are larger for that nucleus than for heavier nuclei or that core-coupling effects are important.

Coupled-channels calculations were performed for the elastic and inelastic ^{9}Be and ^{12}C data. Good fits were obtained using a rotational model for the excited states. A comparison of neutron and proton scattering in the coupled-channels model gave symmetry-energy terms consistent with those obtained for nucleon scattering by heavier nuclei. No difference in the quadrupole deformation parameters for neutron and proton scattering by ^{9}Be was observed.

TABLE OF CONTENTS

Appendix

LIST OF ILLUSTRATIONS

LIST OF TABLES

ACKNOWLEDGEMENTS

I wish to express my appreciation to the many past and present members of the Neutron Time-of-Flight Group at the Triangle Universities Nuclear Laboratory and the support staff for their assistance in obtaining the neutron scattering data described herein. In particular, I wish to thank my advisor and TUNL director, Dr. H. W. Newson, and deputy TUNL director, Dr. E. G. Bilpuch, for giving me the opportunity to work with the Time-of-Flight program as a graduate student at Duke.

Dr. D. W. Glasgow was chiefly responsible for the design and construction of the time-of-flight spectrometer. He and Dr. F. O. Purser directed its installation at TUNL. The computer program for data acquisition was written by Dr. J. C. Clement. I wish to thank these three for their guidance at various times during the data-taking, data-reduction, and data-correction phases of the present work. I am grateful to Dr. C. R. Gould for similar guidance and for providing direction in performing the optical model and coupled-channels analyses of the data.

Finally, I wish to thank those who helped with the production of the manuscript, especially, Mrs. Dorothy "Mike" Bailey, who drew the illustrations; Mr. David Turner, who photographed them; and my wife Brenda, who punched many

computer cards to produce the text and who has provided support in many other ways throughout my years of graduate study.

This work was supported by the United States Energy Research and Development Administration.

H. H. H.

CHAPTER I

INTRODUCTION

An extensive set of differential cross section data for neutron elastic and discrete inelastic scattering of 7-15 MeV neutrons by ^{6}Li, ^{7}Li, ^{9}Be, and ^{12}C were obtained at TUNL in the 3-year period 1974-7. Table 1 provides a summary of these data, some of which have been published[1,2]. Most of the data have been analysed in direct scattering models with good success. The experimental techniques and procedures and the procedures and results of the analyses are described here in detail.

The motivation for undertaking the work was two-fold. High quality fast neutron scattering data for a variety of materials, including most of the p-shell nuclei, are required for fusion reactor design applications. Also, because neutrons do not interact with nuclei through the Coulomb force, they are excellent probes for studying properties of the nuclear force and nuclear structure. When combined with the results of proton scattering studies in the framework of the optical model, neutron scattering provides information relating to the isospin dependence of the nuclear force. The simultaneous analysis of elastic and inelastic scattering in a coupled channels optical model formalism gives information related to the nuclear deformation.

TABLE 1

SUMMARY OF NEUTRON DIFFERENTIAL

CROSS SECTION DATA[a]

Element	Cross Section	No. of Energies	Energy Range(MeV)
^{6}Li	Elastic	7	7.5-14
^{6}Li	Inelastic 2.18-MeV state	7	7.5-14
^{7}Li	Elastic plus 0.48-MeV state	8	7-14
^{7}Li	Inelastic 4.63-MeV state	6	9-14
^{9}Be	Elastic	8	7-14
^{9}Be	Inelastic 2.18-MeV state[b]	8	7-14
^{12}C	Elastic	15	9-15
^{12}C	Inelastic 4.44-MeV state	15	9-15

[a]Nominally at angles from 25° to 160° in 5° increments.
[b]May contain contributions from other nearby states for the higher bombarding energies.

The various partial neutron cross sections for lithium, beryllium, and carbon rank high on priority lists of required data for use in the design of nuclear fusion reactors. However, at present there are few neutron facilities capable of measuring these partial neutron cross sections in the 7- to 14-MeV energy range. The neutron time-of-flight spectrometer at TUNL combined with the Cyclc-Graaff installation provides a capability for making measurements of the required neutron elastic and inelastic scattering cross sections accurate to a few percent.

It has been possible for some years to make measurements of proton elastic and inelastic scattering accurate to the few-percent level. As a result, quality proton scattering analyses have been carried out for most of the stable nuclei, including the p-shell nuclei studied here. The optical model of elastic scattering(OM) and its extension to include low-lying excited states in a coupled-channels treatment(CC) have been favorite tools employed in such analyses due to their simplicity. A motivation for repeating some of these analyses using neutrons rather than protons as the probe is apparent when one recalls that, in the isospin formalism, neutrons and protons are but different isospin states of the same particle. Thus, through analysis of both neutron and proton elastic scattering results, information is obtained which bears directly upon the isospin-dependent part of the nuclear potential.

The CM has been very successful for the A>40 nuclei. Several papers have described nucleon scattering for broad regions in target mass and projectile energy using potentials for which the parameters vary smoothly with mass and energy. The analysis by Becchetti and Greenlees[3] is the most commonly cited of these. Other common parameter sets are listed in the parameter compilation of Perey and Perey[4]. These analyses will be referred to collectively as the "A>40 analyses".

In most cases elastic scattering by a given light nucleus for a given bombarding energy is also well described by a complex potential, but the same potential may poorly describe the scattering from another light nucleus or scattering at a higher or lower energy. Nevertheless, global analyses for light nuclei, such as that by Watson et al.[5] for the p shell, have shown that the CM does describe nuclear scattering by light nuclei in an average way. Furthermore, the parameters of the CM potential obtained in the Watson analysis were comparable in magnitude and energy dependence with those obtained in the A>40 analyses. For individual nuclei the deviations from the CM predictions that occur may be attributed to structure effects in the light compound nuclei formed.

Watson's analysis was performed using primarily proton data, though some neutron data of poorer quality was available at 14 MeV. The present work provides a test of the results of that analysis for neutron scattering by ^{6}Li, ^{7}Li, and ^{9}Be. For

these nuclei, no pronounced resonance structure was indicated in neutron scattering over the 7- to 14-MeV energy region covered. Success in analysis of these neutron data would lend further support to the applicability of the CM for p-shell nuclei and, in turn, give weight to the isospin-dependence results obtained through comparison of the neutron and proton data using that model.

The coupled-channels calculations performed in the present work employed the rotational model of Tamura[6,7]. Neutron scattering from ^{9}Be and ^{12}C were analysed. The aim of the ^{12}C analysis was to further support the rotational picture for that nucleus by extending a previous analysis for a single neutron energy to the 7-14 MeV energy region. The ^{9}Be analysis presented an opportunity to search for a measurable difference in the deformation parameters for neutron and proton projectiles. A comparison of the results of that analysis with a previous ^{9}Be proton analysis performed using the same model was made.

CHAPTER II

EXPERIMENTAL DETAIL

The experimental apparatus and method for acquiring the differential cross section data in the present work are described in this section. A pulsed neutron source was produced by bombarding a deuterium gas target with a chopped and bunched deuteron beam from the TUNL tandem Van de Graaff accelerator. Neutrons scattered by various sample materials were detected and energy analysed in a time-of-flight spectrometer-goniometer system. This consisted of a single, well-shielded, liquid scintillation detector mounted on an angular carriage with associated electronics for neutron flight-time measurement and n-γ discrimination. Angular distributions were obtained for elastic scattering and for scattering to low-lying excited states of the target materials studied. Absolute differential cross sections were obtained by normalizing the measured yields to those obtained by scattering from hydrogen in the same experimental arrangement. Polyethylene was used for the hydrogen scatterer.

Neutron Source

Operation of the neutron spectrometer required a pulsed neutron flux. This was produced by bombarding a deuterium gas target with a chopped, bunched, and accelerated deuteron beam.

Fig. 1 shows the TUNL Cyclo-Graaff installation, which has been described in ref. 8. The deuteron beam originates at the negative ion source(1), is transported through the chopper-buncher system(2) and the tandem Van de Graaff accelerator(3), and is delivered to the neutron target room(4), where the gas target and time-of-flight spectrometer are located.

The ion source is a direct-extraction negative ion source capable of producing a 50 μa DC beam of negative deuterium ions. A standard HVEC RF chopper sweeps this beam across a 0.375 inch diameter aperture at a frequency of 2 MHz. Retrace pulses are removed by an auxiliary chopper. A two-gap klystron buncher bunches the chopped beam to bursts of about 2 ns FWHM at the target.

The HVEC FN tandem Van de Graaff accelerator can run terminal voltages of up to 8 MV routinely; however, the present experiments required terminal voltages up to 6 MeV only. The positive beam from the accelerator output was transported through two 90° and one 70° bending magnets to the neutron target room. Typically, accelerated beams of 2 μa average current were delivered to the target with 90% transmission through the beam transport system from the tandem high energy extension.

Care was taken to minimize beam-related background and source contamination. The target area was separated from the accelerator and analysing magnets by two concrete shielding walls. The final section of the beam tube and beam collimators

Fig. 1. Floor plan of the Cyclo-Graaff laboratory. Circled numbers indicate the locations of the negative ion source(1), the chopper-buncher system(2), the tandem Van de Graaff accelerator(3), and the neutron target area(4).

Cyclo-Graaff Laboratory

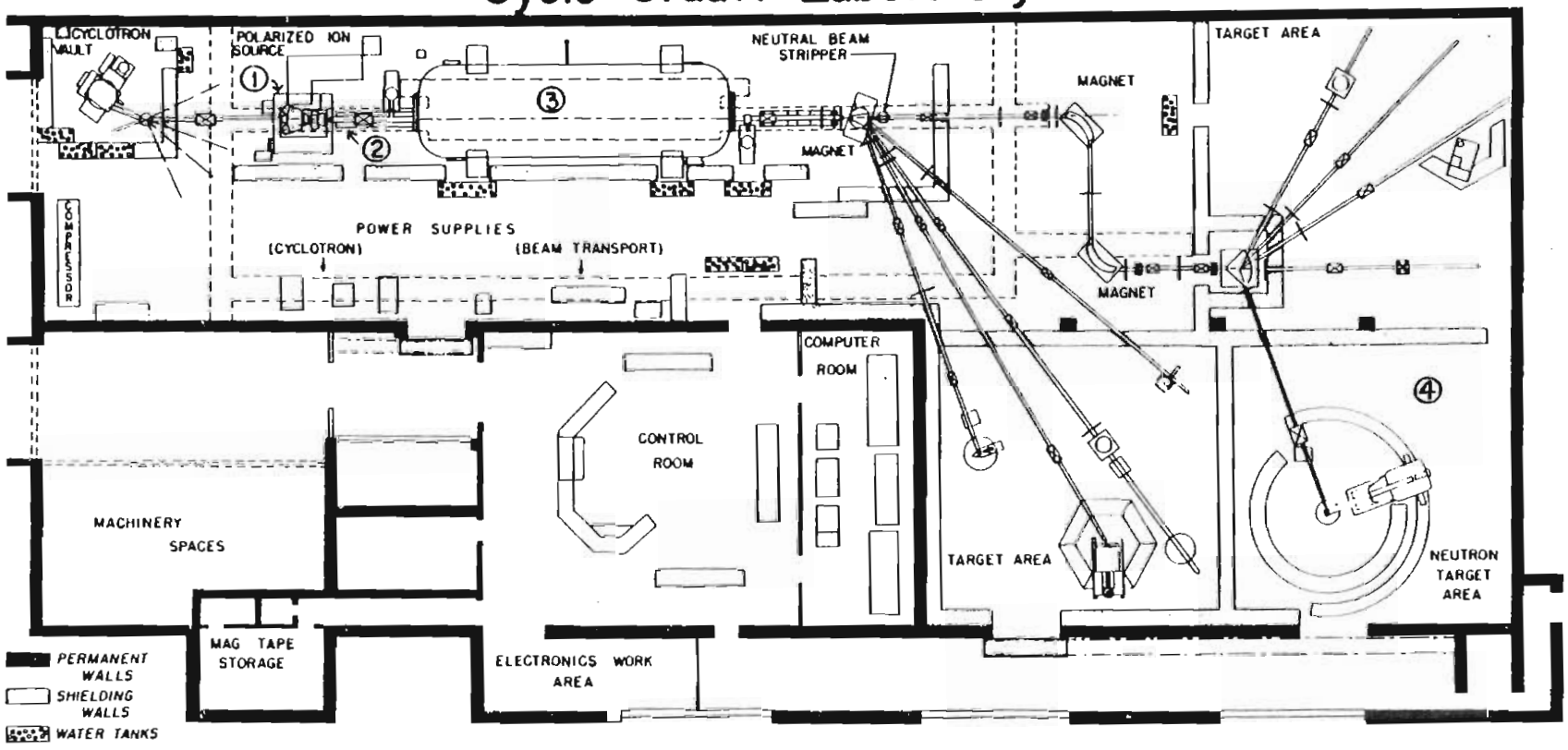

were made of tantalum, for which the (d,n) cross section is small. The beam line was pumped to about 10^{-8} torr in the target area using a turbomolecular pump. Buildup of hydrocarbon contamination on the gas cell entrance foil and collimators was prevented by the good vacuum, cryogenic trapping between the turbomolecular pump and gas cell, and the use of an all metal and ceramic beam tube.

Fig. 2 shows the deuterium gas target assembly. It was constructed of thin-walled stainless steel with care taken to minimize the amount of structural material. As a result, the number of neutrons scattered into the sample from points near the neutron production site is insignificant. To minimize production of neutrons by (d,n) reactions on other than the target gas, a tantalum cell liner and a tantalum beam stop were used. The beam entrance window was made of 3.5μ thick molybdenum foil. A single indium metal "C" ring sealed the foil to both the gas cell and the beam tube. Stainless steel capillary tubing connected the cell to a gas filling system.

Gas cell liners, beam stop, and entrance foil were replaced prior to each week-long run period. Components were cleaned of surface hydrocarbons prior to assembly by immersion in baths of HF and NaOH. The cell was pressurized to 30 psia using high-purity deuterium gas bled through a coil immersed in liquid N_2. This procedure prevented any hydrocarbon contamination which might be present in the gas from reaching the cell.

Fig. 2. Deuterium gas target for neutron production. The deuteron beam enters the cell through the molybdenum foil and produces neutrons through D(d,n) reactions with the deuterium gas. The cell liner and beam stop are made of tantalum for reasons explained in the text.

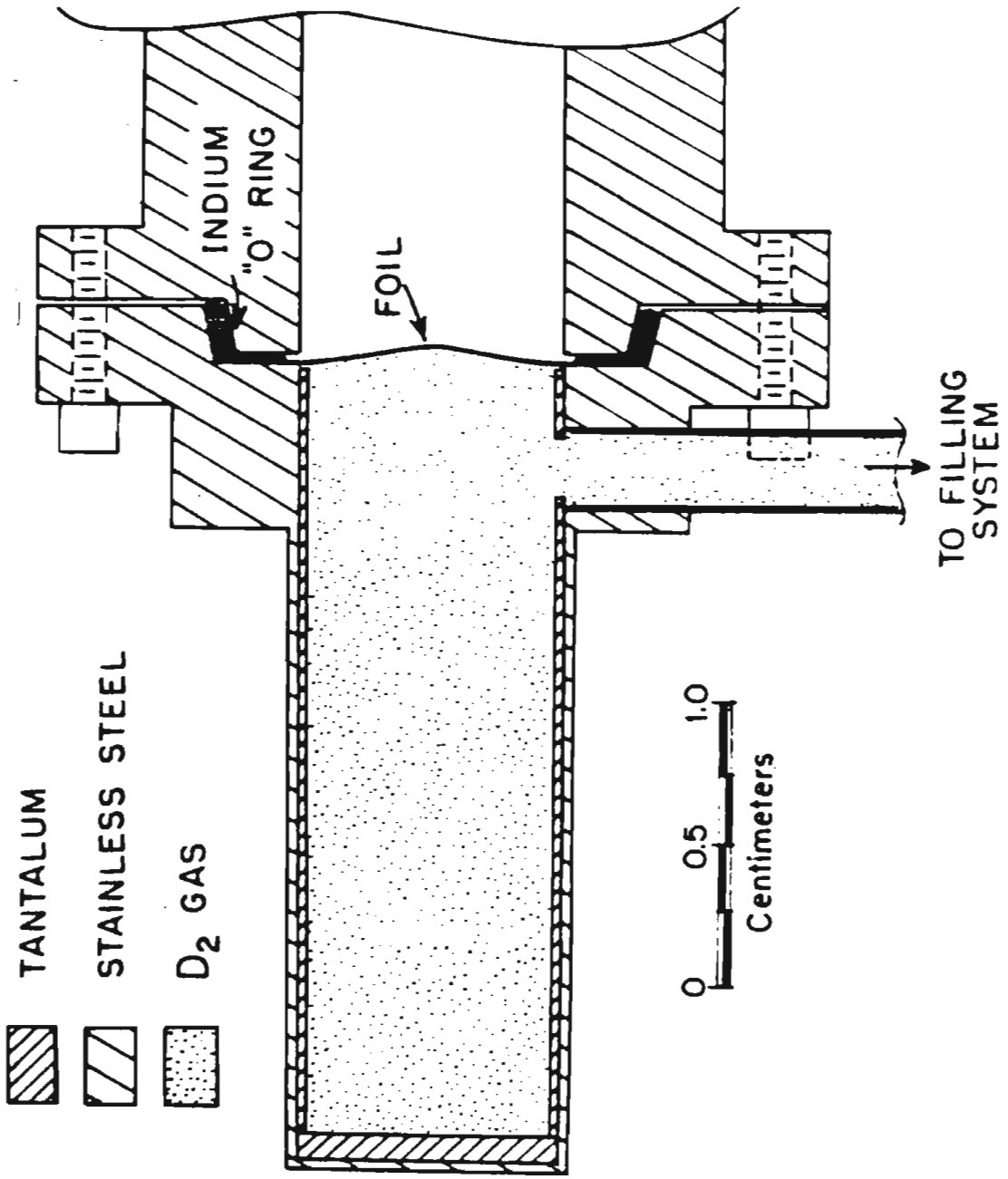
INDIUM "O" RING
FOIL
TO FILLING SYSTEM
TANTALUM
STAINLESS STEEL
D_2 GAS
0
0.5
1.0
Centimeters

With a deuterium beam of 2 μa incident on the cell, the D(d,n)^{3}He reaction gave about 10^8 neutrons/sec/cm^2 at the sample located 8 cm away. Below a deuteron energy of 6 MeV no other neutron-producing reactions contributed to the source flux. Above that energy, break up of deuterons on the deuterium gas and cell materials became significant.

Fig. 3 shows energy spectra for neutrons produced at 0° with respect to the deuteron beam direction. These were obtained from time-of-flight spectra using the spectrometer system to be described below. The energies for the primary D(d,n)^{3}He groups are 14, 11, and 8 MeV in spectra (a), (b), and (c), respectively. These groups are very much broadened in the figure due to the energy resolution of the time-of-flight spectrometer. The average energy spreads(FWHM) in the D(d,n)^{3}He groups ranged from 0.2 MeV at 7 MeV to 0.1 MeV at 15 MeV. The energy difference between the primary group and the highest energy of the break-up continuum [large group at left in spectra (a) and (b)] is about 7.4 MeV. This difference was sufficiently large that elastic scattering of the continuum produced background under the inelastically scattered D(d,n)^{3}He groups only for scattering Q values less than about -6 MeV.

Another feature of the source spectra was a "plateau" which began to form between the primary neutron group and the continuum for the higher primary neutron energies run. This is apparent in spectrum (a) of fig. 3. The feature is produced by

Fig. 3. Typical energy distributions of neutrons from the D(d,n) source. Spectrum (a) is for 14 MeV mean neutron energy in the D(d,n)^{3}He group; spectrum (b), 11 MeV; and spectrum (c), 8 MeV. Neutrons from deuteron break up appear at the left in spectra (a) and (b). A small contaminant group from (d,n) reactions on carbon appears about 5 MeV down from the D(d,n)^{3}He group in each of the spectra.

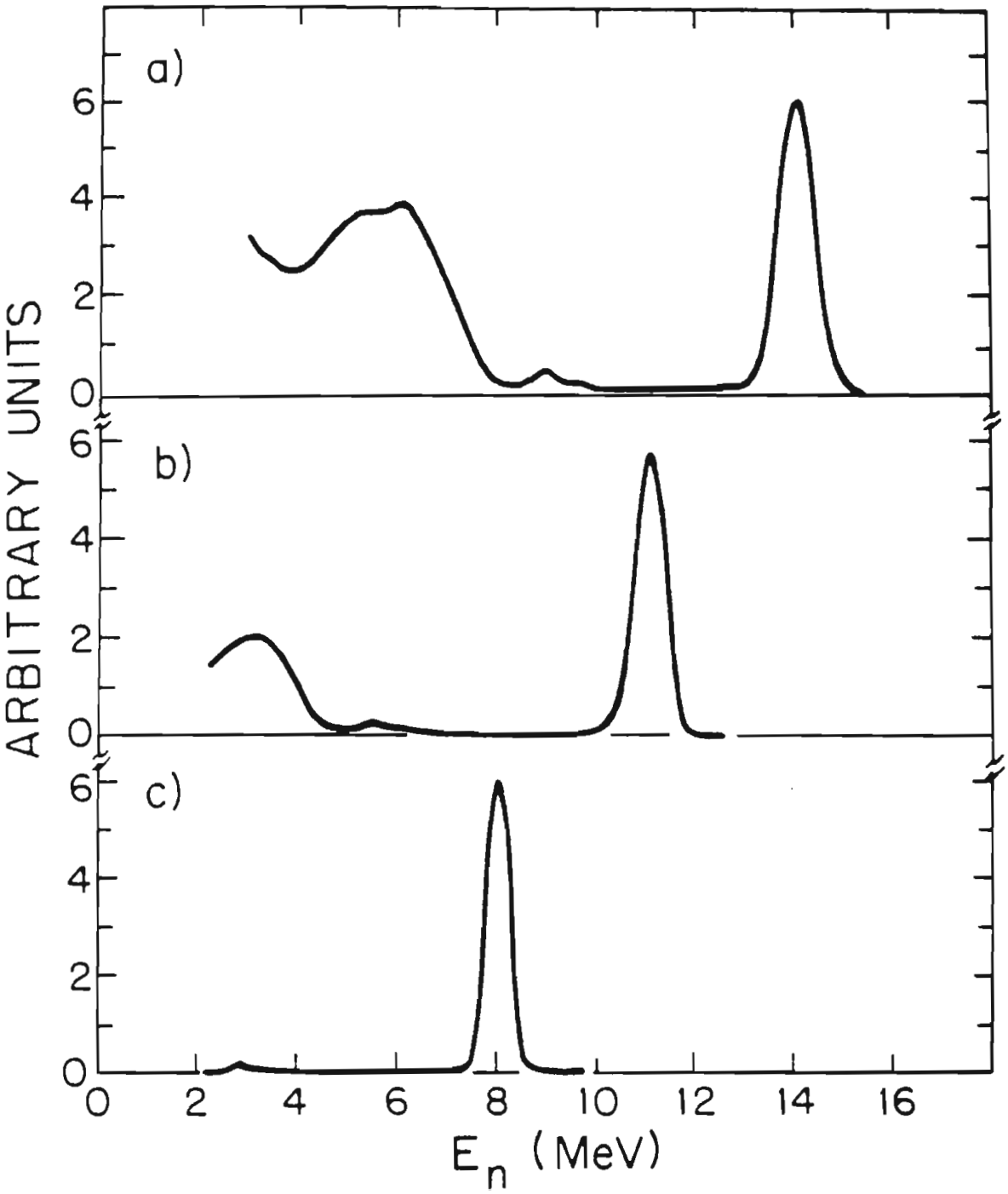
a)
b)
c)
ARBITRARY UNITS
0
2
4
6
0
2
4
6
8
10
12
14
16
E_n (MeV)

D(d,n)^{3}He reactions with deuterium gas driven into the tantalum beam stop. This produced background in the scattering spectra also.

Of course, source-related background in the scattering spectra from "drive-in" or "continuum" neutrons can not be removed by background runs with sample removed. In general, additional background runs with gas removed are required. For the present experiments, however, such runs were avoided. The method used for removing the residual background will be explained in section III.

Time-of-Flight Spectrometer

The time-of-flight spectrometer has been described in two publications [9,10]. Briefly, it consists of a 2-inch thick by 3.5-inch diameter NE218 liquid scintillator coupled to a Phillips 58DVP photomultipler and housed inside a 5-ton shield of paraffin, lithum carbonate, copper, and lead. Fig. 4 is a schematic diagram of the spectrometer and the experimental geometry. Double-truncated conical collimators in the detector entrance channel are designed to permit the detector to view the scatterer but as little as possible of the air space about it while minimizing scattering from its own walls into the detector. A shadow bar consisting of approximately 240 pounds of tungsten metal is used to shield the detector and the collimator throat from direct-source neutrons. The copper preshield shown in the diagram was added during the course of

Fig. 4. Schematic diagram of the neutron detector sheilding and collimation systems showing the experimental gecmetry for the scattering studies.

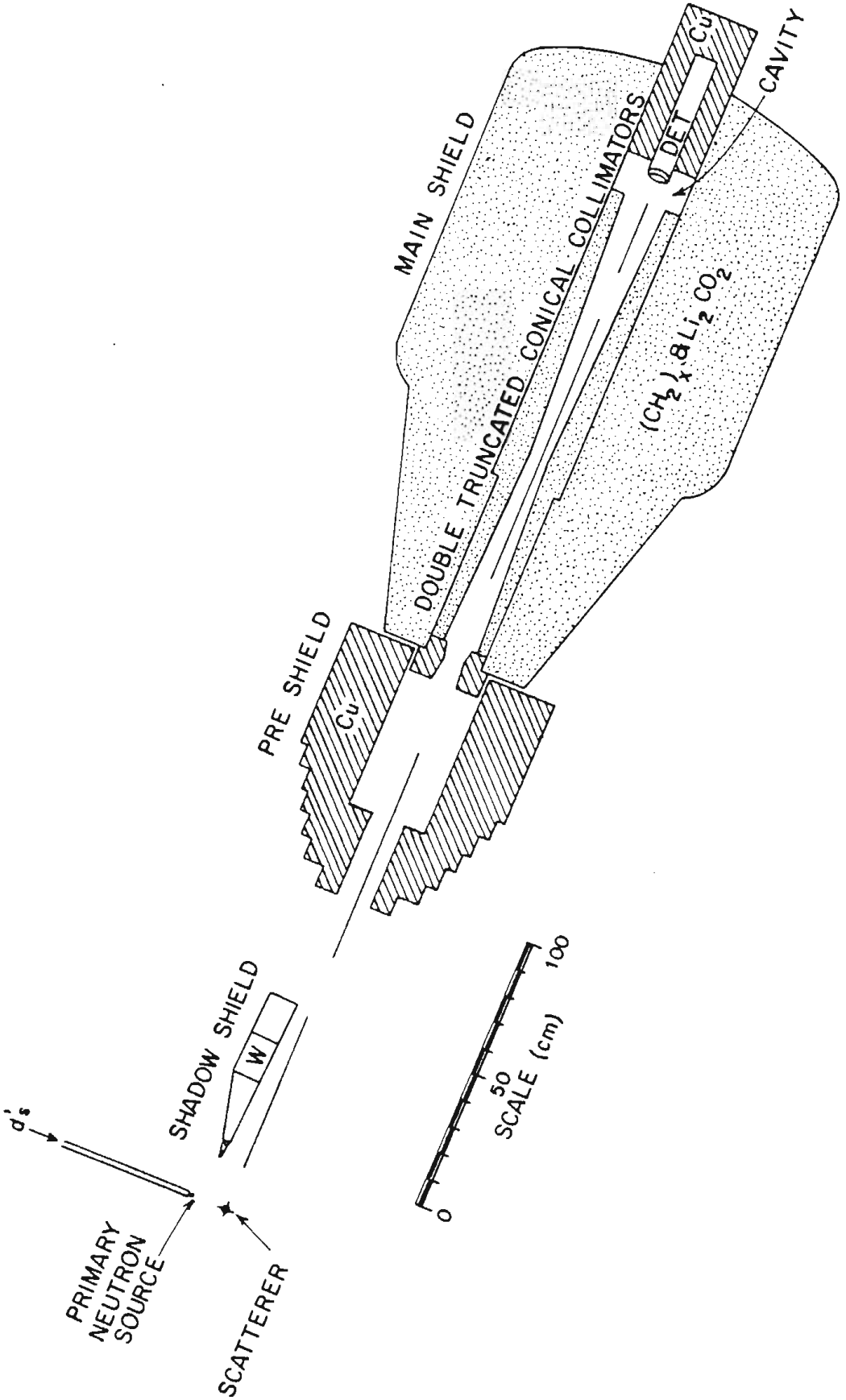
d's
PRIMARY NEUTRON SOURCE
SCATTERER
SHADOW SHIELD
W
PRE SHIELD
Cu
MAIN SHIELD
DOUBLE TRUNCATED CONICAL COLLIMATORS
DET
Cu
CAVITY
$(CH_2)_x$ 8 Li_2CO_3
0
50
100
SCALE (cm)

the experiments. Its purpose was to shadow sides of the main shield from source neutrons not intercepted by the shadow bar.

The detector and shield rest on precision-machined radial and angular carriages. The radial carriage allows neutron flight paths from approximately 2.5 to 3.9 m. The angular carriage is attached to a goniometer table which permits angles of rotation of the detector about the scattering center to be determined to a precision of better than 0.2°. The angular carriage rolls upon a steel plate leveled to approximately 1 mm variance over the 0° to 160° angular range.

The optimal resolution figure-of-merit (time resolution of beam pulse/flight path) for the spectrometer is about 0.5 ns/m but typically ran slightly higher than this during the present experiments. The average energy spread in the incident neutrons was less than 0.2 MeV. These considerations lead to the following approximate expression for the spectrometer energy resolution. Two scattered neutron groups of energies near E could be resolved in the present experiments if their energy difference in MeV was less than

$$\Delta E = [\ (4\times10^{-2}) + (5\times10^{-4})E^3\ ]^{1/2} \qquad (2.1)$$

Fig. 5 is a plot of ΔE vs. E for later reference .

Two flux monitors are used with the spectrometer. A second detector (2-inch diameter by 2-inch thick NE218 scintillator with Phillips 56DVP phototube and copper shielding) is

Fig. 5. Approximate energy resolution of the time-of-flight spectrometer. The minimum energy difference (ΔE) between two scattered neutron groups which can be resolved is shown vs. scattered-neutron energy E_n.

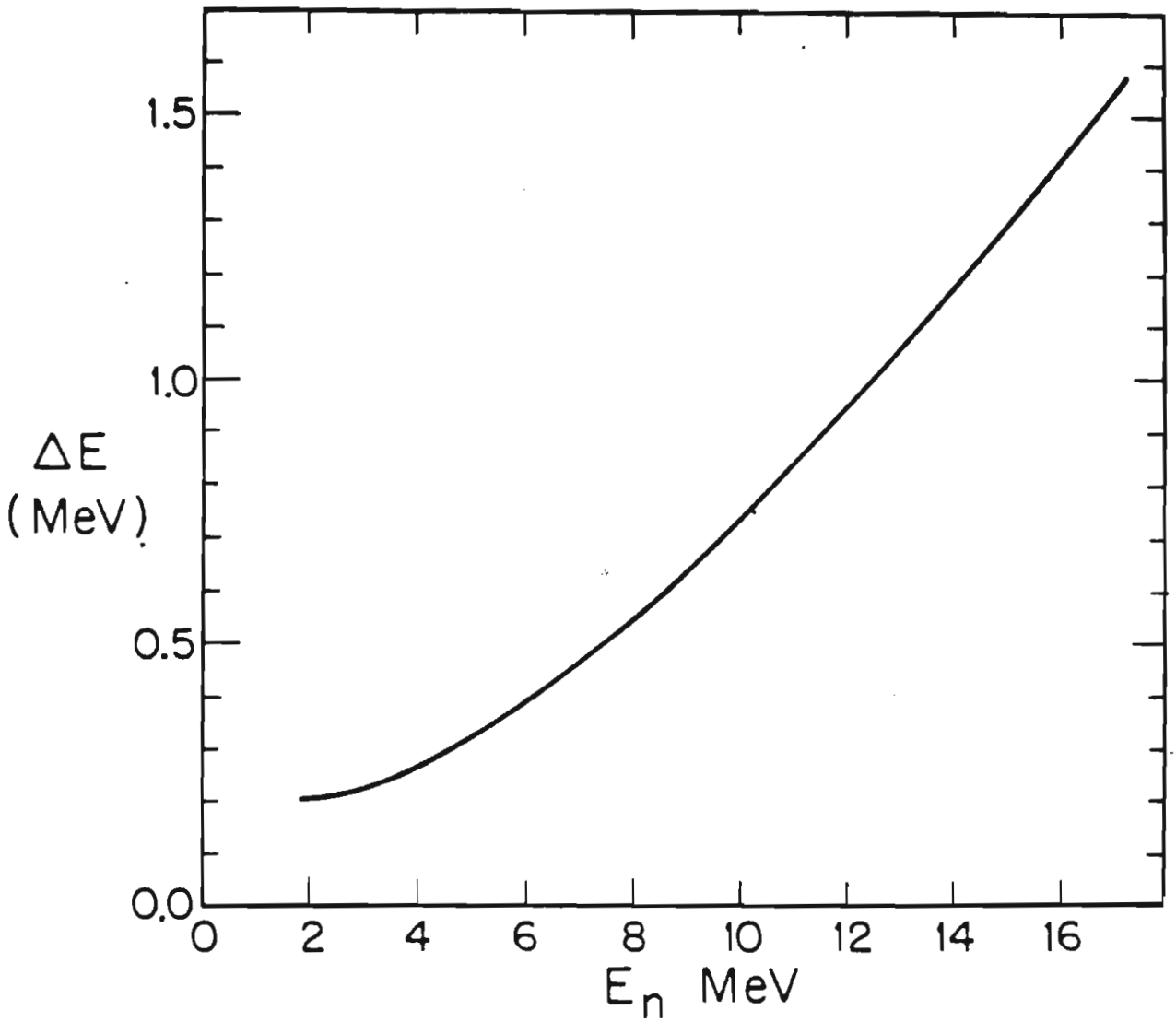
1.5
1.0
0.5
0.0
ΔE
(MeV)
0
2
4
6
8
10
12
14
16
E_n MeV

mounted approximately 2.5 m above the scattering plane viewing the source. The yield in the D(d,n)^{3}He group in this detector during main detector counting intervals is the primary relative measurement of the integrated neutron flux at the sample during the intervals. A secondary flux monitor is provided as a check on the operation of the monitor detector by integrating the charge on the beam stop. For this purpose the gas cell is electrically isolated from the beam pipe and a voltage of about -800 volts is applied to an electron-suppression ring just preceding the cell.

Electronics

The electronic circuitry associated with the spectrometer is diagrammed in fig. 6. There are two essentially identical networks for main and monitor detectors. These networks transform signals from the detectors and pulses from the capacitive beam pulse pick-off loop located before the gas cell into time-of-flight and n-γ discrimination signals.

A fast signal from one of the detector photomultipliers and an amplified, delayed signal from the pick-off are analyzed by constant fraction pulse height (CFPH) discriminators which produce timing signals with minimal jitter and walk. The respective discriminator outputs trigger the start and stop of a time-to-amplitude converter(TAC) to produce the time-of-flight(TOF) signal. The delay in the pick-off branch is adjusted so that a stop signal occurring after a start signal

Fig. 6. Block diagram of the electronics used with the time-of-flight spectrometer. Nearly identical circuits for the main and monitor detectors convert signals from the detectors and from the beam pulse pick off into time-of-flight and n-γ discrimination signals.

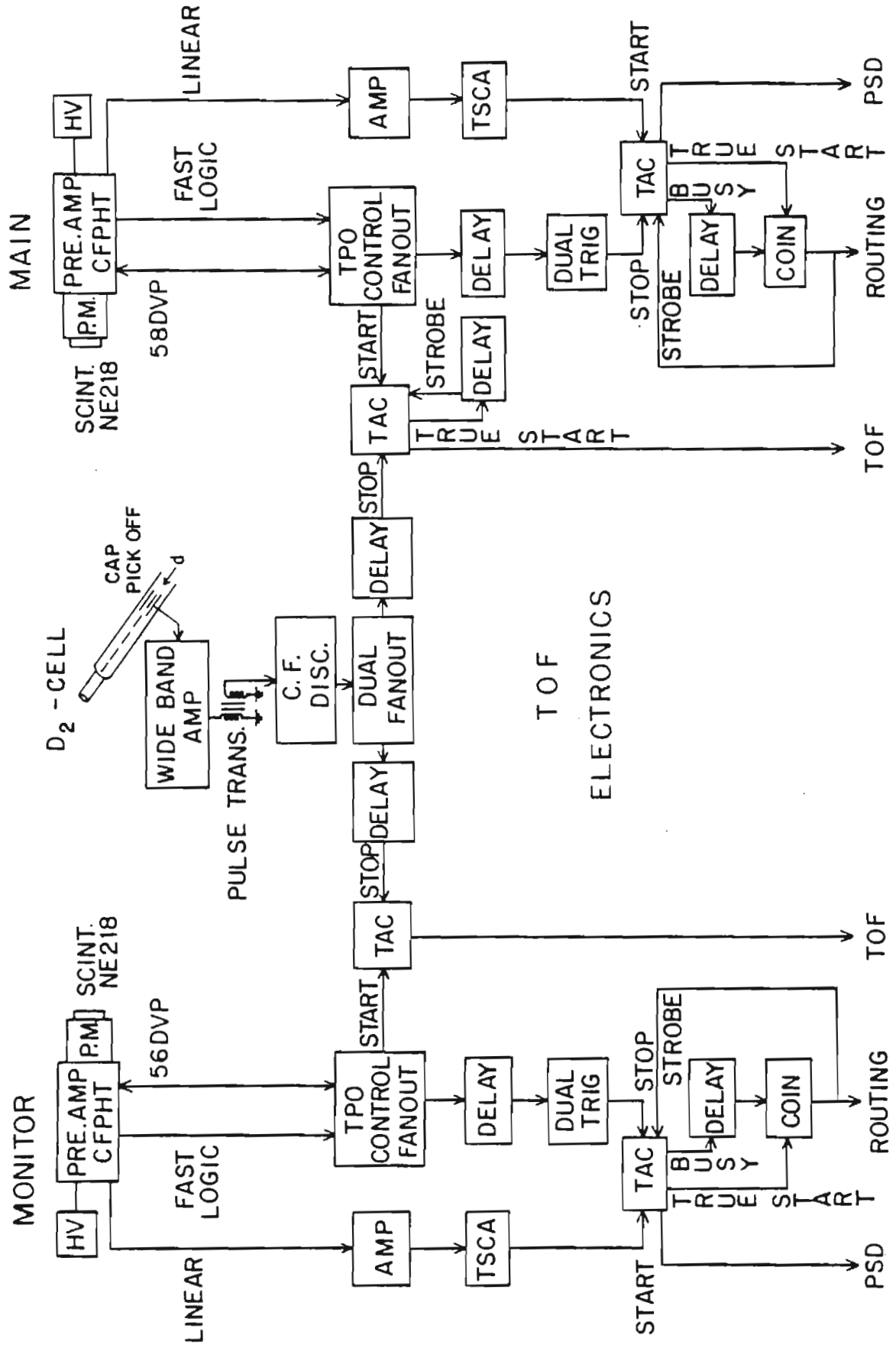
MONITOR
HV
PRE.AMP CFPHT
P.M.
SCINT. NE218
56DVP
FAST LOGIC
LINEAR
AMP
TSCA
START
PSD
TPO CONTROL FANOUT
DELAY
DUAL TRIG
STOP
STROBE
TAC
BUSY
TRUE START
ROUTING
TOF
PULSE TRANS.
WIDE BAND AMP
C.F. DISC.
DUAL FANOUT
D_2 -CELL
CAP PICK OFF
d
TOF ELECTRONICS
MAIN
HV
PRE.AMP CFPHT
P.M.
SCINT. NE218
58DVP
FAST LOGIC
LINEAR
AMP
TSCA
START
PSD
TPO CONTROL FANOUT
DELAY
DUAL TRIG
STOP
STROBE
TAC
BUSY
TRUE START
ROUTING
TOF

from the detector and within the TAC range must have resulted from the beam pulse which produced the neutron or gamma causing the start. This inverted stop-start scheme was chosen to minimize TAC dead time.

Standard pulse shape discrimination(PSD) circuitry is used to distinguish between neutron and gamma events. Briefly, neutrons and gammas give rise to light pulses in the scintillator which decay at different rates. Linear signals from the photomultiplier are passed through a timing signal channel analyser(TSCA) to a delay-line amplifier. The bipolar output of the delay-line amplifier crosses through zero relatively later for neutron than for gamma events. A PSD signal is derived by starting a TAC with the output of the delay-line amplifier and stopping on the delayed fast detector signal. Fig. 7 is a pulse-height distribution of the PSD TAC output. Neutron and gamma events are shown clearly separated.

For the present experiments, the lower level of the TSCA in the PSD network was set to reject linear signals having pulse height smaller than that of the Compton edge of gammas from ^{137}Cs. With this bias, neutrons of energy below about 2 MeV were not detected. The bias was set prior to each week-long data taking period and checked at least once each 24 hours during the period .

A signal labeled ROUTING in Fig. 6 was generated whenever the PSD TAC received a start signal followed by a stop within its range. If this signal did not occur following a TAC

Fig. 7. Typical pulse-height distribution of the pulse shape discrimination signal. By means of a window set to frame the neutron group appearing at the left, time-of-flight signals are sorted into neutron and gamma spectra.

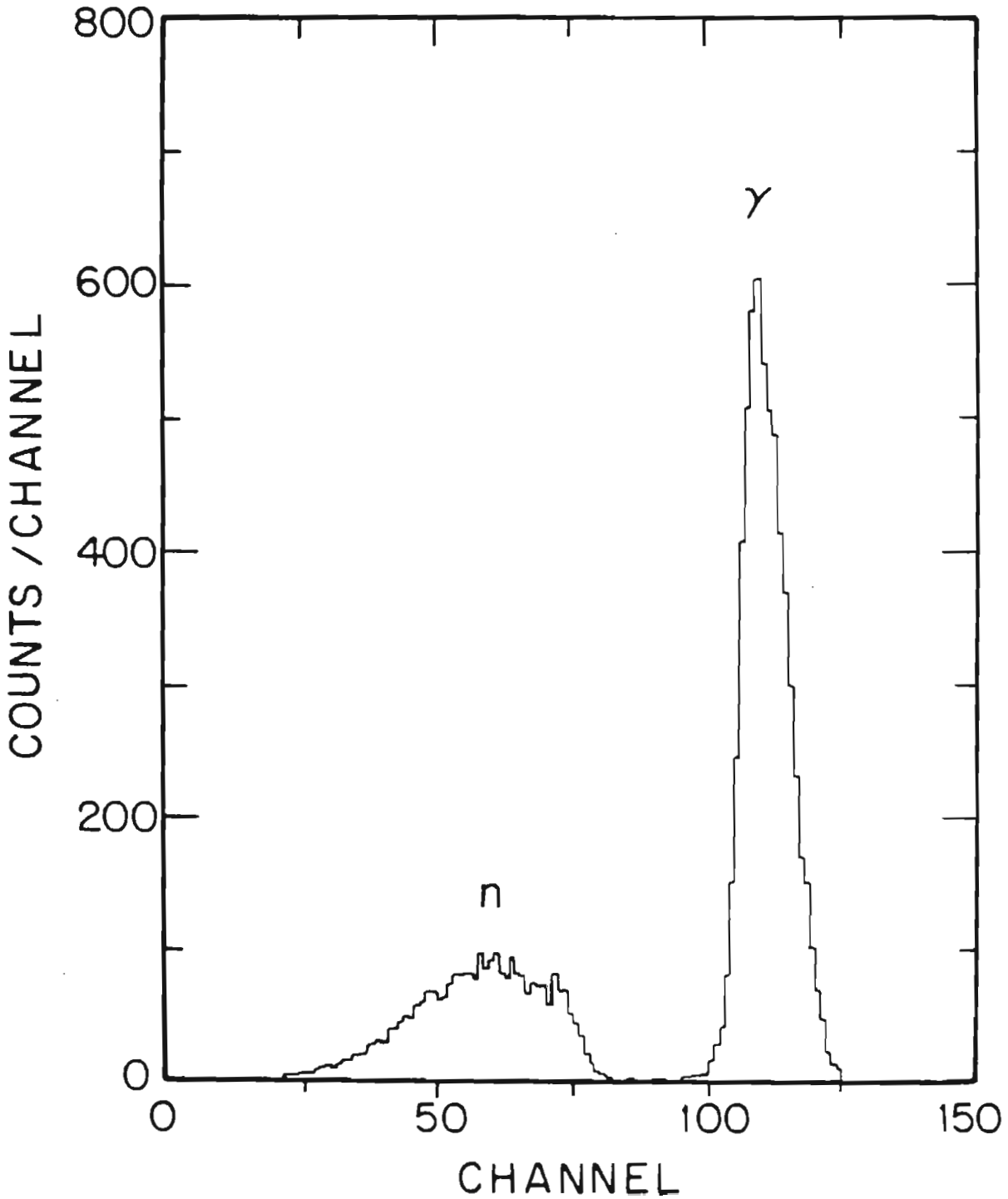
800
600
400
200
0
COUNTS / CHANNEL
γ
n
0
50
100
150
CHANNEL

start, the TAC was reset immediately to avoid unnecessary dead time.

The TOF and PSD signals were sent to separate amplitude-to-digital converters gated by the ROUTING signal and interfaced with a Honeywell DDP224 computer. The computer was programmed to read the ADCs and store events from the main and monitor detectors. Simultaneously, any of the neutron, gamma, or PSD spectra could be displayed on a CRT. A variety of auxiliary operations (e.g., peak summation) could be performed on the spectra without interrupting data acquisition. Spectra for each detector position were dumped on magnetic tape for read-back and analysis off line.

A sample TOF spectrum is shown in fig. 8. This is for 11-MeV primary source neutrons scattered from carbon sample at 30°. Time of flight increases from right to left. Two sharp groups appear in the right half of the spectrum. These are, from right, neutrons elastically scattered and neutrons inelastically scattered leaving ^{12}C in its 4.44-MeV excited state. The neutrons appearing in the left half of the figure are the neutrons produced by deuteron break-up reactions in the gas target and scattered by the sample to the detector.

Samples

Samples used in the present work were ^{12}C (natural graphite) and ^{9}Be, ^{6}Li, and ^{7}Li (metals). All are solids at room temperature; however, only carbon and beryllium could be

Fig. 8. Time-of-flight spectrum of 11 MeV neutrons scattered by carbon to a laboratory angle of 30°. Time of flight decreases from left to right. The groups appearing in the spectrum are discussed in the text.

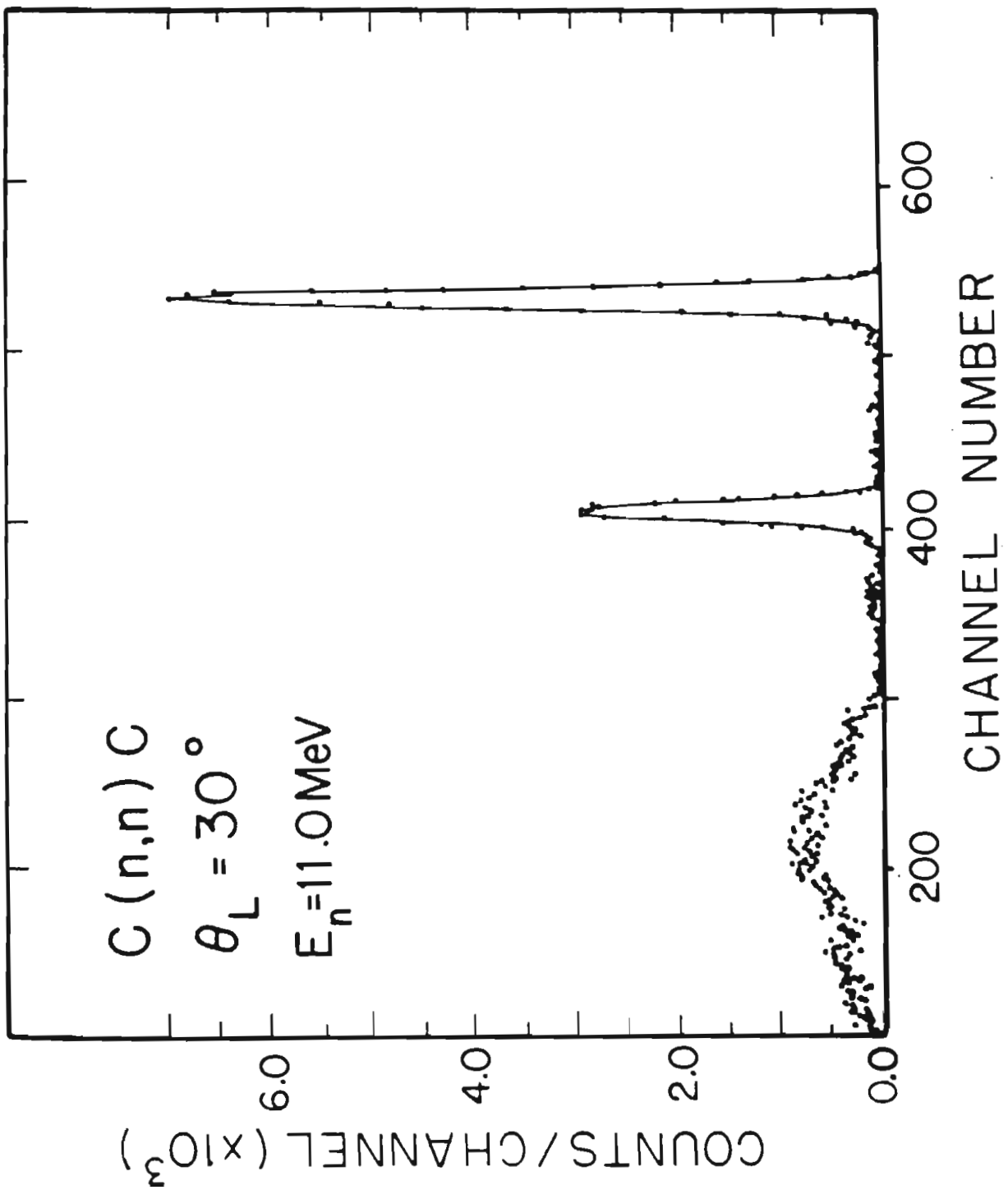
C(n,n)C
θL = 30°
En=11.0MeV
COUNTS/CHANNEL (x10³)
0.0
2.0
4.0
6.0
200
400
600
CHANNEL NUMBER

made into self-supporting samples. Lithium metal is soft and hygroscopic; therefore, samples of ^{6}Li and ^{7}Li obtained from Oak Ridge National Laboratory were encapsulated in thin-walled aluminum cans. An empty aluminum container was provided in order that neutron scattering from aluminum could be removed from the lithium spectra with a background run.

Samples were fabricated as right circular cylinders of approximately 1-inch height and 3/4-inch diameter; however, for carbon a sample having 3/8-inch diameter was used for some of the runs. The polyethylene samples used for normalization of the angular distributions were made very small (about 1/4-inch diameter) in order that finite geometry and multiple scattering corrections would be very small and could be treated analytically. Data on the individual samples are given in table 2.

Samples were suspended at the center of rotation of the detector with their symmetry axes vertical. In order for this to be done the ^{6}Li, ^{7}Li samples and the aluminum blank were fitted with aluminum end caps to which suspension wires were attached. The carbon and beryllium samples were suspended by passing a suspension wire through 0.015-inch diameter holes drilled along their symmetry axes. Friction between suspension wires and samples was sufficient to prevent the samples from sliding on the wires.

TABLE 2

PHYSICAL DATA FOR THE SCATTERING SAMPLES[a]

Sample	Radius (cm)	Height (cm)	Encapsulated[b]	Weight (g)	Principal Contaminant
^{6}Li	0.95	2.54	Yes	3.32	5.0% ^{7}Li
^{7}Li	0.95	2.54	Yes	3.80	-
^{9}Be	0.95	2.54	No	13.38	-
^{12}C #1	0.48	2.48	No	3.04	1.1% ^{13}C
^{12}C #2	0.95	2.54	No	12.50	1.1% ^{13}C
Polyethylene #1 (used with ^{12}C #1)	0.29	2.55	No	0.66	-
Polyethylene #2 (all other samples)	0.30	2.81	No	0.72	-
Al blank[b] (Li background)	0.95	2.54	-	3.10	-

[a] All samples are in the form of right circular cylinders.
[b] Thin-walled aluminum can with end caps for 3.10g total weight of aluminum.

Experimental Procedure

Data were accumulated from 30° to 160° in 10° increments then from 25° to 155° in 10° increments. Such a procedure allowed any slow drifting of detector efficiency to be observed by separating the counts for adjacent angles over a long time period. With the present source-to-sample distance, proper shadowing of the detector from direct-source neutrons cannot be achieved for angles forward of 25°. Also, due to the interference of the detector shield with the beam pipe, angles beyond 160° are inaccessible.

At each detector position, a spectrum was obtained for the sample in place and followed immediately by a background spectrum accumulated with only the sample suspension wire or aluminum blank in place. Each background spectrum was accumulated for a length of time chosen to minimize the net statistical error on the elastic group for the total counting time ("in" count plus "out" count). This was done as follows. During the background counting period a quantity

$$q = \frac{M_o}{M_I}\sqrt{\frac{\frac{C_I}{M_I} + \frac{3}{2}\left(\frac{C_I}{M_I}\right)^2}{\frac{C_o}{M_o} + \frac{3}{2}\left(\frac{C_o}{M_o}\right)^2}} \qquad (2.2)$$

was continually updated. Here C_I and C_o are foreground and background counts, respectively, for the elastic group in the

main detector. Similarly, M_x and M_o are foreground and background counts for the D(d,n)^{3}He group in the monitor detector. When the value of q increased to unity, data collection for that detector position was terminated. Net counting statistics for the elastic group were always better than 1% except in deep minima of the differential cross sections.

At least two and often three polyethylene spectra were taken during the course of each angular distribution measurement. A polyethylene scattering sample was mounted and a spectrum was accumulated until approximately 10,000 counts had accumulated in the neutron group scattered from hydrogen. A background spectrum was then accumulated. For these measurements the detector was placed at an angle near 30° chosen to give maximum kinematic separation of the hydrogen peak from carbon elastic and inelastic groups. Fig. 9 is a background-subtracted time-of-flight spectrum for neutron scattering from polyethylene at 30° for an incident neutron energy of 11 MeV. The hydrogen-scattered group appears midway between the carbon elastic group (at the right) and the inelastic group to the 4.44-MeV state of carbon. Above 12-MeV incident neutron energy the resolution of the TCF system was insufficient to completely separate the tails of the hydrogen group from those of the carbon groups. For these energies a small carbon scatterer containing the same number of carbon nuclei as the polyethylene

Fig. 9. Time-of-flight spectrum for 11 MeV source neutrons scattered by polyethylene to a laboratory angle of 30°. The neutron group scattered from hydrogen appears between and well separated from the groups scattered from carbon.

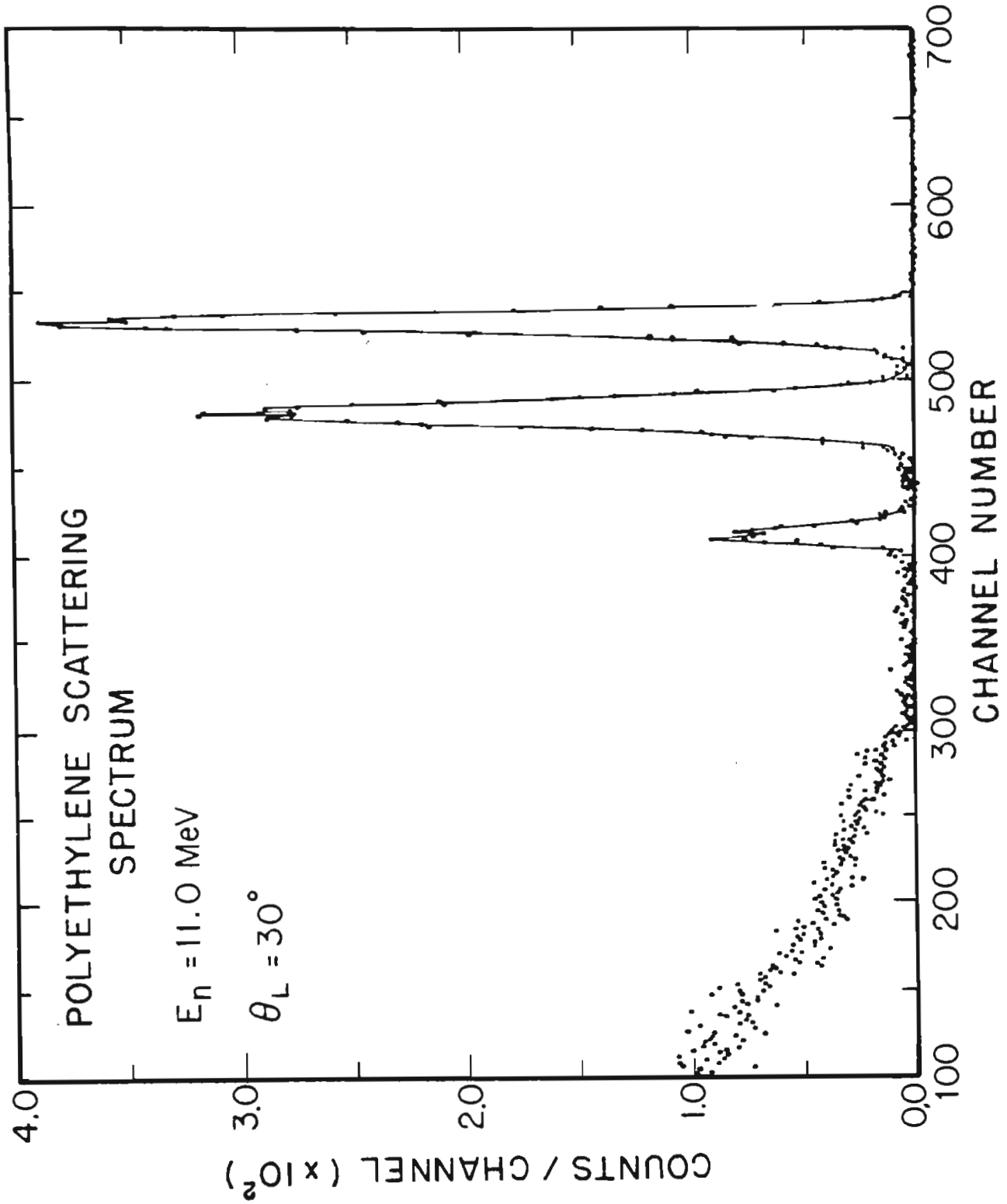
POLYETHYLENE SCATTERING
SPECTRUM
E_n = 11.0 MeV
θ_L = 30°
COUNTS / CHANNEL (x 10^2)
CHANNEL NUMBER
0.0
1.0
2.0
3.0
4.0
100
200
300
400
500
600
700

sample was used for the background run. This allowed carbon-scattered neutrons to be completely removed from the spectra.

CHAPTER III

DATA REDUCTION

Derivation of differential cross sections from measured time-of-flight spectra required three steps. In the first of these, spectra were read back from magnetic tape where they had been stored during the experiment, difference spectra were formed by subtracting background from foreground runs, and the yields for the various neutron groups of interest were obtained from the difference spectra. In the next step, sets of yields vs. angle for a particular energy and scattering process were converted to normalized angular distributions. The yield in the hydrogen-scattered group from the polyethylene spectra were used here together with the known $^{1}H(n,n)^{1}H$ differential cross section and the energy dependence of the main neutron detector efficiency. The latter had to be determined in an independent experiment. Finally, the data were corrected for finite geometry and multiple scattering effects.

Difference Yields

The time-of-flight difference spectra were obtained by subtracting a monitor-normalized background run, taken with sample removed, from the sample-"in" spectrum. The expression used was

$$D = (F - rgB)/f. \qquad (3.1)$$

D Foreground-minus-background yield in a particular time bin (channel)

F Foreground yield in the channel

B Background yield in the channel

r Ratio of $D(d,n)^3He$ yields in the monitor detector obtained during foreground and background runs

f Fractional main detector live-time for the foreground run

g Electronic dead-time correction factor equal to the product of the main detector foreground and monitor detector background live-time fractions divided by the product of the main detector background and monitor detector foreground live-time fractions

Subtraction of sample-"out" runs failed to remove all neutron background. What source-related background remained was primarily due to neutrons produced by $D(d,n)^3He$ reaction with deuterium driven into the tantalum beam stop and scattered by the sample. Normally additional runs with evacuated gas cell would have been required to remove such background from the spectra; however, gas-"out" spectra proved to be very smooth and could be approximated with a low-order polynomial.

A fitting procedure was adopted for removing the residual background from the time-of-flight spectra. In each difference spectrum, a time window was selected to frame some

neutron group of interest. Background windows on both sides of this time window were chosen and a polynominal fit was made to the portion of the spectrum inside the background windows. The area under the polynomial curve inside the time window was taken as the residual background estimate and removed from the sum over the time window.

The size of the residual background was typically below 2% for the elastic groups and from 2 to 10% for inelastic groups. The error assigned to the background subtraction was estimated from the scatter of the background values about a smooth angular dependence. The total errors on the extracted yields were formed by combining the errors on this residual background and statistical errors in quadrature.

Normalization

Fully background subtracted yields for a complete set of detector angles and for the hydrogen-scattered group in the polyethylene spectra were scaled to correspond to the same (arbitrary) number of monitor detector counts. The final set of yields vs. angle was converted to absolute cross section. The expression used was

$$\frac{d\sigma}{d\Omega}(E,\theta) = \frac{Y(\theta)}{Y_H(\theta_H)} \cdot \frac{1}{A(\theta_H)} \cdot \frac{\varepsilon_H}{\varepsilon} \cdot \frac{n_H}{n} \cdot \frac{d\sigma}{d\Omega}(E,\theta_H) \qquad (3.2)$$

$\frac{d\sigma}{d\Omega}(E,\theta)$ Differential cross section as a function of incident neutron energy E and scattering angle θ for the group of interest

$Y(\theta)$	Monitor-normalized yield for the group of interest in the difference spectrum at angle θ
$Y_H(\theta_H)$	Monitor-normalized yield for the hydrogen-scattered group in the polyethylene spectrum for angle θ_H
$A(\theta_H)$	Attenuation correction factor for the hydrogen group from the polyethylene scatterer, which also includes a first-order multiple scattering correction (see "Data Correction" below)
ε_H	Relative efficiency of the neutron detector at the energy of neutrons scattered to angle θ_H by hydrogen
ε	Relative efficiency of the detector at the energy of the neutron group of interest scattered to angle θ by the sample material
n_H	Number of hydrogen atoms in the polyethylene scatterer
n	Number of atoms in the sample
$\frac{d\sigma_H}{d\Omega}(E,\theta_H)$	Neutron differential cross section for hydrogen at energy E and angle θ_H taken from the work of Hopkins and Breit[11]

The detector relative efficiency is required for data normalization. This may be calculated, in principle, provided that scintillator composition, partial neutron cross section for the constituent elements, scintillator light output vs. energy for the various recoil particles produced by incident neutrons, and the phototube response function are known. All of these properties are not usually known with sufficient

accuracy to permit calculation of the detector efficiency with confidence. Therefore, a direct measurement of the relative efficiency for the main neutron detector was made. Appendix I describes this auxiliary experiment and its results. The efficiency curve obtained and used in the analysis is shown in fig. 10. The dots represent the efficiency data obtained in the experiment, and the line is the result of a smooth fit to the data. For comparison, the results of a Monte Carlo efficiency calculation performed for the present detector and scattering geometry is shown as the crosses in fig. 10[12]. The calculation was performed at Oak Ridge National Laboratory using program O5S[13]. The calculation fails to describe the relative efficiency data at the high and low energy ends of the range.

The ^{7}Li data presented a special problem for efficiency correcting the yields. Since the spectrometer energy resolution(see fig. 5) was not sufficient to separate the elastic scattering from scattering to the 0.478 MeV state over the energy range of the present experiment, the group corresponding to these processes in the scattering spectra was not monoenergetic. The problem was resolved by using the energy of the elastically scattered neutrons in eq. 3.2 for normalizing the data and including the proper efficiency correction in the Monte Carlo data-correction program(to be described).

It is possible also that the inelastic group for ^{9}Be contains small contributions from scattering to states in ^{9}Be

Fig. 10. Efficiency of the main neutron detector vs. neutron energy. The crosses are the result of a Monte Carlo calculation. The dots and the smooth line through them are the results of a measurement of the relative efficiency of the detector. The measured data has been normalized to the calculated values at 6 MeV.

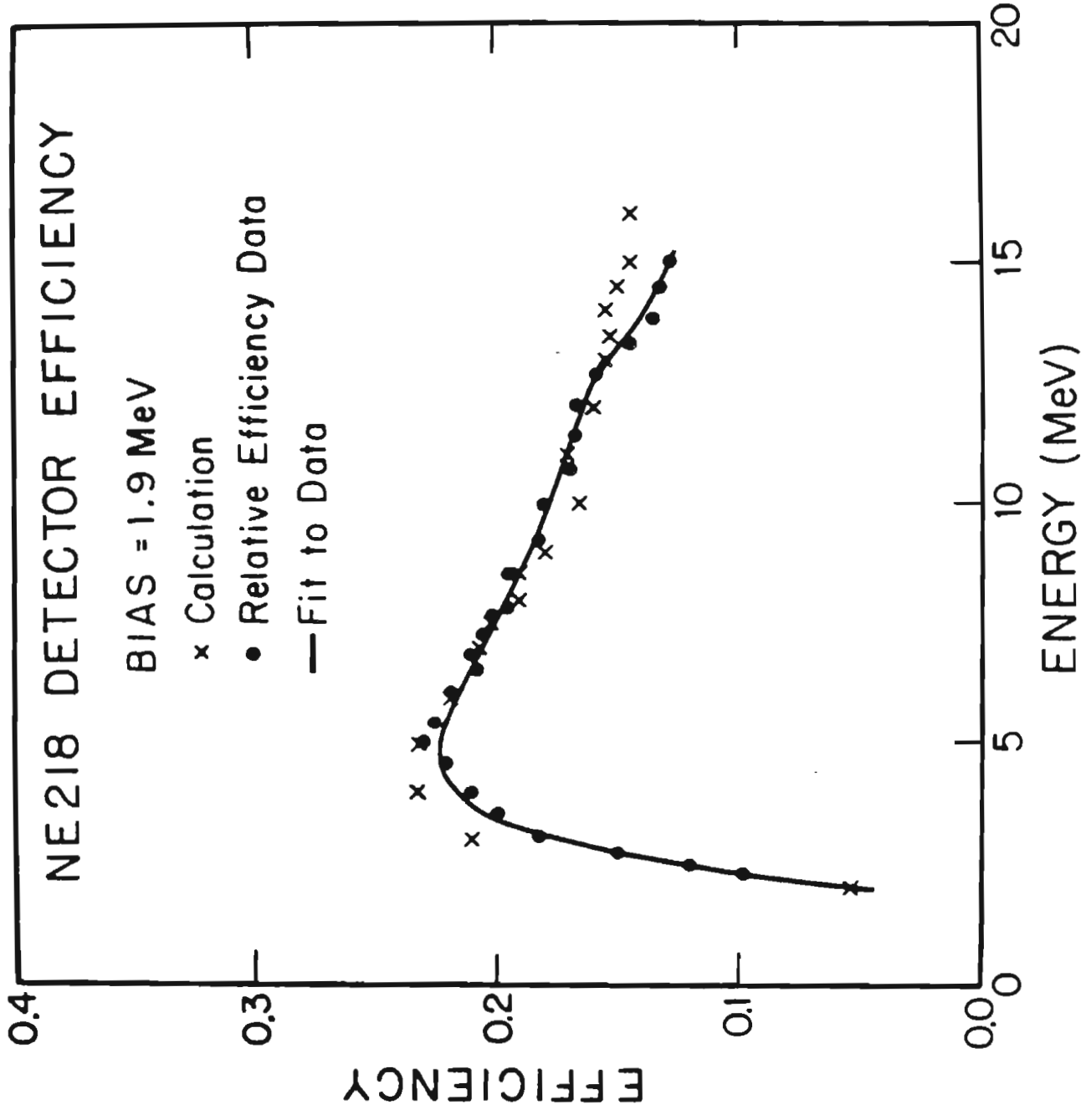
NE218 DETECTOR EFFICIENCY
BIAS = 1.9 MeV
× Calculation
• Relative Efficiency Data
— Fit to Data
EFFICIENCY
ENERGY (MeV)
0.0
0.1
0.2
0.3
0.4
0
5
10
15
20

near 1.7, 2.8, and 3.1 MeV for the higher bombarding energies. Reference to fig. 5 shows that these states would not be experimentally resolved from the 2.43-MeV state over most of the energy range covered here. At the lower bombarding energies where the states would be resolved, they appear not to contribute to the spectra. See, for example, the difference spectum for 7 MeV incident neutrons scattered to 130° (fig. 11). It was assumed in the data reduction that contributions to the ^{9}Be inelastic group other than the 2.43-MeV state, if present, are negligible. The term "2.43-MeV state" has been used throughout to refer to this group of states in ^{9}Be.

An additional factor is generally required in eq. 3.2 whenever the neutron source is non-isotropic and the sample and normalization scatterer are of different dimensions. This is a correction for the different average incident neutron fluence seen by the two scatterers. In the present case, however, dimensions of the sample and normalization scatterer were chosen to obey the criterion of Velkley et al.[14], i.e.,

$$H_p^2 \left(H_p^2 + D_p^2 \right) = H^2 \left(H^2 + D^2 \right), \qquad (3.3)$$

where H_p and D_p are the height and diameter of the polyethylene scatterer, and H and D are corresponding quantities for the sample. For the D(d,n)^{3}He reaction and for samples with dimensions chosen according to this criterion, Monte Carlo

Fig. 11. Background-subtracted time-of-flight spectrum for 7 MeV neutrons scattered to laboratory angle 130° by ^{9}Be. Groups corresponding to scattering to states in ^{9}Be near 1.7, 2.8, and 3.1 MeV do not appear.

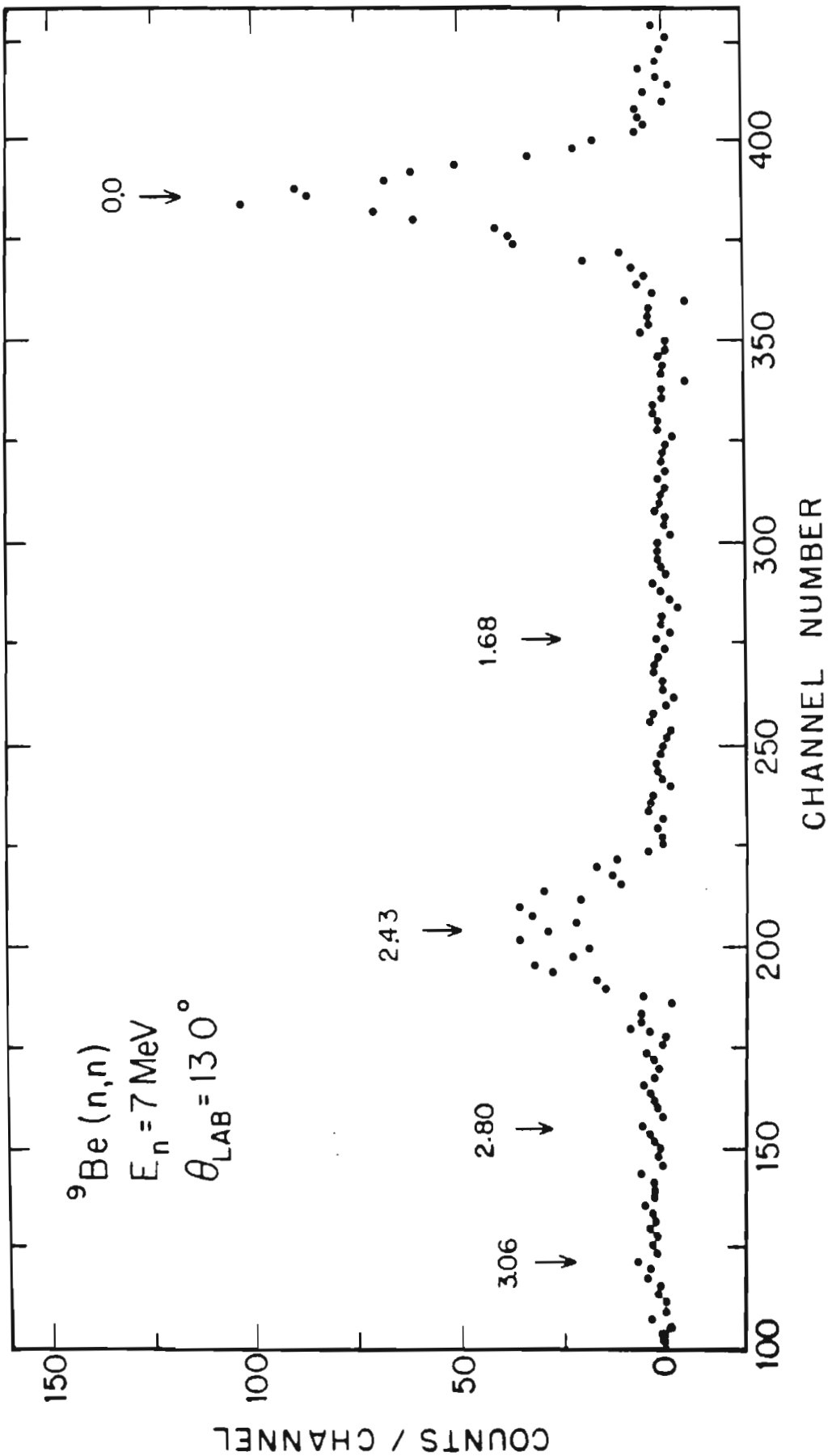
^{9}Be (n,n)
E_n = 7 MeV
θ_{LAB} = 130°
0.0
1.68
2.43
2.80
3.06
COUNTS / CHANNEL
CHANNEL NUMBER
0
50
100
150
100
150
200
250
300
350
400

calculations have shcwn that the fluence correction factor is unity to within 1%.

Data Correction

The factor A used in eq. 3.2 to correct the hydrogen-scattered yield for attenuation and multiple scattering in the polyethylene sample was

$$A(\theta_H) = \exp\{(\pi/4)\sum(E_o)R + (8/3\pi)\sum(E_1)B\}, \qquad (3.4)$$

where, $\sum = n_H\sigma_H + n_c\sigma_c$

n_H Hydrcgen nuclear density in the polyethylene sample

n_c Carbcn nuclear density in the polyethylene sample

σ_H Hydrcgen total crcss section

σ_c Carbcn non-elastic cross section

E_o Incident neutron energy

E_1 Energy cf neutrons scattered to angle θ_H by hydrcgen

R Radius of polyethylene scatterer

This expression is the "disc approximation" of Kinney[15] with the exception that the carbon nonelastic cross section is used here rather that the total cross section. This modification was suggested by the authors cf ref. 14. The aim of the

modification was to provide a first-order correction for multiple scattering in the polyethylene sample by incorporating the following reasonable assumptions:

1. Most neutrons elastically first-scattered by carbon in the polyethylene sample are not lost from the neutron flux incident at a hydrogen site
2. Equal numbers of neutrons are elastically second-scattered into and out of the detector solid angle by carbon
3. The average energy lost to carbon in neutron elastic scattering is so small that neutrons scattered once by carbon and once by hydrogen remain within the time-of-flight window for the singly-scattered hydrogen group

The magnitude of the total correction required for the small polyethylene sample employed in the present work was 5-6%. The multiple scattering part of the correction was less than 1%; therefore, the analytic correction method employed was considered quite adequate.

Eq. 3.2 produced differential cross sections vs. angle for particular neutron groups appearing in the difference spectra. These required correction by up to 20% due to the combined effects of the experimental averaging over the finite neutron source, sample and detector volumes; attenuation of the incident neutron flux in the sample; and multiple scattering in the sample. Several authors have given analytic prescriptions for making corrections for these effects subject to certain

restrictions and approximations[14-18]. These methods have usually been shown to be accurate to a few percent for heavy elements and for energies away from resonance structure in the scattering cross sections. For other cases the quality of the corrections can not be predicted.

In order that data corrections provide no limitation on the accuracy of the final cross sections, the present data were corrected using an exact numerical technique. Briefly, an iterative method was employed to solve for point-geometry differential cross section values at each experimental energy and angle using Monte Carlo simulation of the scattering spectra. Full detail of the problem, the solution technique, and the operating characteristics of a computer program for carrying out this calculation are given in appendix II.

One additional data correction was necessary for the ^{6}Li elastic scattering data. This was removal of the effects of a 5.0% ^{7}Li contaminant. The following expression was used.

$$\frac{d\sigma_6}{d\Omega} = \left[\frac{d\sigma_{6+7}}{d\Omega} - k \frac{d\sigma_7}{d\Omega} \right] \frac{1}{k-1} \qquad (3.5)$$

$\frac{d\sigma_{6+7}}{d\Omega}$ Effective differential elastic cross section value at some angle and energy for the ^{6}Li scatterer with its ^{7}Li contamination

$\frac{d\sigma_6}{d\Omega}$ Desired ^{6}Li cross section for that angle and energy

$\frac{d\sigma_7}{d\Omega}$ Measured ^{7}Li cross section for that angle and energy

k Fractional number of ^{7}Li nuclei in the ^{6}Li scatterer

Sources of uncertainty in the present experiments and typical magnitudes in percent for the contribution of each are given in table 3. These are divided into relative and normalization errors. Relative errors are errors on quantities which have an angular dependence; normalization errors, those on quantities which merely scale the angular distributions. Partial relative and normalization errors were separately combined in quadrature to obtain total relative and normalization errors. The normalization error was quoted for each angular distribution, and the total error--quadratic combination of total relative and normalization errors--was quoted at each angle. The relative errors were used in weighting the Legendre polynomial fits to be described.

Data Presentation

The present ^{6}Li, ^{7}Li, ^{9}Be, and ^{12}C data, converted to the center-of-mass system, are presented in figs. 12-17. The ^{7}Li elastic + 0.478-MeV angular distributions were converted to the center-of-mass system as though only elastic scattering were present. The error introduced by this approximation was negligible. The lines through the points on figs. 12-17 are the results of fitting each of the distributions with a sum of Legendre polynomials,

TABLE 3

SOURCES OF UNCERTAINTY IN THE MEASUREMENTS

Source	^{6}Li and ^{7}Li measurements	^{9}Be measurements	^{12}C measurements
	Relative Errors		
Counting Statistics	1-10% elas. 4-25% inel.	0.5-4% elas. 2.5-6% inel.	1-10% elas. 2- 5% inel.
Detector Efficiency	0-2.5%	0-2.5%	0-2.5%
Monte Carlo Corrections	0-1%	0-1%	0-1%
	Normalization Errors		
n-p Scattering Yield	1-6%	2-4%	1-5%
Analytic Correction to n-p Yield	2%	2%	2%
n-p Differential Cross Section	1-1.2%	1-1.2%	1-1.2%

Fig. 12. Center-of-mass elastic and inelastic differential cross section data for ^{6}Li. The curves result from Legendre polynomial fits to the data. Both second and fourth order fits to the inelastic distribution at 11 MeV are shown. The fourth order fit was chosen.

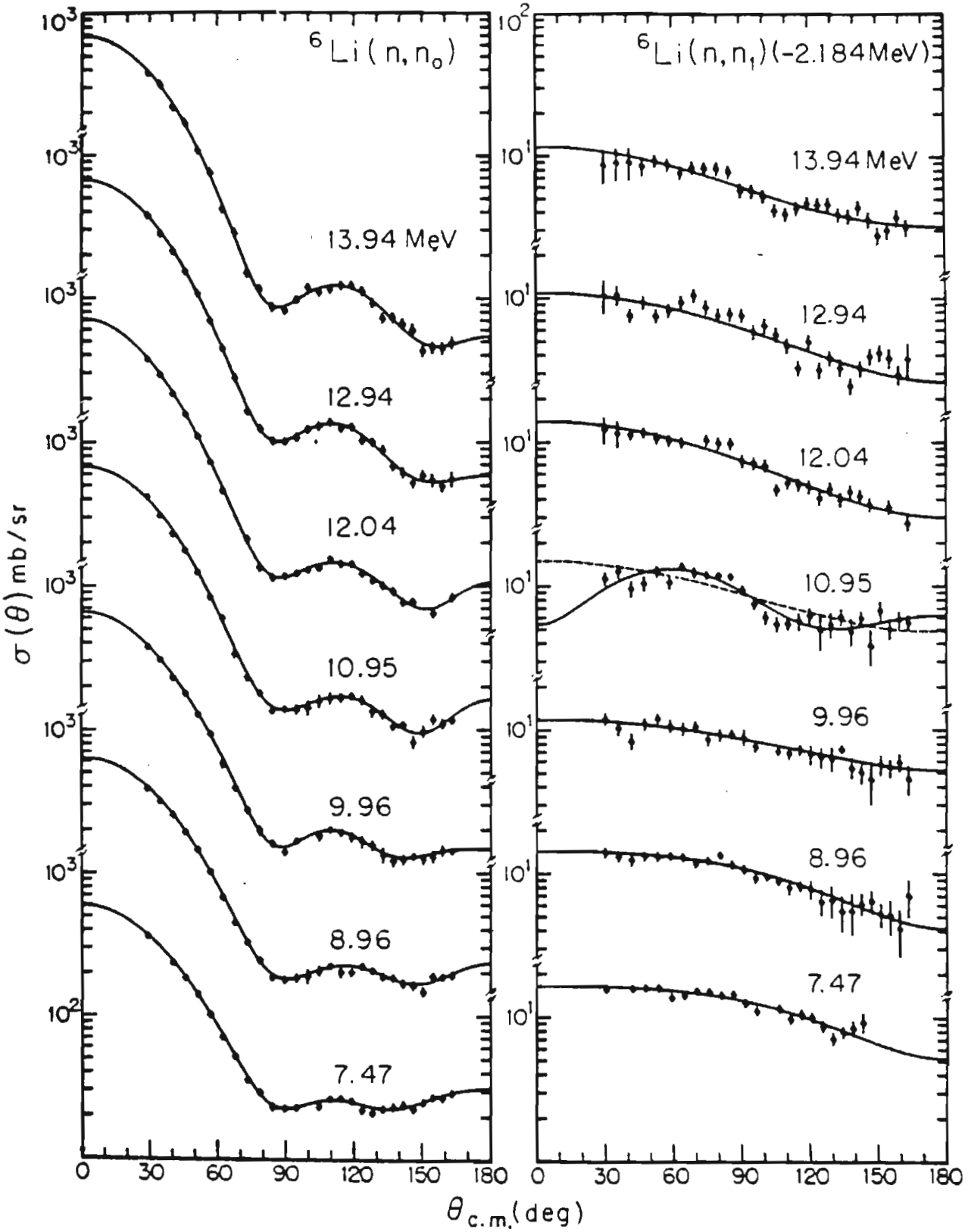
$^6Li(n,n_o)$
$^6Li(n,n_1)(-2.184MeV)$
13.94 MeV
12.94
12.04
10.95
9.96
8.96
7.47
$\sigma(\theta)$ mb/sr
$\theta_{c.m.}$(deg)
0
30
60
90
120
150
180

Fig. 13. Center-of-mass differential cross section data for neutron elastic scattering by ^{7}Li plus scattering to the 0.478-MeV state and cross section data for inelastic scattering to the 4.63-MeV state in ^{7}Li. The curves result from Legendre polynomial fits to the data.

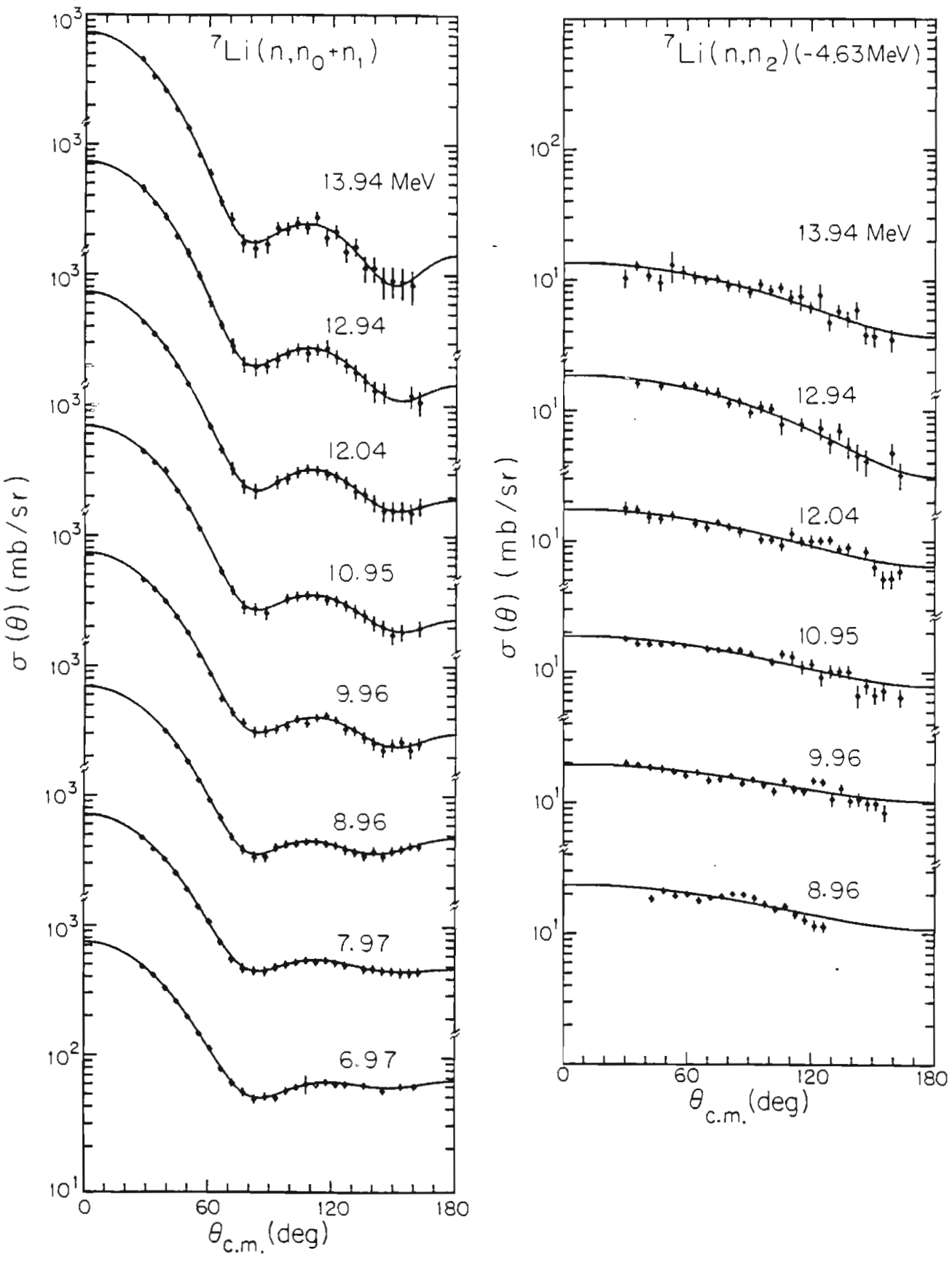
^{7}Li(n,n$_0$+n$_1$)
13.94 MeV
12.94
12.04
10.95
9.96
8.96
7.97
6.97
σ(θ) (mb/sr)
θ$_{c.m.}$ (deg)
^{7}Li(n,n$_2$)(-4.63MeV)
13.94 MeV
12.94
12.04
10.95
9.96
8.96
σ(θ) (mb/sr)
θ$_{c.m.}$ (deg)

Fig. 14. Center-of-mass differential cross section data for neutron elastic scattering by ^{9}Be. The curves through the data result from Legendre polynomial fits. The small angle data of ref. 19 are shown at 9, 11, and 14 MeV.

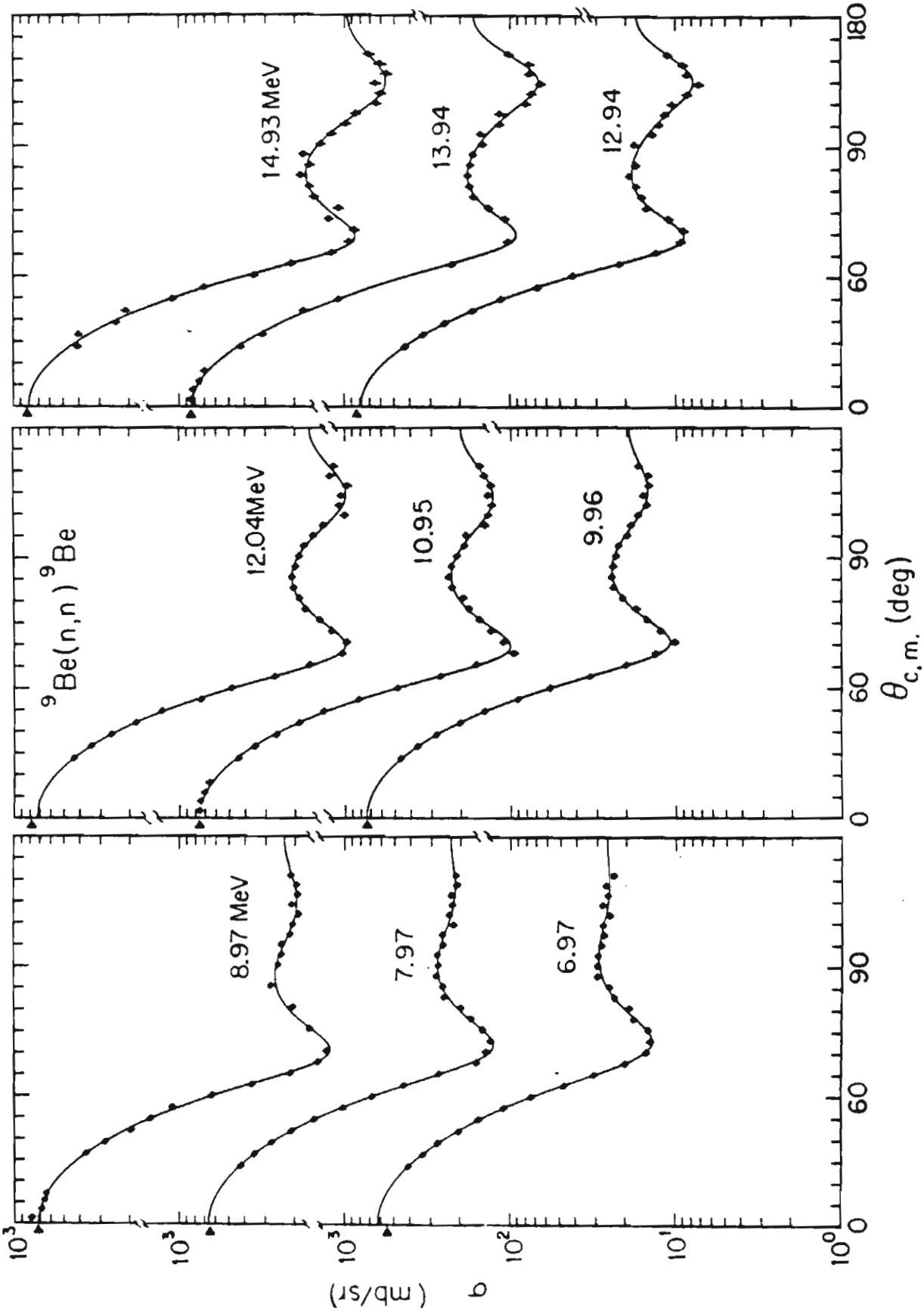
^{9}Be(n,n)^{9}Be
14.93 MeV
13.94
12.94
12.04MeV
10.95
9.96
8.97 MeV
7.97
6.97
σ (mb/sr)
$\theta_{c.m.}$ (deg)

Fig. 15. Center-of-mass differential cross section data for neutron inelastic scattering to the 2.43-MeV state in ^{9}Be. The curves through the data result from Legendre polynomial fits.

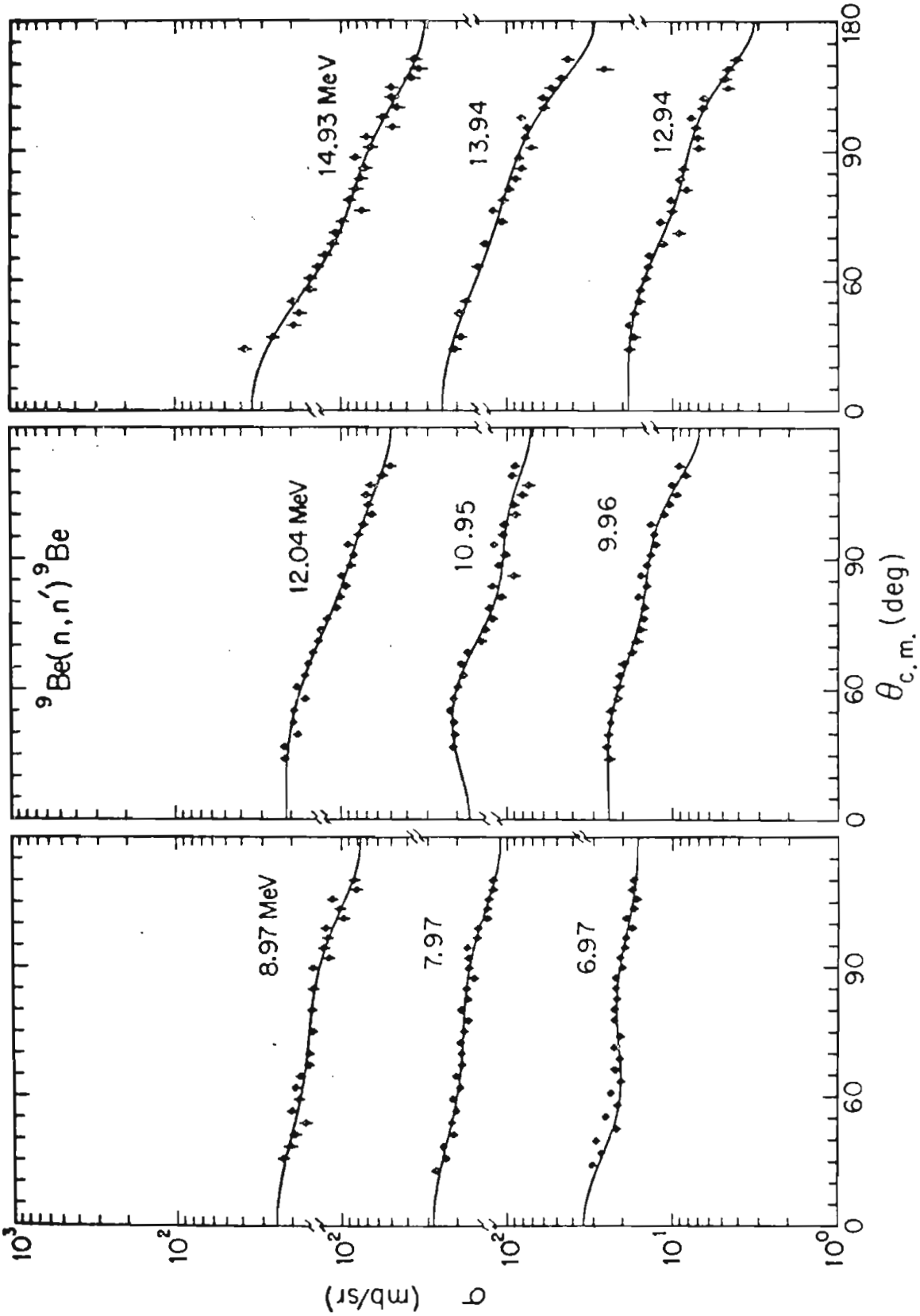
^{9}Be(n,n')^{9}Be
14.93 MeV
13.94
12.94
12.04 MeV
10.95
9.96
8.97 MeV
7.97
6.97
σ (mb/sr)
$\theta_{c.m.}$ (deg)

Fig. 16. Center-of-mass differential cross section data for neutron elastic scattering by carbon. The curves through the data result from Legendre polynomial fits.

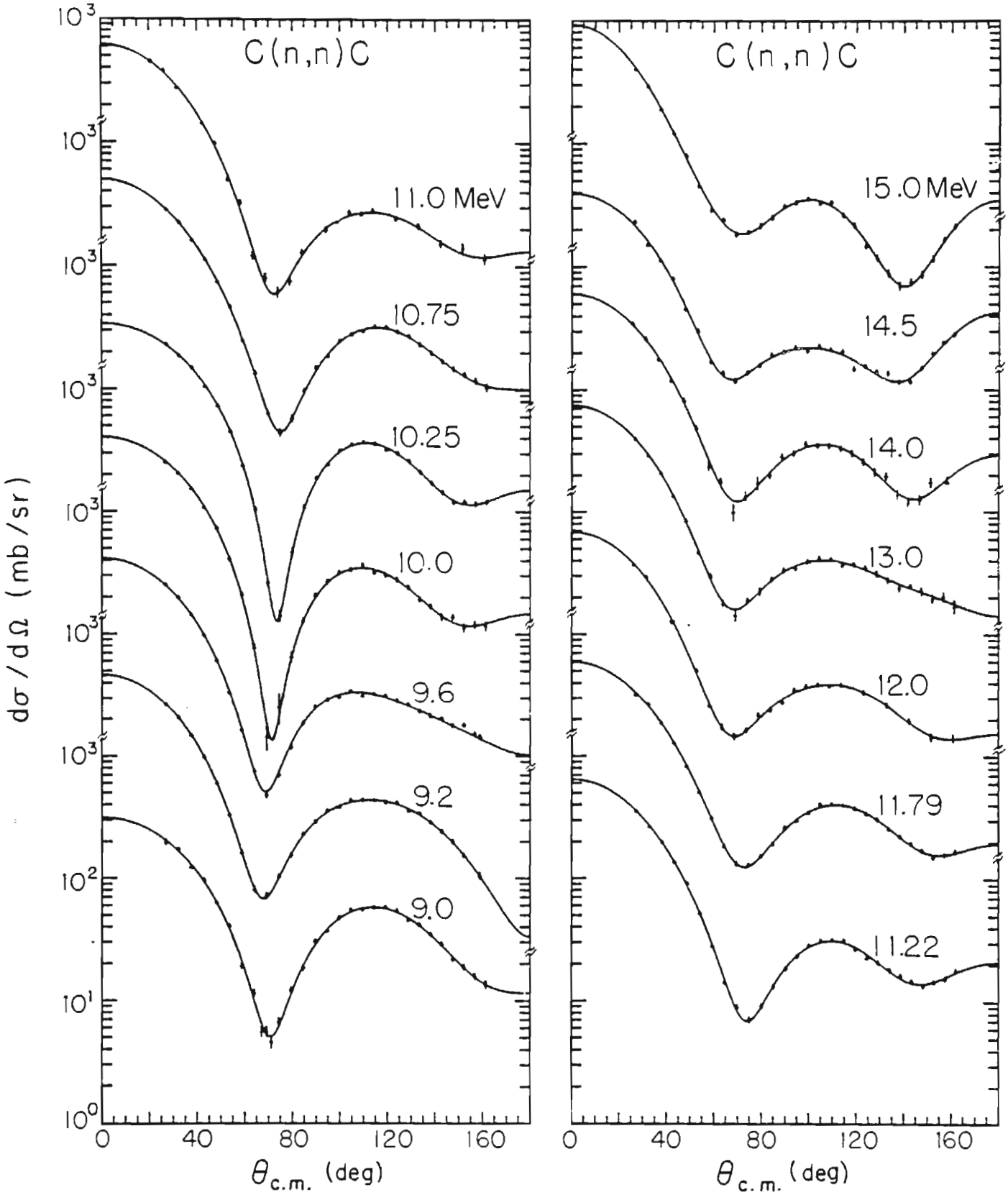
C(n,n)C
11.0 MeV
10.75
10.25
10.0
9.6
9.2
9.0
C(n,n)C
15.0 MeV
14.5
14.0
13.0
12.0
11.79
11.22
dσ/dΩ (mb/sr)
θc.m. (deg)
θc.m. (deg)

Fig. 17. Center-of-mass differential cross section data for neutron inelastic scattering to the 4.44-MeV state of ^{12}C. The curves through the data result from Legendre polynomial fits.

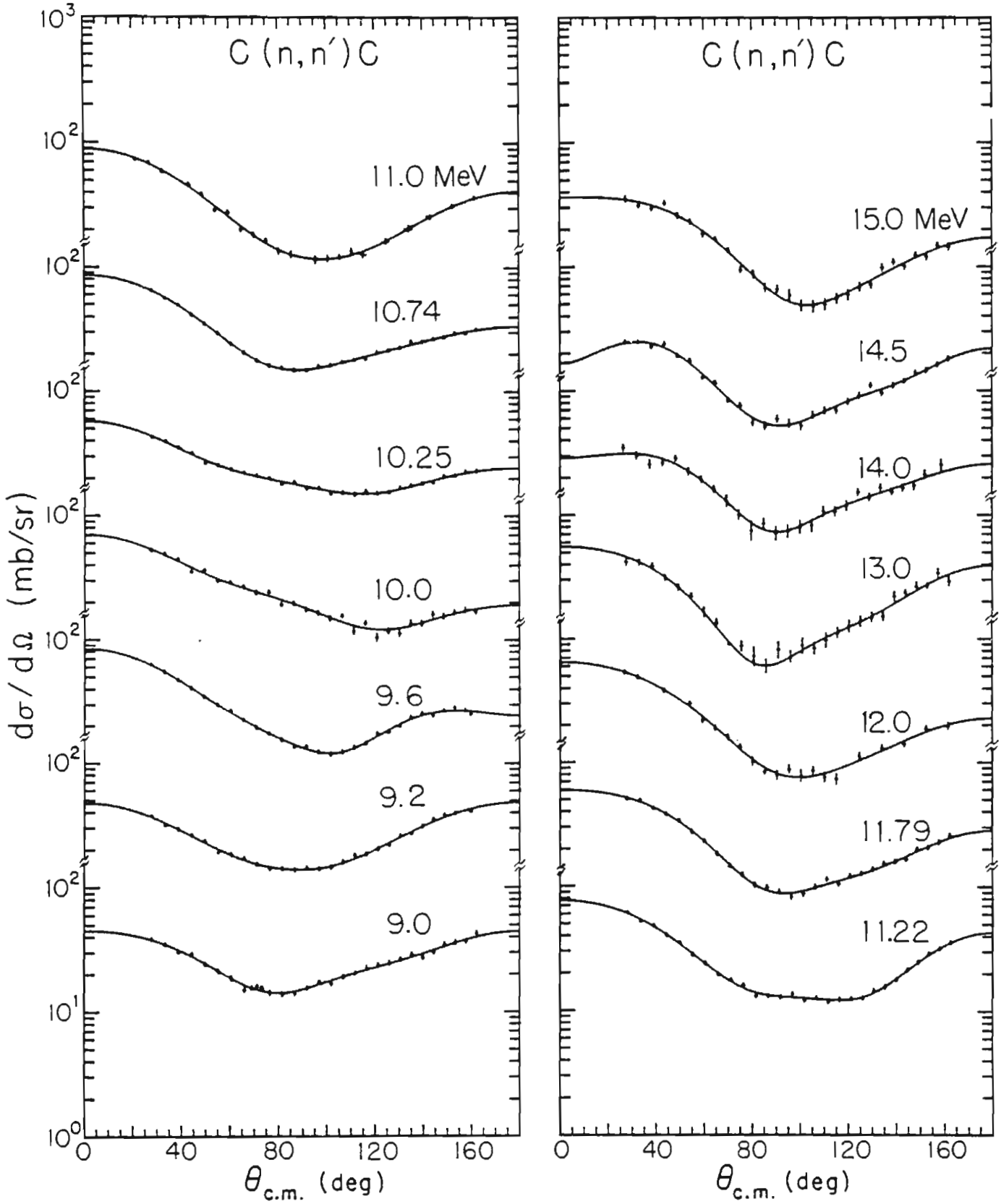
C (n, n′) C
11.0 MeV
10.74
10.25
10.0
9.6
9.2
9.0
C (n, n′) C
15.0 MeV
14.5
14.0
13.0
12.0
11.79
11.22
dσ/dΩ (mb/sr)
θc.m. (deg)
θc.m. (deg)

$$\frac{d\sigma_F}{d\Omega}(\theta) = \sum_{l=0}^{l_{max}} a_l P_l(\cos\theta) \qquad (3.6)$$

The values of the a_l coefficients from the fits are given in appendix III. The small angle data of Bucher and Hollandsworth[19] for elastic scattering by ^{9}Be to angles smaller than 20° is also shown for energies of 9, 11, and 14 MeV. This serves as a check on the extrapolation of the differential cross section to small angles by means of Legrendre polynomial fitting.

The coefficients in eq. 3.6 for a given l_{max} were chosen in the usual manner, i.e., by requiring a minimum in the chi-square,

$$\chi^2 = \sum_{i=1}^{N} \{[\frac{d\sigma_F}{d\Omega}(\theta_i) - \frac{d\sigma_E}{d\Omega}(\theta_i)]/\Delta(\theta_i)\}^2, \qquad (3.7)$$

where $\frac{d\sigma_F}{d\Omega}(\theta_i)$, $\frac{d\sigma_E}{d\Omega}(\theta_i)$, and $\Delta(\theta_i)$ are, respectively, the fitted cross section value, experimental cross section value, and the experimental relative error at angle θ_i. N is the number of angles at which data were taken.

The maximum coefficient order l_{max} was chosen to be that value giving best agreement with the following criteria:

1. The chi-square per degree of freedom $\chi^2/(N-l_{max}-1)$ vs. l_{max} is minimum
2. $\frac{d\sigma_F}{d\Omega}(0°)[= \sum_{l=0}^{l_{max}} a_l] > \sigma_\omega$
3. Coefficients a_l for $l \leq l_{max}$ are significant

The quantity σ_w of item 2 is the Wick limit[20], the theoretical lower limit of the differential elastic cross section at 0°.

$$\sigma_w = [k\sigma_T/(4\pi)]^2, \qquad (3.8)$$

where k is the center-of-mass wave number and σ_T, the total cross section at the incident neutron energy. Values of σ_T from the evaluated data file at Brookhaven National Laboratory, version ENDFB/IV, were used for carbon and beryllium. More recent σ_T values (to be included in ENDFB/V) were used for the lithium data[21].

For the best fits, integrated elastic and inelastic cross sections were obtained from

$$\sigma = 4\pi a_0 \qquad (3.9)$$

The results are plotted vs. energy in figs. 18-21 for ^{6}Li, ^{7}Li, ^{9}Be, and ^{12}C, respectively. The total, elastic, and available partial inelastic or total non elastic cross section values from ENDFB/IV are also shown in the figures over the energy range of the present data. These represent the state of knowledge of cross sections for those elements prior to the present work. A recent measurement of the elastic and inelastic differential cross section for neutron scattering by ^{12}C over the same range as the present measurements has been made

Fig. 18. Neutron cross sections for ^{6}Li vs. energy. The points are from the present measurements and the curves are from ENDFB/IV. The lower curve is the total $^{6}Li(n,n'\alpha)d$ cross section, of which the cross section for excitation of the 2.18-MeV state in ^{6}Li is a part.

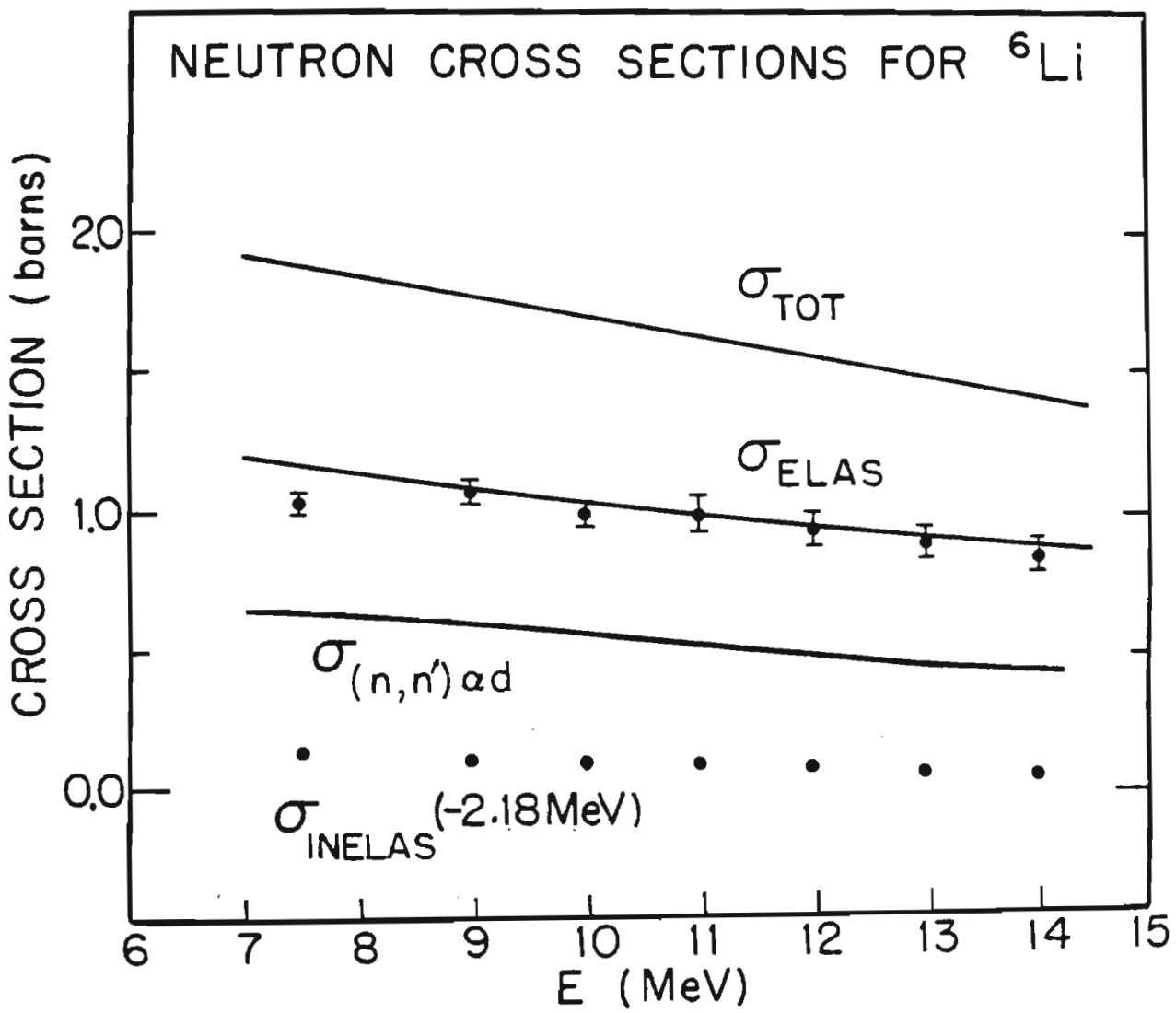
NEUTRON CROSS SECTIONS FOR ^{6}Li
CROSS SECTION (barns)
2.0
1.0
0.0
σ_{TOT}
σ_{ELAS}
$\sigma_{(n,n')\alpha d}$
σ_{INELAS} (-2.18 MeV)
6
7
8
9
10
11
12
13
14
15
E (MeV)

Fig. 19. Neutron cross sections for ^{7}Li vs. energy. The solid dots are the present data. The elastic cross section was obtained by subtracting the cross section for inelastic scattering to the 0.478-MeV state of ref. 24 (open circles at bottom) from the present elastic plus 0.478-MeV state cross section. The total cross section data shown are from ref. 20. The lines shown are eye guides.

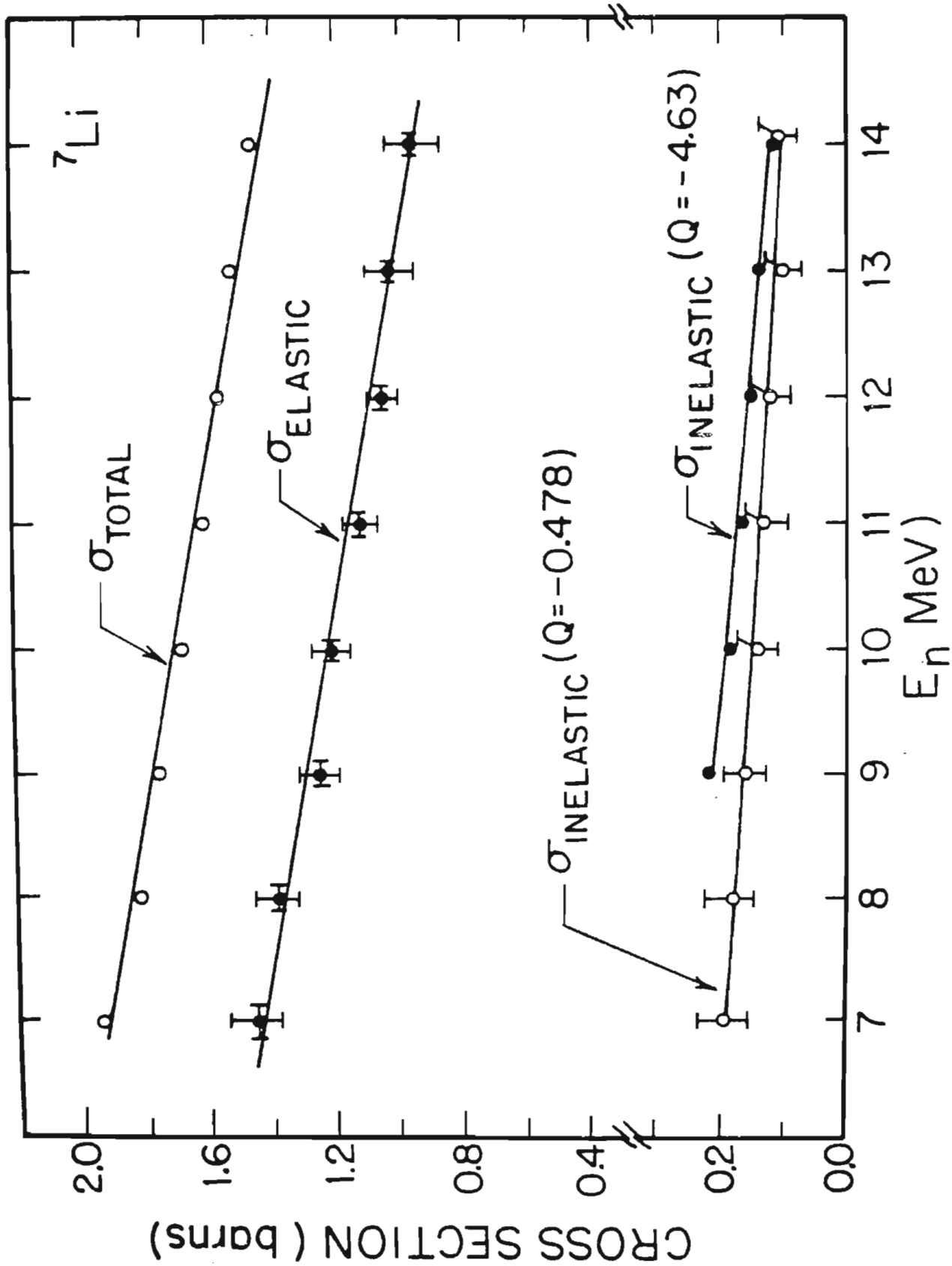
^{7}Li
σ_{TOTAL}
$\sigma_{ELASTIC}$
$\sigma_{INELASTIC}$ (Q=-0.478)
$\sigma_{INELASTIC}$ (Q=-4.63)
CROSS SECTION (barns)
E_n MeV)
0.0
0.2
0.4
0.8
1.2
1.6
2.0
7
8
9
10
11
12
13
14

Fig. 20. Neutron cross sections for ^{9}Be vs. energy. The points are from the present measurements of the ^{9}Be elastic and 2.43-MeV state cross section. The solid curves are corresponding values from ENDFB/IV. The dashed curve represents the total (n,2n) cross section, of which the cross section for excitation of the 2.43-MeV state is a part.

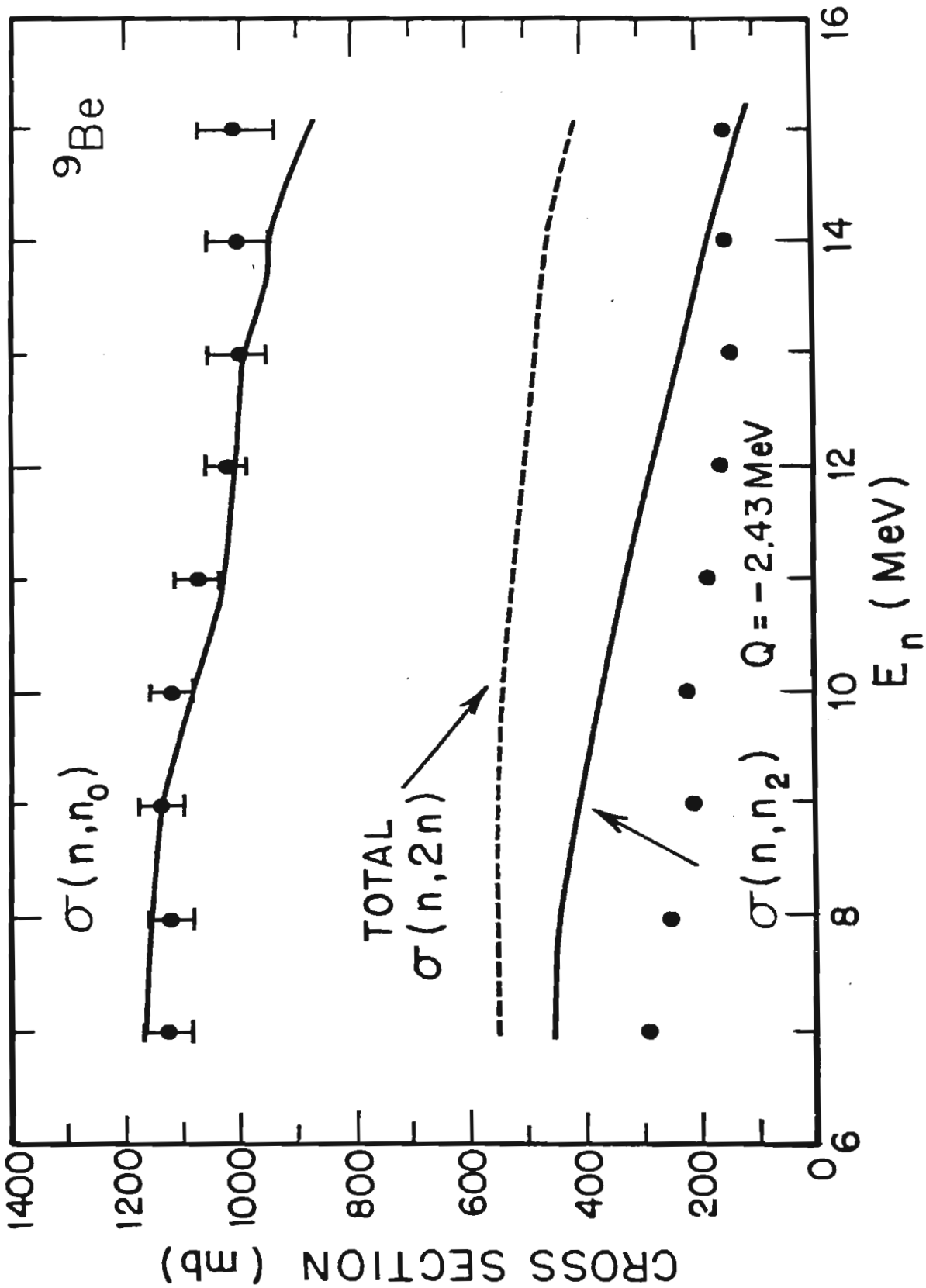
^{9}Be
$\sigma(n,n_0)$
TOTAL
$\sigma(n,2n)$
$\sigma(n,n_2)$
Q = −2.43 MeV
E_n (MeV)
CROSS SECTION (mb)
0
200
400
600
800
1000
1200
1400
6
8
10
12
14
16

Fig. 21. Neutron cross sections for ^{12}C vs. energy. The solid circles are the present data, the crosses are the data of ref. 22, and the curves are from ENDFB/IV.

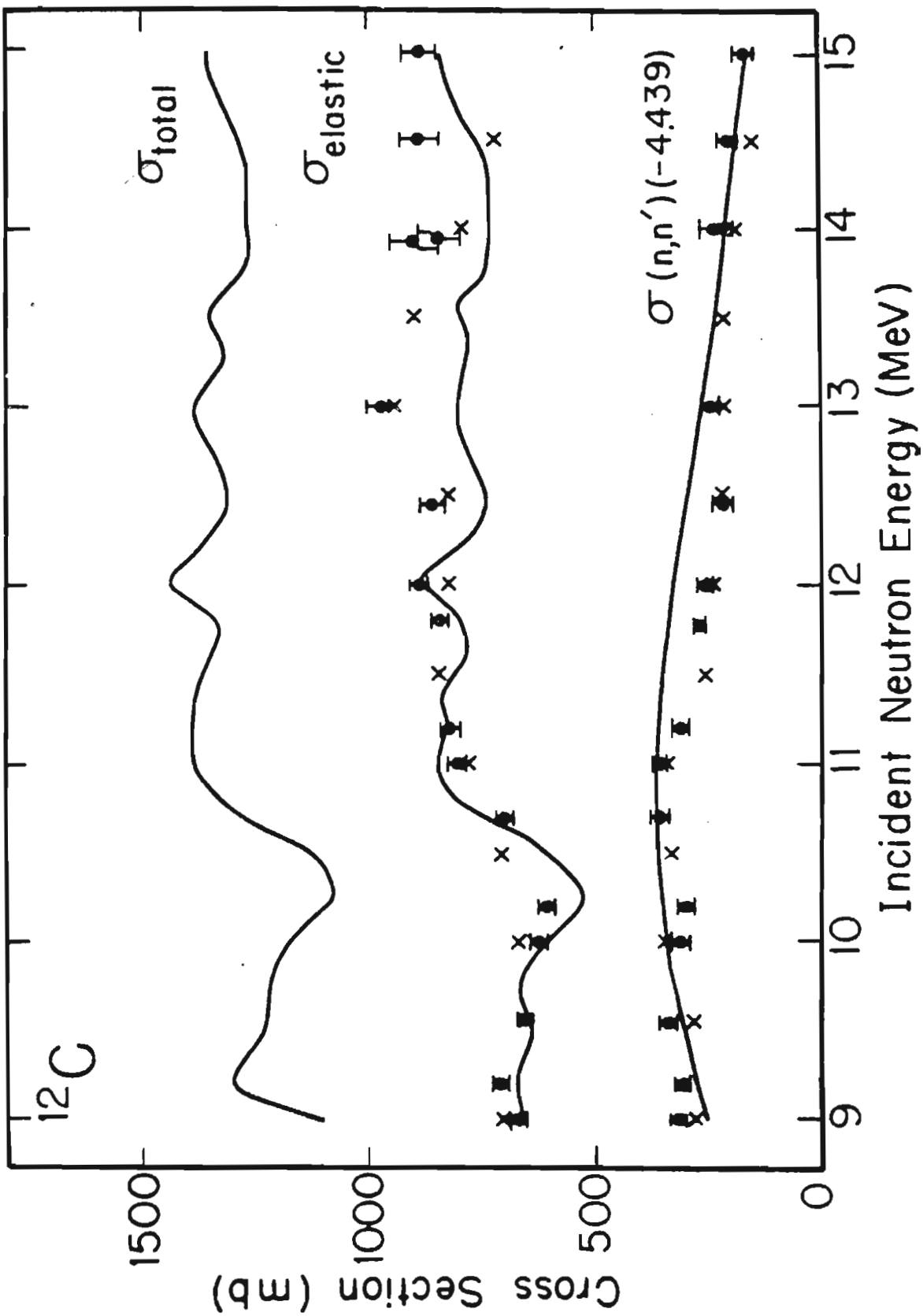
^{12}C
σ_{total}
$\sigma_{elastic}$
$\sigma(n,n')(-4.439)$
Cross Section (mb)
0
500
1000
1500
9
10
11
12
13
14
15
Incident Neutron Energy (MeV)

by Hacuat et al[22]. The integrated cross sections from that work are included in fig. 21. Data from the present work is now included in the data files of the National Nuclear Cross Section Center at Brookhaven National Laboratory.

CHAPTER IV

OPTICAL MODEL ANALYSES

The present neutron scattering data was analysed to yield information related to the isospin dependence of the effective neutron-nucleus potential for very light nuclei. The phenonenological optical model(OM) was used to analyse the elastic scattering data. In this model the isospin dependence takes the form of a term proportional to (N-Z)/A (symmetry term) in the real and imaginary well depths. An extension of the OM, a coupled channels(CC) treatment, was used to analyse both elastic scattering and inelastic scattering to low-lying target states for some of the present data.

The use of the OM to describe scattering from very light mass requires some justification. As explained in section I, the analysis of Watson et al.[5] for the p shell provides this justification in part. However, the Watson analysis included neutron scattering results at 14 MeV only. Thus as a first step, OM calculations were performed for the present ^{6}Li, ^{7}Li, and ^{9}Be data to verify that the OM is a useful tool to describe neutron scattering from these nuclei.

Symmetry terms were extracted directly from the comparison of the OM parameters for neutron scattering by ^{6}Li and ^{7}Li. These were also extracted in another way. The OM parameters from a previous proton scattering analysis for ^{9}Be

were adjusted to fit the present neutron plus ^{9}Be data, and the symmetry terms were obtained by comparing the proton and neutron well depths.

Coupled channels analyses were performed for ^{9}Be, coupling elastic scattering and scattering to the 2.43 MeV state, and for ^{12}C, coupling elastic scattering and scattering to the 4.44 MeV state. The CC model used included a permanent quadrupole deformation in the OM potential. The possibility of a difference in the quadrupole deformation parameter for neutron and proton projectiles was investigated for ^{9}Be. This was made possible by the existence of a previous proton scattering study on ^{9}Be using the same model. Although the ^{12}C scattering cross sections show resonance effects, a previous CC analysis was able to fit scattering data at 14.1 MeV. The present ^{12}C CC analyses extends the results of that study down to 9 MeV with good success.

Spherical Optical Model Analyses

The OM potential used in the present analyses was

$$U(r) = -Vf(x_R) - 4iW\frac{d}{dx_I}f(x_I) + \lambda_\pi^2 V_s (\vec{\sigma}\cdot\vec{l})\frac{d}{dr}f(x_s), \qquad (4.1)$$

where $f(x_i) = [1 + \exp(x_i)]^{-1}$,

$x_i = (r - r_i A^{1/3})/a_i$, and

λ_π =pion Compton wavelength = $\sqrt{2.000}$ fermi.

Only the surface imaginary well was used, and no Coulomb potential was needed for neutron projectiles. Nine parameters specify the potential. These are the real, imaginary, and spin-orbit well depths V, W, and V_S; the corresponding radius parameters r_R, r_I, and r_S; and the diffuseness parameters a_R, a_I, and a_S.

To facilitate searching the parameter space for an energy-dependent set of parameters judged to produce acceptable fits to the angular distribution data, certain parameter restrictions are justified. It is well known that CM fits are little changed with changes in V and r_R provided a relation of form Vr_R^n=constant is observed. The exponent n is usually taken to be 2. A similar "ambiguity" is expressed by Wa=constant. Because such parameter relations exist, geometric parameters were held fixed when possible in the present analyses, and all energy dependence was put into the well depths. As another restriction, the spin-orbit parameters were kept fixed (after initial optimization) near values from previous analyses. This was possible since the spin-orbit potential has the least effect on the differential cross sections of any of the terms in eq. 4.1, and that small effect may be compensated for, in large part, by changes in the other parameters.

Computer programs OPTICS[23] and SNOOPY[24] were used to perform the OM calculations. The former operates a CRT

display to permit the user to select parameter values for "visual" best fit. This is an extremely useful option for narrowing the region of parameter space to be searched by an automatic chi-square search program.

SNCOPY is such an automatic search program. It varies a given subset of parameters for a minimum value of the chi-square per datum,

$$\chi^2_N = N^{-1} \sum_{i=1}^{N} \{ [\frac{d\sigma_c}{d\Omega}(\theta_i) - \frac{d\sigma_E}{d\Omega}(\theta_i)] / \Delta(\theta_i) \}^2 \qquad (4.2)$$

The quantities $\frac{d\sigma_c}{d\Omega}$ and $\frac{d\sigma_E}{d\Omega}$ are values of the respective calculated and experimental differential cross sections at the experimental angle. Δ is the relative error on $\frac{d\sigma_E}{d\Omega}$, and N is the number of angles.

Typical analysis procedure was as follows. First, one of the angular distributions of a data set was chosen for fitting. Starting parameters were obtained from previous work. (The compilation of Perey and Perey[4] was a useful reference to previous OM analyses.) Searches were carried out on OPTICS and SNCOPY for the best nine-parameter fit. Next, starting from the parameter values of that analysis, best fits to the remaining angular distributions were obtained by varying V and W. For ^{6}Li good fits were not obtained for all energies without additional degrees of freedom; therefore, the real and imaginary diffuseness parameters also were allowed to vary in the fitting.

Figs. 22 and 23 show typical CM fits obtained for ^{6}Li and ^{9}Be, respectively. Parameter values and linear fits to their energy dependences are given in table 4. The plots of the energy dependences of those parameters which were permitted to vary with energy are shown in figs. 24 and 25 for ^{6}Li and ^{9}Be, respectively. Also plotted in fig. 25 for ^{9}Be are the energy dependences of the real and imaginary well depths from the p-shell analysis by Watson et al.[5] and parameter energy dependences from the ^{9}Be coupled-channels analysis to be described. The real well depth in the ^{6}Li analysis increases with energy over the energy region covered, while in the global analyses the opposite behavior occurs. It is not clear whether this effect is due to allowing energy dependent geometric parameters in the analysis, whether it is a compound nuclear effect, or whether it is the effect of nonlocality for very light nuclei. It was assumed that this anomalous slope for the energy dependence of the real well depth would not affect the extraction of CM symmetry terms using the procedure described below.

Since elastic scattering from ^{7}Li was not experimentally resolved from scattering to the 0.478-MeV first excited state, a different procedure was used to choose OM parameters to best describe the ^{7}Li scattering data. It was assumed that the CM parameters required for the calculation of neutron scattering from ^{7}Li differ from those required for ^{6}Li only by energy-independent terms in the real and imaginary well depths.

Fig. 22. Optical model fits tc the ^{6}Li elastic differential cross section data at 9, 11, and 13 MeV. The points are the present ^{6}Li elastic data and the curves are optical model calculations performed as described in the text.

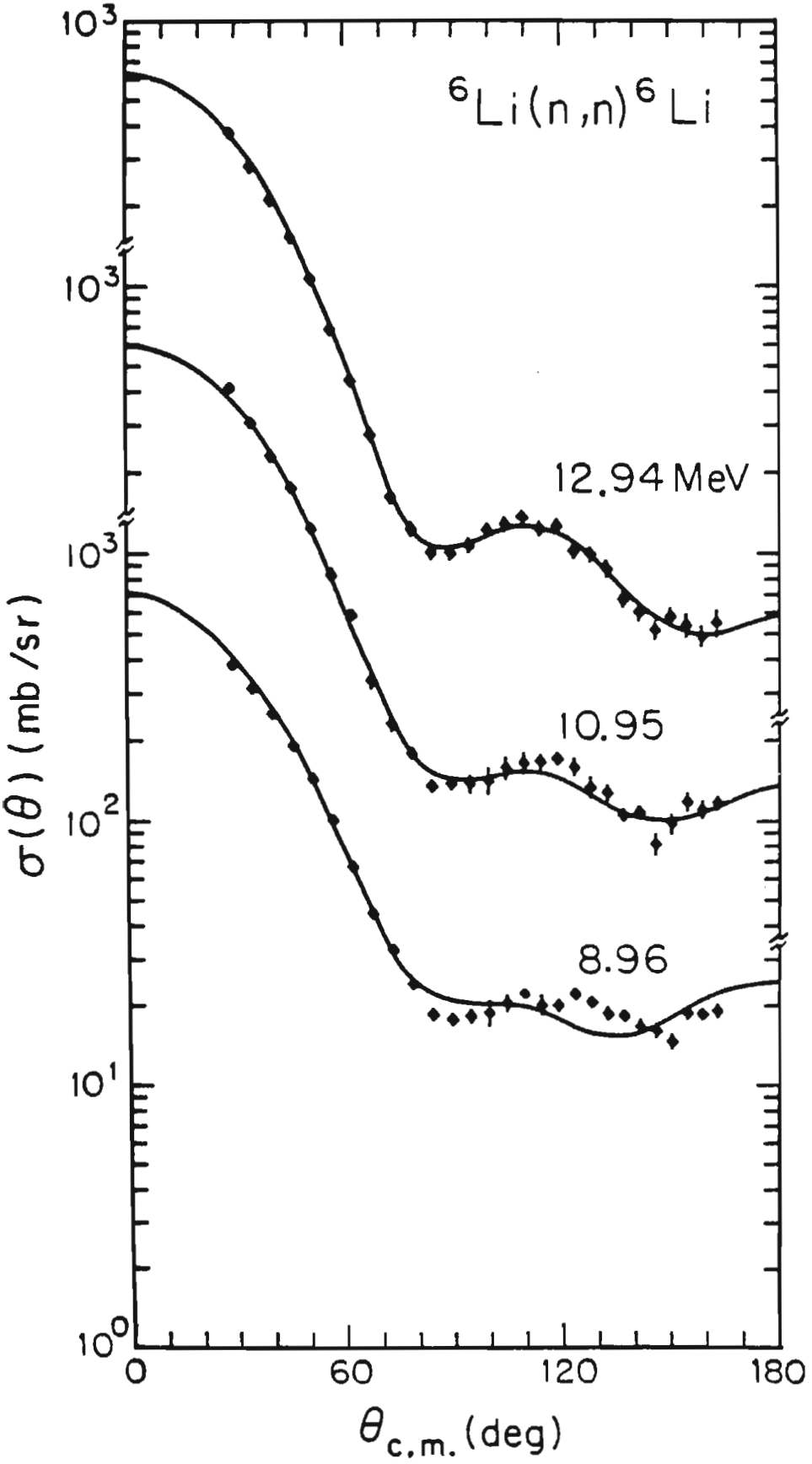
^{6}Li(n,n)^{6}Li
12.94 MeV
10.95
8.96
$\sigma(\theta)$ (mb/sr)
$\theta_{c.m.}$ (deg)
10^3
10^2
10^1
10^0
0
60
120
180

Fig. 23. Optical model fits to the ^{9}Be differential cross section data. The points are the present ^{9}Be elastic data and the curves are optical model calculations performed as described in the text.

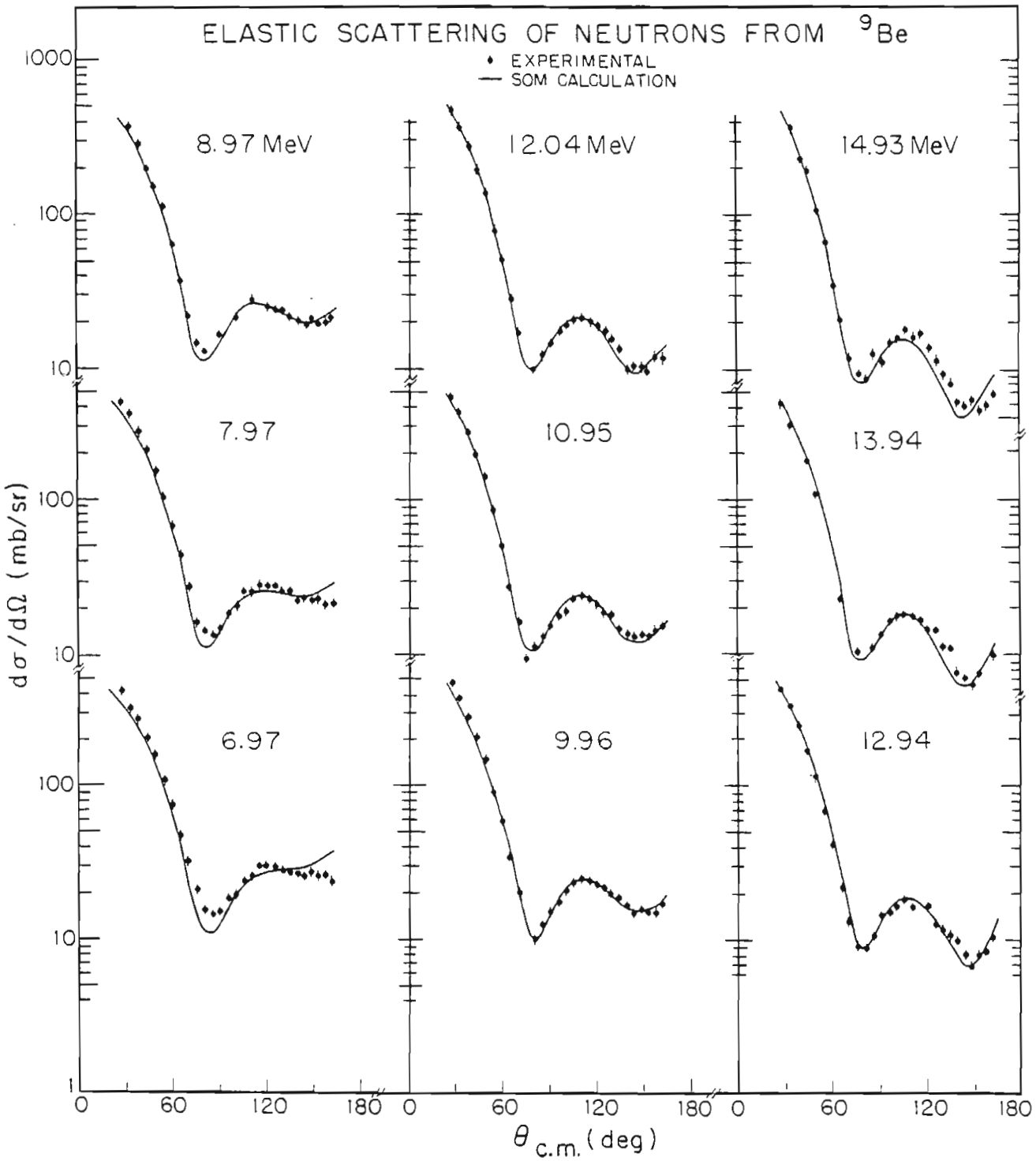
ELASTIC SCATTERING OF NEUTRONS FROM ^{9}Be
EXPERIMENTAL
SOM CALCULATION
8.97 MeV
12.04 MeV
14.93 MeV
7.97
10.95
13.94
6.97
9.96
12.94
dσ/dΩ (mb/sr)
θ c.m. (deg)
1000
100
10
1
0
60
120
180

TABLE 4

PARAMETER VALUES FROM THE ^{6}Li AND ^{9}Be

SPHERICAL OPTICAL MODEL ANALYSES[a]

Parameter	^{6}Li Analysis	^{9}Be Analysis
r_R	1.25	1.47
a_R	1.10 - 0.03E	0.39
r_I	1.50	1.21
a_I	0.88 - 0.03E	0.42
r_S	1.45	1.24
a_S	0.59	0.35
V	39.4 + 0.7E	42.4 - 0.5E
W	0.0 + 0.6E	1.0 + 0.4E
V_S	5.1	4.9

[a]The geometric parameters (r, a) are in fermis; the potential strength parameters (V, W, V_S) and the laboratory energy E are in MeV.

Fig. 24. Energy dependence of the optical potential strength and diffusness parameters in the ^{6}Li spherical optical model analysis. The real and imaginary potential radius parameters were kept fixed at the values given in table 4.

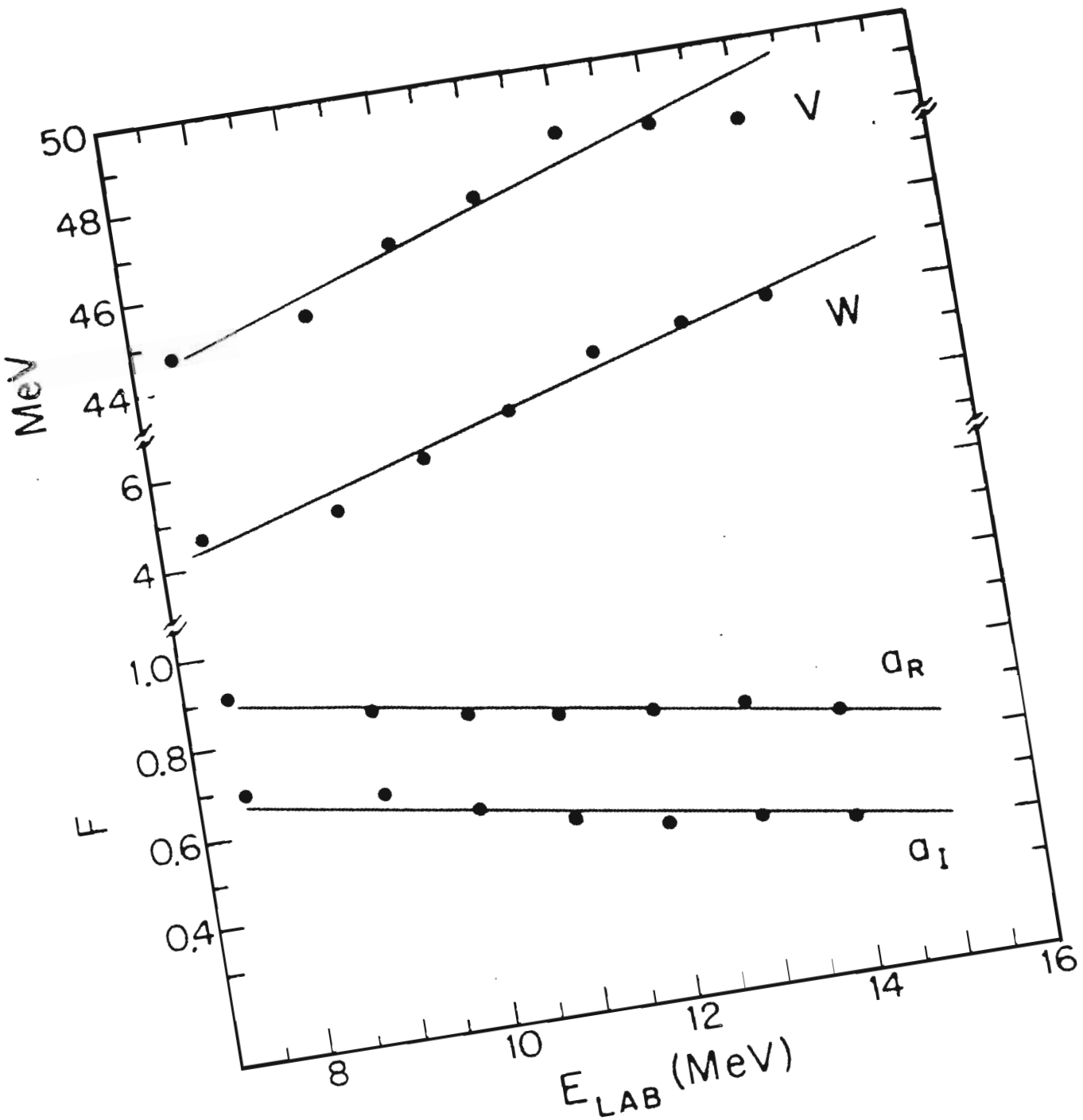
50
48
46
44
MeV
6
4
1.0
0.8
0.6
0.4
F
V
W
a_R
a_I
8
10
12
14
16
E_{LAB} (MeV)

Fig. 25. Energy dependences of the optical potential strengths in the ^{9}Be spherical optical model(SOM) and coupled-channels(CC) analyses. Other parameters were held fixed at values given in table 4. Corresponding parameter energy dependences from the global analysis of ref. 5 are also shown.

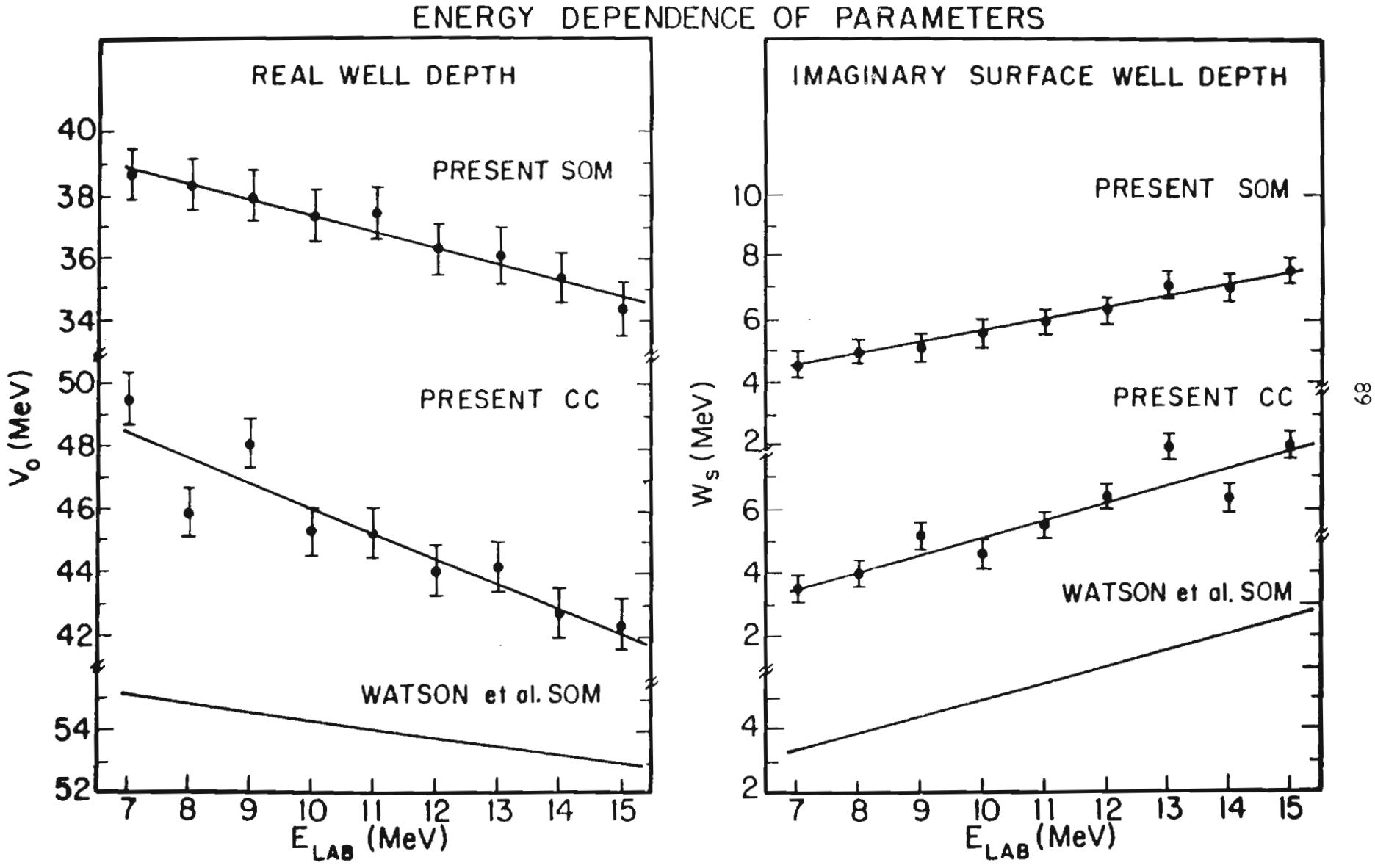
ENERGY DEPENDENCE OF PARAMETERS
REAL WELL DEPTH
PRESENT SOM
PRESENT CC
WATSON et al. SOM
V_o (MeV)
E_{LAB} (MeV)
IMAGINARY SURFACE WELL DEPTH
PRESENT SOM
PRESENT CC
WATSON et al. SOM
W_s (MeV)
E_{LAB} (MeV)

This assumption is consistent with the results of previous global CM analyses--those for A>40 and Watson's analysis in the p shell. ΔV(real well depth in ^{7}Li analysis minus real well depth in ^{6}Li analyses) and ΔW(the corresponding quantity for the imaginary well) were determined by fitting elastic differential cross section data from the Ohio University Accelerator Laboratory at 7.5 MeV[25]. The values obtained were $\Delta V=3.6\pm0.6$ and $\Delta W=1.3\pm0.4$. The errors on ΔV and ΔW are the respective changes in the V and W parameters required to double the minimum value of χ^2 from the fit to the Ohio data.

Representative ^{7}Li angular distributions, calculated with parameters from the ^{6}Li analysis and adjusted using the ΔV and ΔW values given above, are shown as the solid curves in fig. 26. The data points in that figure are the corresponding elastic + 0.478 MeV state measurements.

It is evident that the calculation reproduces the positions of maximum and minima in the scattering cross section. What remains to be shown is that the calculated curves reproduce the elastic scattering in magnitude. The integrated cross section for scattering to the 0.478 MeV state in ^{7}Li, extracted by integrating the elastic + 0.478 MeV state data and subtracting calculated elastic cross section values, is plotted vs. energy in fig. 27. The solid line in that figure represents the data of Dickens et al.[26] for excitation of the 0.478 state in a ^{7}Li(n, n'γ)^{7}Li experiment. To obtain the curve, the Dickens data was smoothed over energy intervals

Fig. 26. Optical model calculations of the differential cross section for neutron elastic scattering from ^{7}Li at 9, 11, and 13 MeV. The curves are the calculated elastic scattering, and the points are the measured elastic scattering plus scattering to the 0.478-MeV state in ^{7}Li.

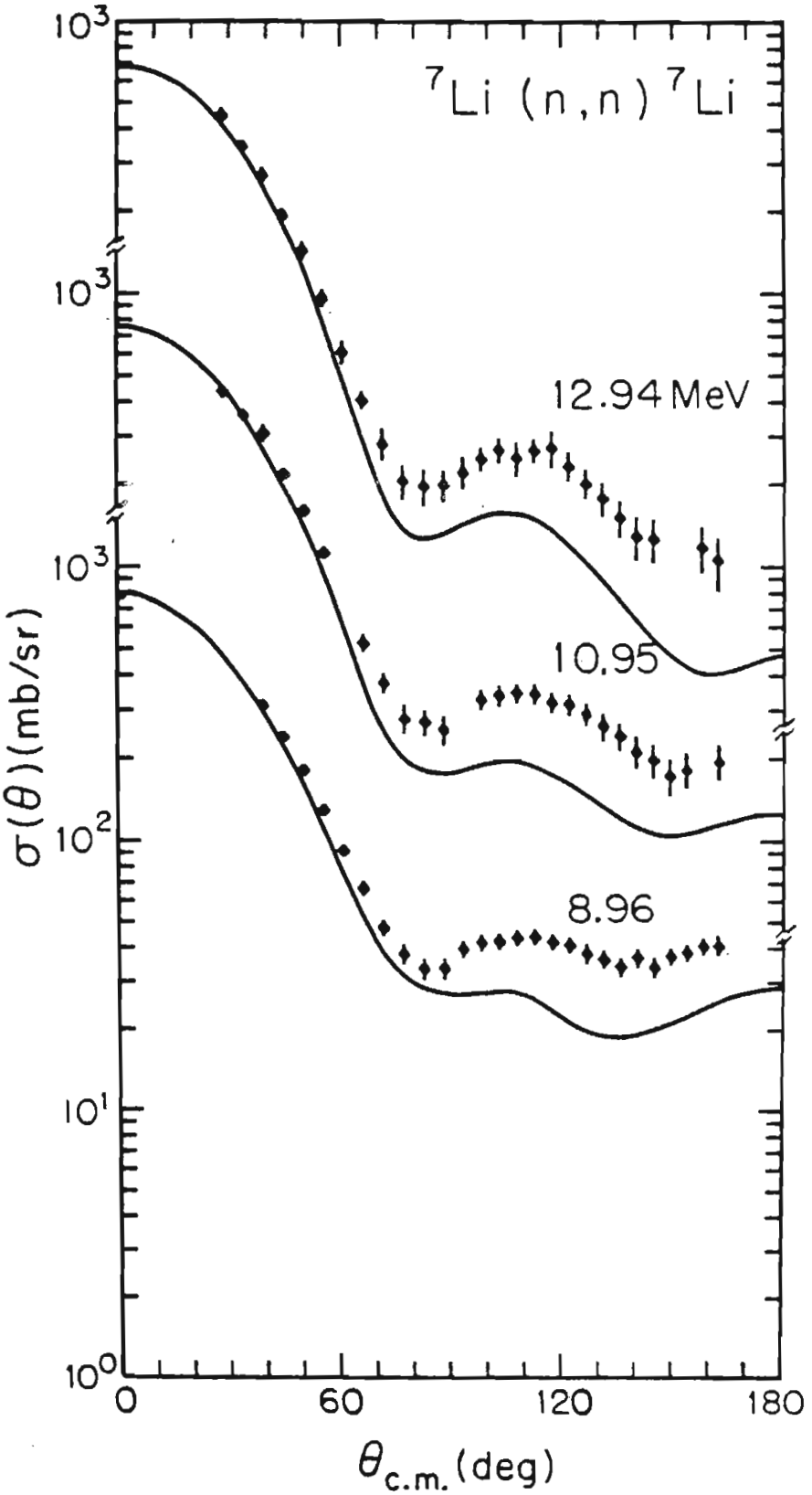
^{7}Li (n,n) ^{7}Li
12.94 MeV
10.95
8.96
$\sigma(\theta)$(mb/sr)
10^3
10^3
10^3
10^2
10^1
10^0
0
60
120
180
$\theta_{c.m.}$(deg)

Fig. 27. Cross section for neutron scattering to the 0.478-MeV state in ^{7}Li. The points are the 0.478-MeV state cross section values extracted from the present data and optical model calculations. The solid curve is from the $^{7}Li(n,n'\gamma)$ measurement of ref. 26.

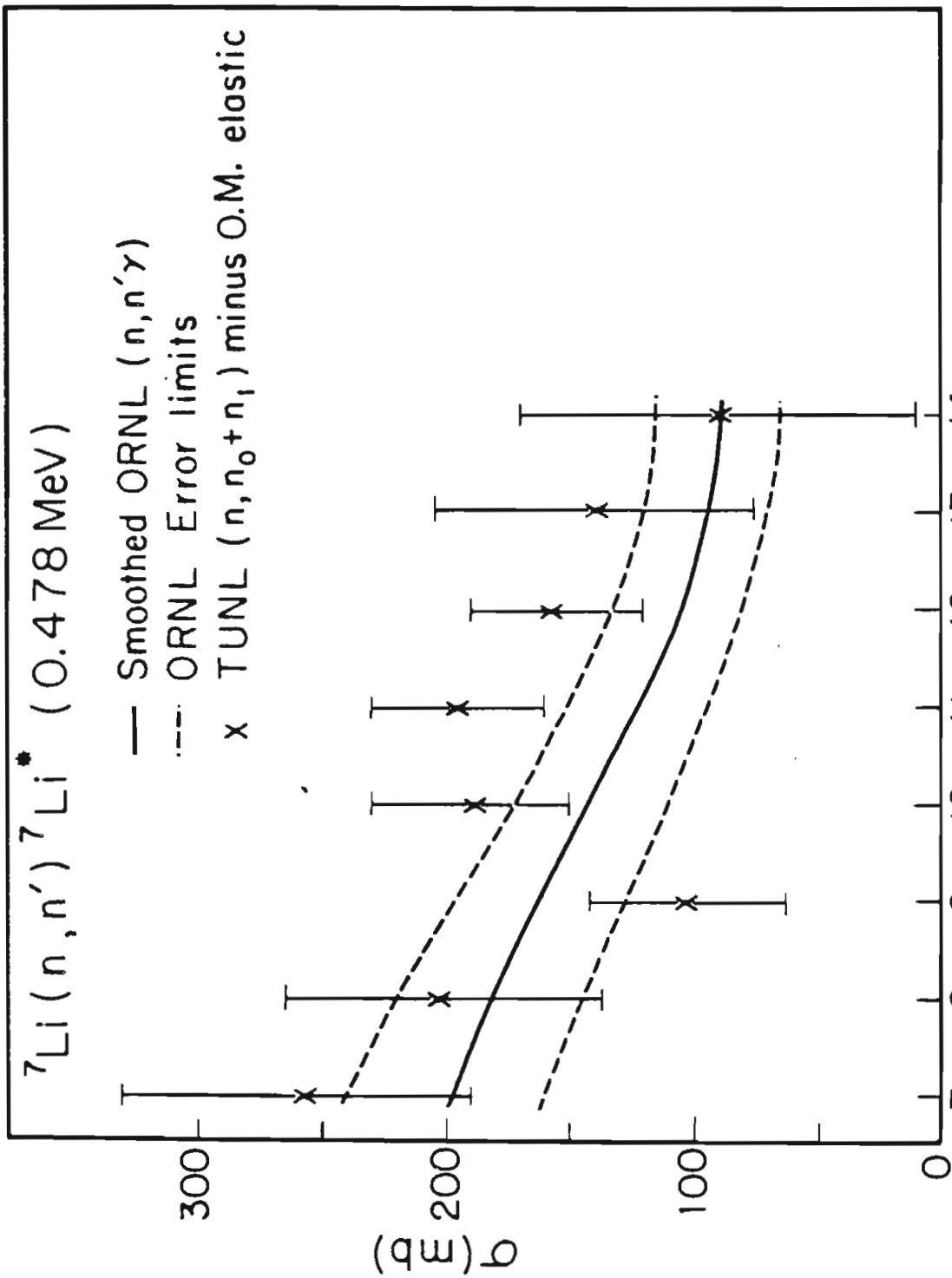
$^{7}Li(n,n')^{7}Li^{*}$ (0.478 MeV)
Smoothed ORNL (n,n'γ)
ORNL Error limits
x TUNL (n,n_0+n_1) minus O.M. elastic
σ(mb)
300
200
100
0
7
8
9
10
11
12
13
14
E_n (MeV)

approximating the energy resolution of the present measurements. The dashed curves are error limits quoted in the Dickens paper. The agreement between the $^{7}Li(n, n'\gamma)^{7}Li$ measurement and the 0.478-MeV tate cross section values extracted in the present work is generally good. This confirms that the calculated ^{7}Li angular distributions are correct in magnitude.

Near 9 MeV the present result shows evidence for resonance structure in the inelastic scattering channel. There is also a suggestion of such structure in the unsmoothed data of Dickens et al.; however, the experimental scatter in that work largely masks the effect.

Extraction of Symmetry Terms

In the Watson analysis and in the A>40 analyses which treated both neutron and proton data it has been customary to expand the real and imaginary well depths as

$$V = v_0(E) \pm v_s(N-Z)/A + v_c Z/A^{1/3} \quad \text{and}$$
$$W = w_0(E) \pm w_s(N-Z)/A + w_c Z/A^{1/3}, \qquad (4.3)$$

where $v_c = \begin{cases} 0.4 \text{ MeV, for protons} \\ 0.0 \text{ MeV, for neutrons,} \end{cases}$

$w_c = 0.0$ MeV,

$v_s = 24\text{-}27$ MeV, and

$w_s = 10\text{-}16$ MeV.

The plus signs are to be taken for proton projectiles and the minus signs for neutrons.

The present ^{6}Li, ^{7}Li, and ^{9}Be neutron scattering data offered two independent ways of extracting v_s and w_s. The adjustments ΔV and ΔW required to the ^{6}Li real and imaginary well depths, respectively, in order to describe scattering by ^{7}Li gave v_s and w_s directly. From eqs. 4.3,

$$\begin{aligned} \Delta V &= v_s[(N-Z)/A]_{^{7}Li} \text{ and} \\ \Delta W &= w_s[(N-Z)/A]_{^{7}Li}, \end{aligned} \tag{4.4}$$

giving $v_s = 25 \pm 4$ and $w_s = 9 \pm 3$ when the values of ΔV and ΔW; and N, Z, and A for ^{7}Li were supplied.

The second method for extracting v_s and w_s is less direct and involves a comparison of the neutron data with proton scattering studies. Again, using eqs. 4.3,

$$\begin{aligned} V_p - V_n &= 2v_s(N-Z)/A + v_c Z/A^{1/3} \text{ and} \\ W_p - W_n &= 2w_s(N-Z)/A + w_c Z/A^{1/3}, \end{aligned} \tag{4.5}$$

where subscripts p and n refer to neutron and proton projectiles. $V_p - V_n$ and $W_p - W_n$ may be obtained from CM analyses of neutron and proton scattering from the same nucleus at the same energy. Then, if v_c and w_c are set to their usual values of

0.4 and 0.0 MeV, respectively, eqs. 4.5 may be solved for v_s and w_s.

This procedure was applied to nucleon scattering by ^{9}Be. Votava et al.[27] analysed proton scattering from ^{9}Be for proton energies form 13 MeV to 30.3 MeV; however, the geometric parameters of that analyses differ somewhat from those of the present neutron scattering analysis for ^{9}Be. In order for a direct comparison of the well depths required for neutron and proton projectiles to be made, the proton angular distribution data at 13 and 14 MeV analysed by Votava et al. were obtained[28] and refit along with the present neutron data using the same geometric parameters for both. The fits were of only slightly poorer quality than those of the original analysis. The 14-MeV fits are shown in the upper half of fig. 28. Table 5 lists the parameter values. The proton and neutron well depths together with N, Z, and A for ^{9}Be and standard v_c and w_c values were inserted in eqs. 4.5 to obtain v_s and w_s, and the results for 13 and 14 MeV were averaged. This gave $v_s = 34 \pm 3$ MeV and $w_s = 18 \pm 4$ MeV, which disagree with the values obtained from the lithium analysis and with values from the A>40 analyses.

To try to improve the situation, the $Z/A^{1/3}$(Coulomb) terms in eqs. 4.3 were investigated. The standard values for v_c and w_c are calculated using the energy dependence of the nuclear potential. This cannot be determined accurately in mass regions where nuclear collective effects are large, such as the p shell[29].

Fig. 28. Comparisons of neutron and proton elastic differential cross sections for scattering from ^{9}Be and from ^{12}C at 14 MeV. The neutron data are from the present measurements. The proton data are from refs. 28 and 31 for ^{9}Be and ^{12}C, respectively. The curves are optical model fits performed as described in the text.

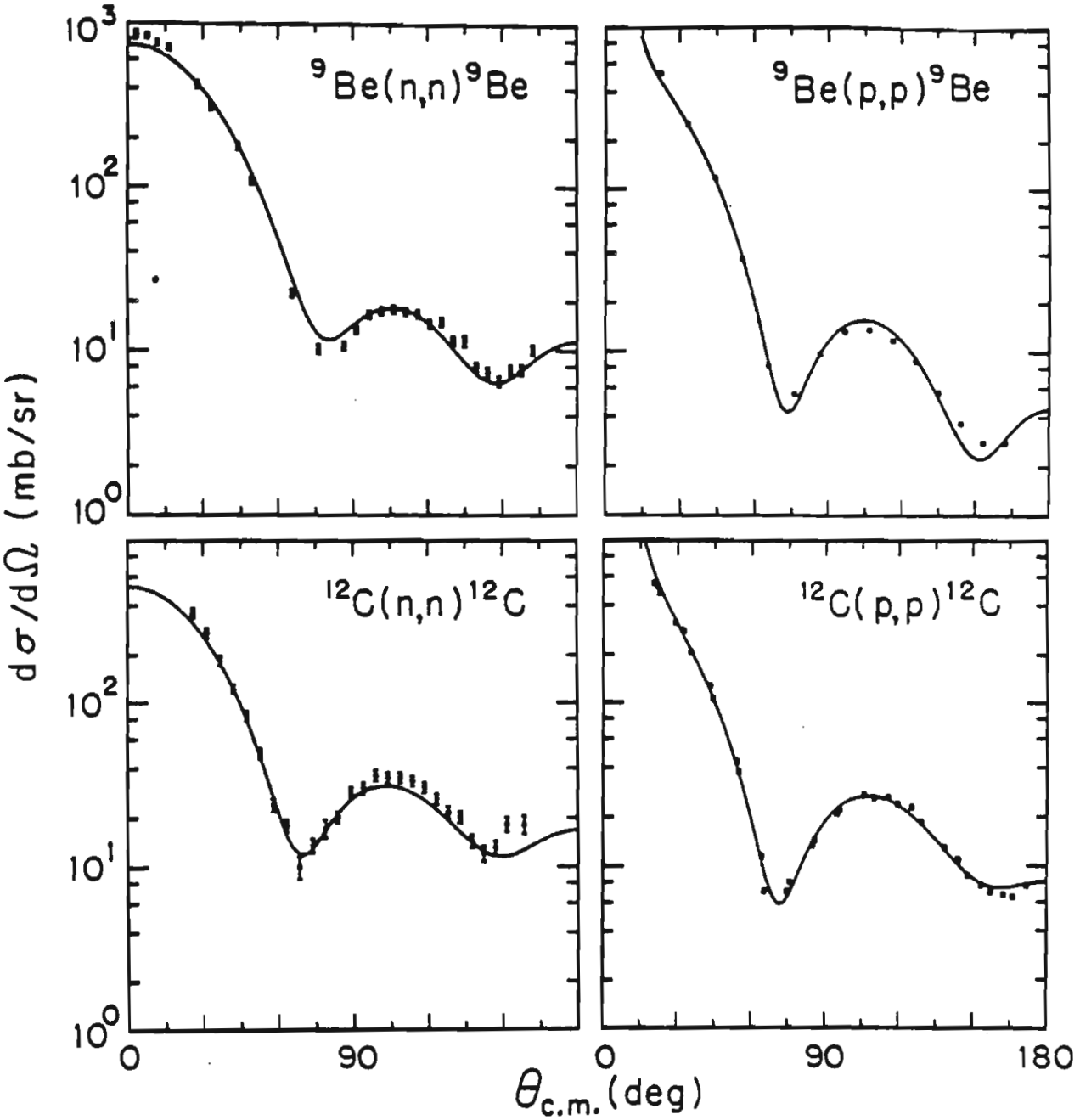
$^{9}Be(n,n)^{9}Be$
$^{9}Be(p,p)^{9}Be$
$^{12}C(n,n)^{12}C$
$^{12}C(p,p)^{12}C$
$d\sigma/d\Omega$ (mb/sr)
10^3
10^2
10^1
10^0
0
90
180
$\theta_{c.m.}$ (deg)

TABLE 5

OPTICAL MODEL PARAMETER VALUES FOR NUCLEON SCATTERING BY ^{9}Be AND ^{12}C [a]

Parameter	^{9}Be, 13 MeV	^{9}Be, 14 MeV	^{12}C, 14 MeV
r_R	1.35	1.35	1.22
a_R	0.50	0.50	0.35
r_I	1.27	1.27	1.15
a_I	0.43	0.43	0.23
r_S	1.20	1.20	1.25
a_S	0.31	0.31	0.40
r_C [b]	1.30	1.30	1.25
V_p	48.1	48.0	57.1
V_n	40.5	39.0	53.3
W_p	10.3	10.6	9.5
W_n	6.7	6.1	8.1
V_S	4.9	4.9	6.0

[a] Geometric parameters (r, a) are in fermis; potential strengths are in MeV.

[b] r_C is the Coulomb radius parameter required for proton projectiles. The Coulomb potential is that for a uniformly charged shere of radius $R = r_C A^{1/3}$.

Therefore, it was decided to determine v_c and w_c empirically by comparing neutron and proton scattering from a light nucleus for which N=Z.

Nodvik et al.[30] found that proton scattering by carbon could be fit with an optical model above about 12 MeV. The present neutron data for 14 MeV neutrons elastically scattered by carbon and the proton scattering data of Peele[31] at that energy were simultaneously fit with the OM using the same procedure as used in the beryllium case. The resulting fits obtained are shown in the lower half of fig. 26 and the parameter values from the fits are given in table 5. Applying eq. 4.5 gave $v_c = 1.4 \pm 0.4$ MeV and $w_c = 0.5 \pm 1.0$ MeV.

Substituting these values for the standard ones for determining v_s and w_s led to the following results: $v_s = 25 \pm 4$ MeV and $w_s = 17 \pm 9$ MeV. These values for the coefficients of the symmetry terms now agree with those obtained for other nuclei--both for A>40 and in the p shell. However, non-standard values for the Coulomb terms in the real and imaginary wells had to be admitted.

Coupled-Channels Analyses

Elastic scattering and inelastic scattering to the 2.43-MeV state in ^{9}Be have been analysed together in the rotational coupled-channels model of Tamura[6]. Likewise, elastic and inelastic scattering to the 4.44-MeV state in ^{12}C have been analysed using the same model. These are nuclei for

which Hartree-Fock calculations predict large permanent deformations.[32].

Tamura's model provides for a symmetric deformation of the optical potintial. This not only gives a more realistic optical pctential than eq. 4.1 for neutron elastic scattering from deformed nuclei, but it also produces coupling to inelastic channels. The technique for including the deformation is to make $R=r_\lambda A^{1/3}$ of eq. 4.1 angle dependent as fcllows:

$$R(\theta) = R_o\{1 + \sum_{\lambda=o}^{\ell_{MAX}} \beta_\lambda Y_\lambda^o(\theta)\} \qquad (4.6)$$

Here $\{Y_\lambda^o\}$ are spherical harmonics and $\{R_o, \beta_\lambda\}$ are expansion parameters.

The calculations were performed using a modified version[33] cf computer program JUPITOR-I by Tamura[7]. Only the first two terms of eq. 4.6. were used. Also, only the first coupling term in the Legendre polynomial expansion of eq. 4.1 with eq. 4.6 included was kept; however, complex coupling was allowed.

The fitting procedure and parameter restrictions used in the CC analyses were the same as those used in the OM analyses already described, with the exception that one additional parameter, the quadrupole deformation parameter β_2 had to be included in the parameter space. Starting parameters for the ^{9}Be neutron analysis were frcm a similar proton CC analysis for ^{9}Be by Votava et al.[27]. A previous analysis of neutron

scattering from ^{12}C at 14.1 MeV by Grin et al.[34] gave starting parameters for the ^{12}C CC analysis.

Typical fits obtained for ^{9}Be are shown in figs. 29, 30, and 31; and those for ^{12}C are shown in figs. 32 and 33. Parameter values from the analyses are given in table 6. The parameters from the Votava proton scattering analysis at 13 and 14 MeV and from the neutron analysis by Grin are also given there. The parameters from the present neutron CC analysis for ^{9}Be are in much closer agreement with those of the proton CC analysis by Votava than were the parameter sets in the corresponding spherical OM analyses. However, this may not be significant since parameter ambiguities exist and the methods used for searching the parameter spaces in the neutron and proton analyses were not necessarily the same. Plots of the energy dependence of the real and imaginary well depths in the present CC analyses for ^{9}Be and ^{12}C, are given in figs. 25 and 34, respectively. The solid lines on these figures are the result of linear fits to the energy dependences. These have the typical behavior seen in the Watson and A>40 OM analyses.

Study of Deformation Effects

The present CC analyses of scattering by ^{9}Be and ^{12}C confirm the results of other nucleon scattering studies that scattering to low-lying states in these nuclei is consistent with a collective rotational description of these states. The ^{9}Be analysis is of particular interest for comparison with the

Fig. 29. Coupled-channels fits tc the present elastic and inelastic scattering data for ^{9}Be for energies near 7, 8, and 9 MeV.

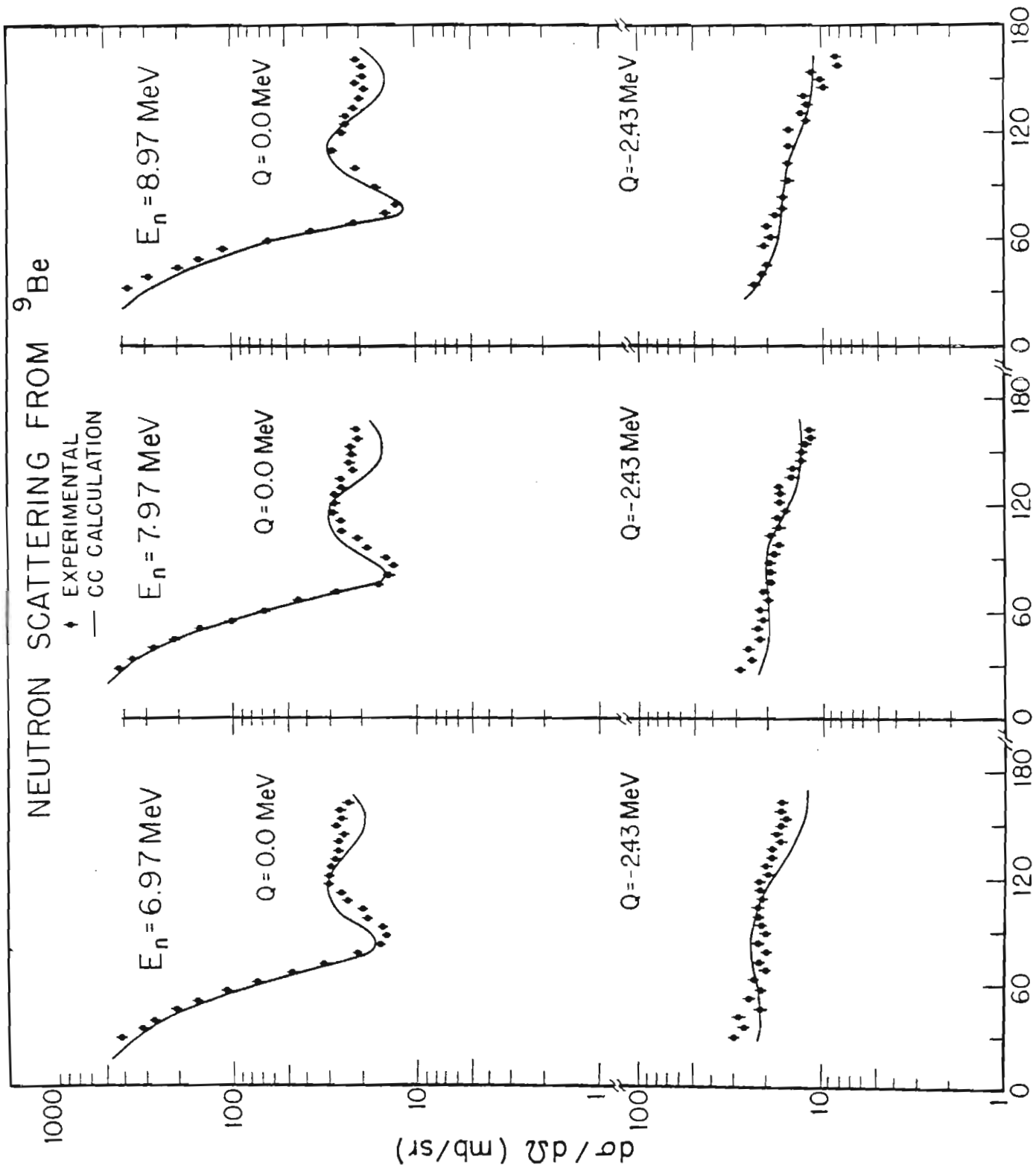
NEUTRON SCATTERING FROM ^{9}Be
EXPERIMENTAL
CC CALCULATION
E_n = 6.97 MeV
Q = 0.0 MeV
Q = -2.43 MeV
E_n = 7.97 MeV
Q = 0.0 MeV
Q = -2.43 MeV
E_n = 8.97 MeV
Q = 0.0 MeV
Q = -2.43 MeV
$d\sigma / d\Omega$ (mb/sr)
$\theta_{c.m.}$ (deg)

Fig. 30. Coupled-channels fits to the present elastic and inelastic scattering data for ^{9}Be for energies near 10, 11, and 12 MeV.

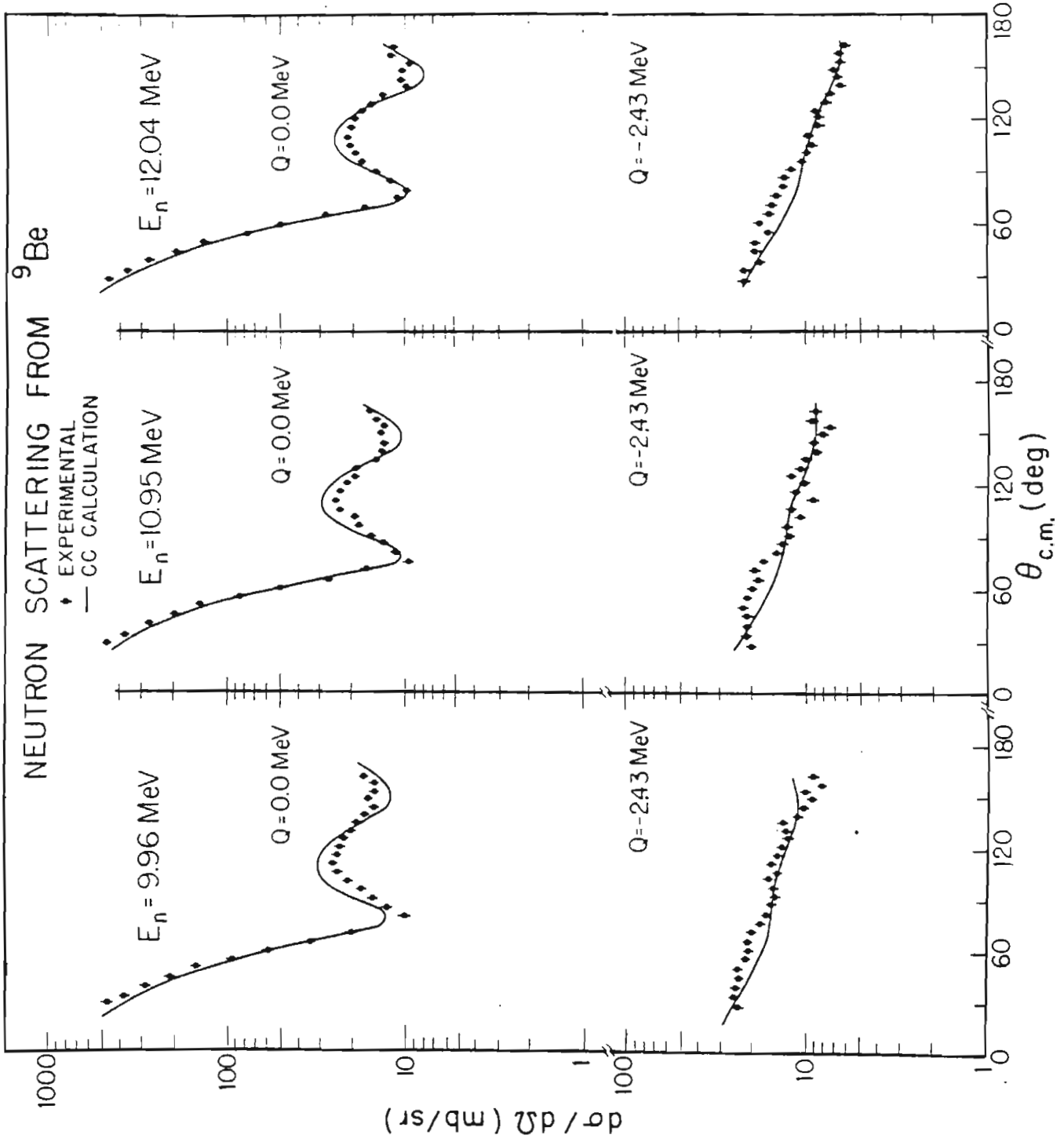
NEUTRON SCATTERING FROM ^{9}Be
EXPERIMENTAL
CC CALCULATION
E_n = 9.96 MeV
E_n = 10.95 MeV
E_n = 12.04 MeV
Q = 0.0 MeV
Q = -2.43 MeV
$d\sigma/d\Omega$ (mb/sr)
$\theta_{c.m.}$ (deg)

Fig. 31. Coupled-channels fits to the present elastic and inelastic scattering data for ^{9}Be for energies near 13, 14, and 15 MeV.

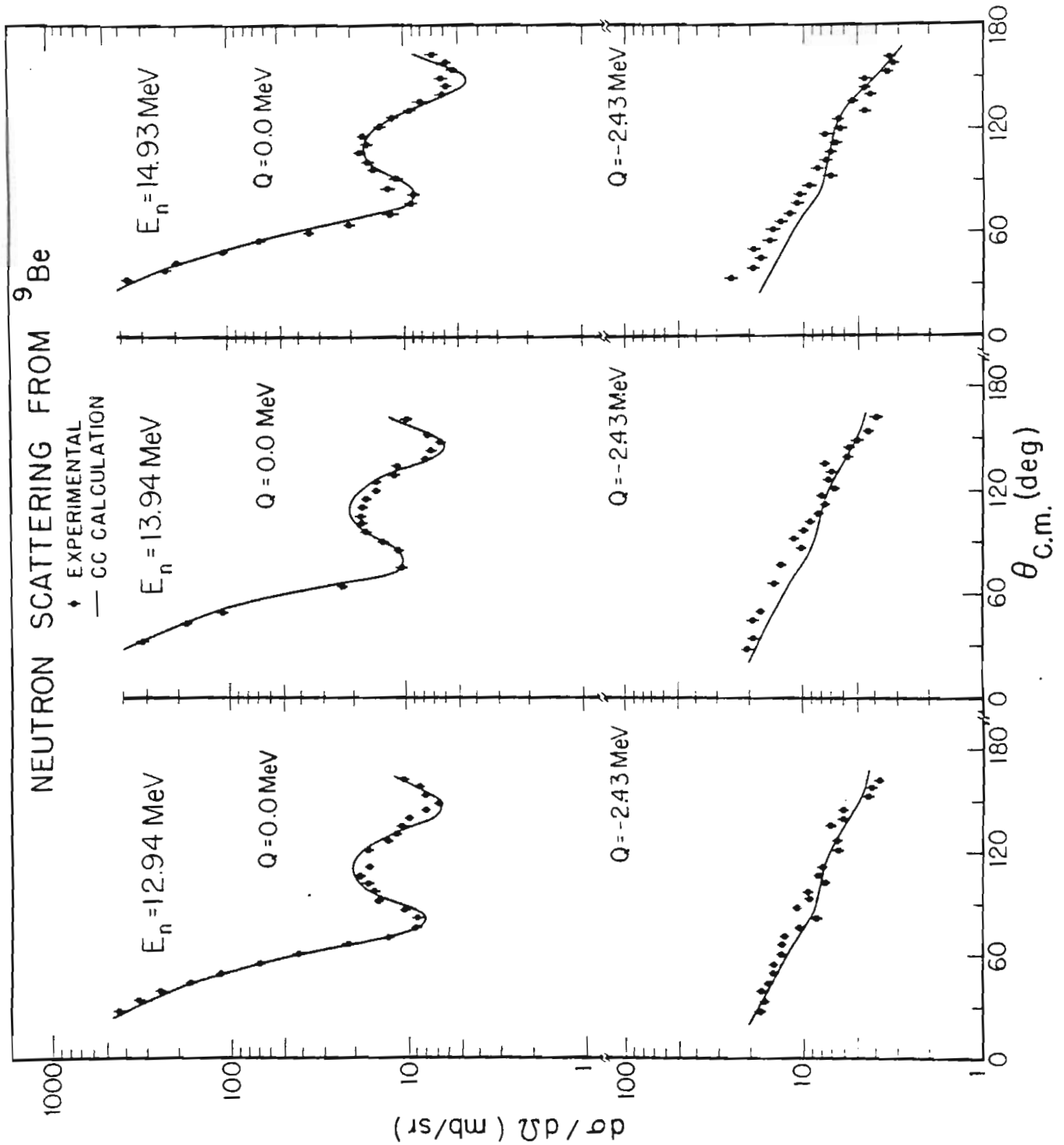
NEUTRON SCATTERING FROM ^{9}Be
EXPERIMENTAL
CC CALCULATION
E_n = 12.94 MeV
E_n = 13.94 MeV
E_n = 14.93 MeV
Q = 0.0 MeV
Q = -2.43 MeV
$d\sigma / d\Omega$ (mb/sr)
$\theta_{c.m.}$ (deg)
1000
100
10
1
0
60
120
180

Fig. 32. Coupled-channels fits to the present elastic and inelastic scattering data for ^{12}C for energies near 9, 10, and 11 MeV.

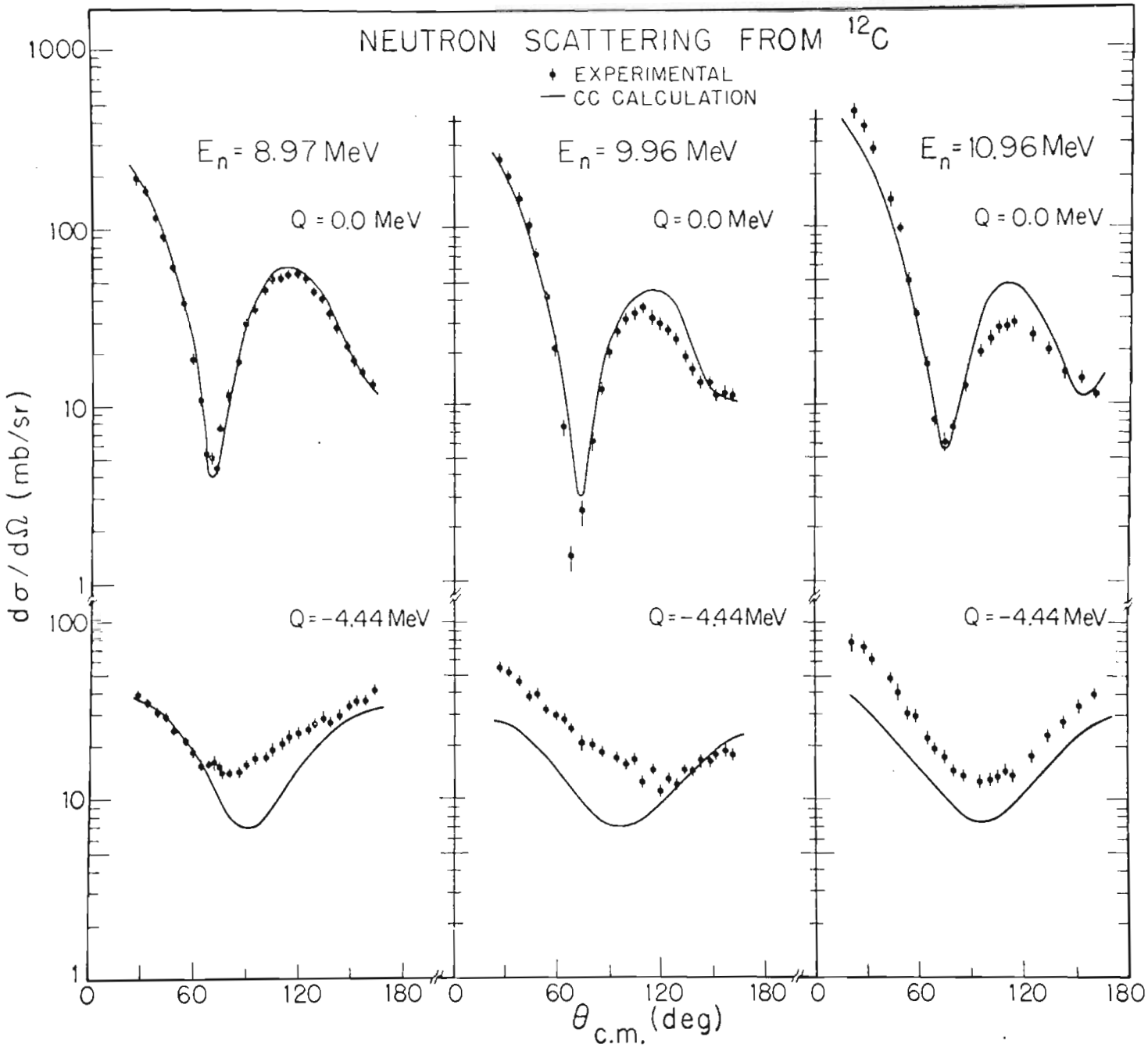
NEUTRON SCATTERING FROM ^{12}C
EXPERIMENTAL
CC CALCULATION
E_n = 8.97 MeV
E_n = 9.96 MeV
E_n = 10.96 MeV
Q = 0.0 MeV
Q = −4.44 MeV
$d\sigma / d\Omega$ (mb/sr)
$\theta_{c.m.}$ (deg)
1000
100
10
1
0
60
120
180

Fig. 33. Coupled-channels fits to the present elastic and inelastic scattering data for ^{12}C for energies near 12, 14, and 15 MeV.

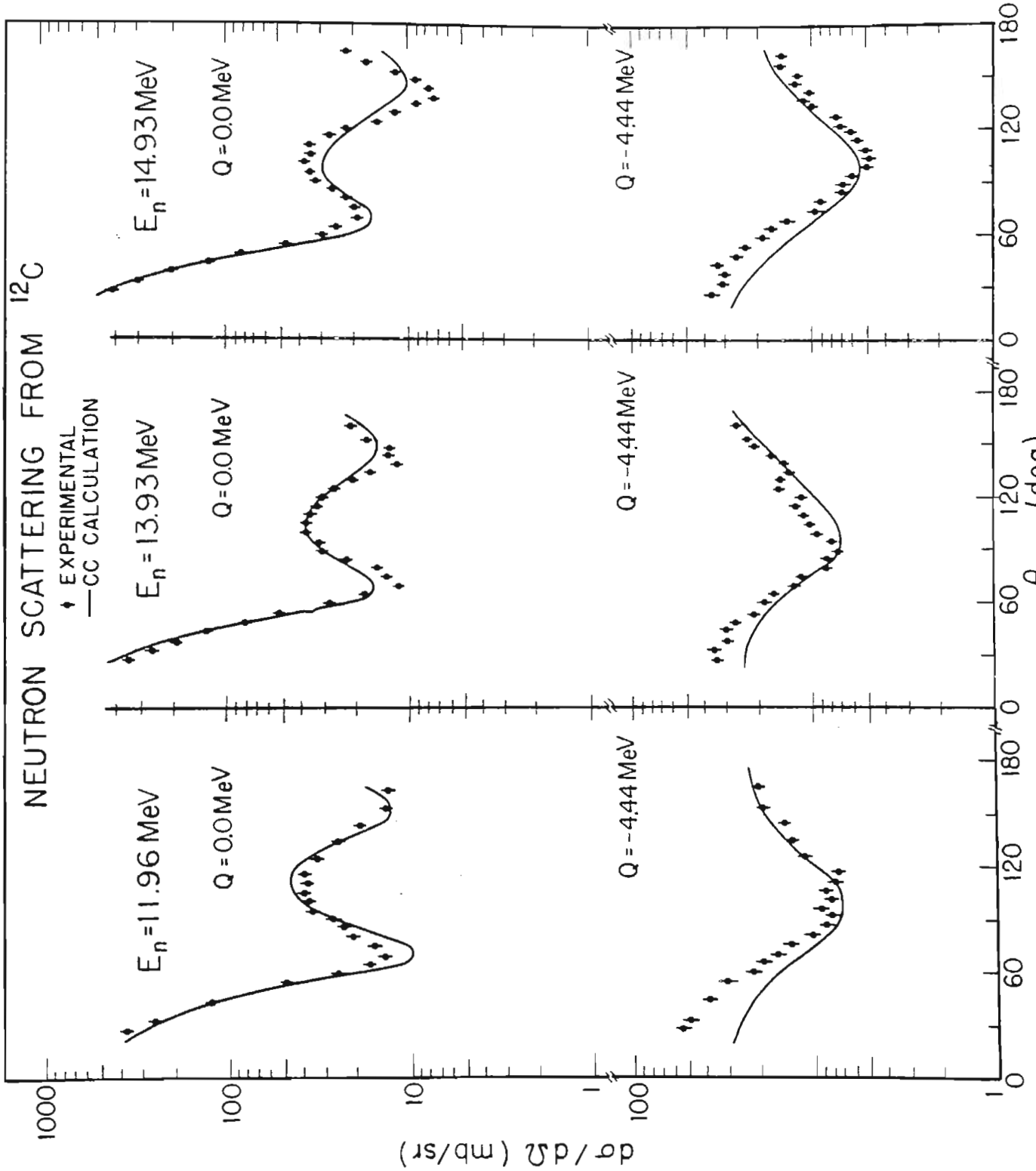
NEUTRON SCATTERING FROM ^{12}C
EXPERIMENTAL
CC CALCULATION
E_n=11.96 MeV
Q=0.0 MeV
Q=-4.44 MeV
E_n=13.93 MeV
Q=0.0 MeV
Q=-4.44 MeV
E_n=14.93 MeV
Q=0.0 MeV
Q=-4.44 MeV
$d\sigma/d\Omega$ (mb/sr)
$\theta_{c.m.}$ (deg)

TABLE 6

PARAMETER VALUES FROM THE ^{9}Be AND ^{12}C COUPLED-CHANNELS ANALYSES[a]

Parameter	^{9}Be Analysis	^{12}C Analysis
r_R	1.17	1.25
a_R	0.54	0.35
r_I	1.21	1.25
a_I	0.20	0.20
r_S	1.20	1.25
a_S	0.31	0.35
V	53.9 - 0.8E	58.0 - 0.9E
W	-0.20 +0.54E	0.28E
V_S	4.9	5.0
β_2	1.06	-0.64

[a] Geometric parameters (r, a) are in fermis; potential strengths (V, W, V_S) and laboratory energy E are in MeV.

Fig. 34. Energy dependences of the real and imaginary optical potential strengths for ^{12}C. The solid circles are the real and imaginary potential strengths from the present CC analysis of the carbon data. The lines are the result of a least squares fit. Also shown(open circles) are the values of V and W from the analysis of ref. 34 at 14 MeV.

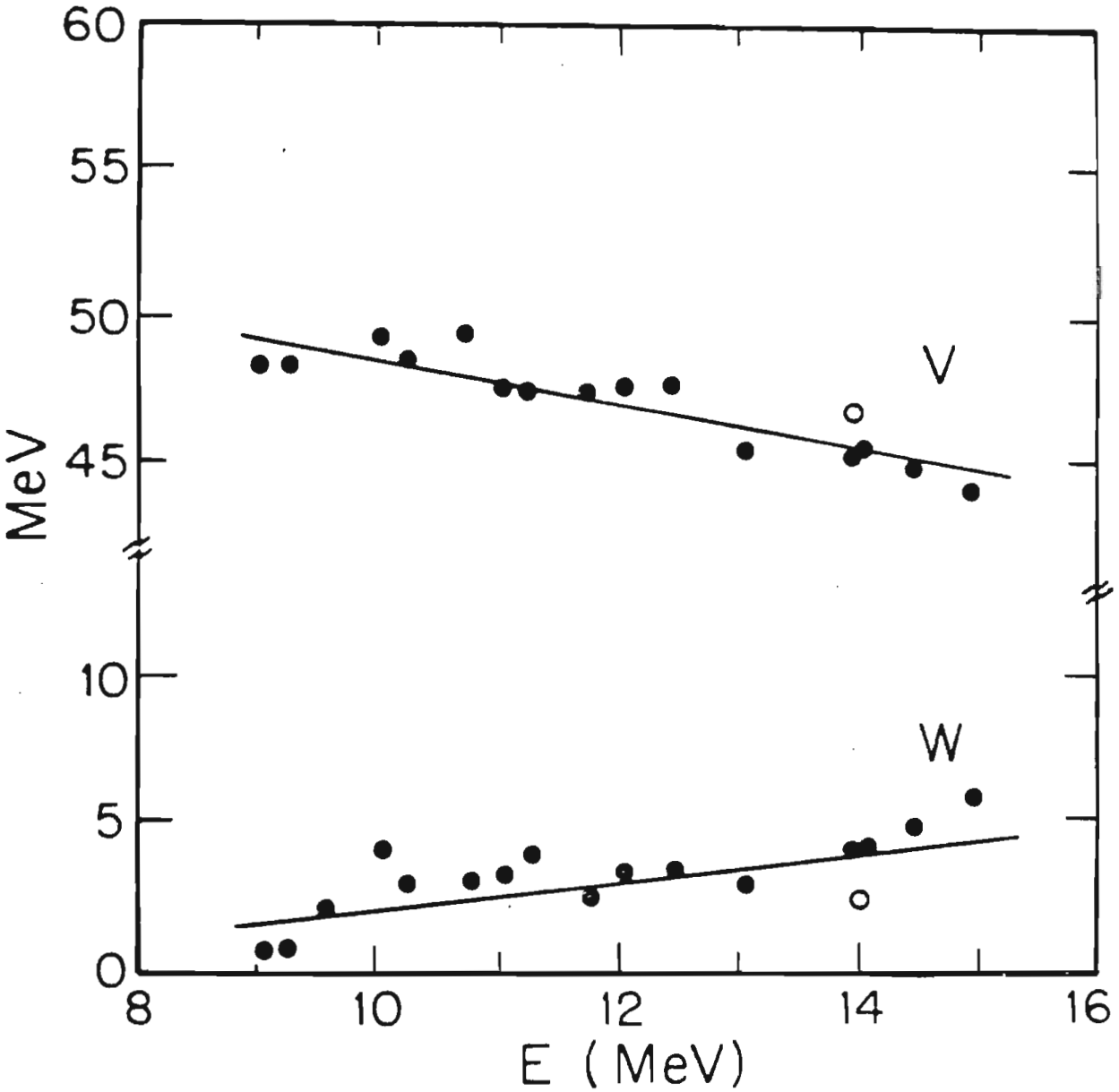
60
55
50
45
10
5
0
MeV
V
W
8
10
12
14
16
E (MeV)

proton CC analysis of Votava to test for the presence of two effects of the nuclear deformation: A difference between the quadrupole deformation parameters for neutron and proton projectiles may exist, and the extraction of symmetry terms in the real and imaginary OM potential strengths through the comparison of neutron and proton scattering from a nucleus may be affected by the presence of a nuclear deformation.

Madsen et al.[35] showed that the quadrupole deformation parameter β_2 should be different for proton and neutron projectiles. The present neutron scattering analysis gave β_2=1.06 while Votava's proton scattering analysis gave β_2=1.10, so there is an apparent effect. However, Thompson[36] has refit some of the proton data included in the Votava analysis using complex coupling rather than real coupling, which was used in the original analysis. The deformation parameter preferred in the reanalysis was β_2=1.05, with an estimated uncertainty of about 5%. Therefore no disagreement between β_2 parameters extracted from neutron and proton scattering by ^{9}Be is seen within error.

A recent paper by Lachkar et al.[37] reported OM and CC analyses for the even-A selenium isotopes. The authors concluded that the differences in nuclear deformation among the various isotopes had a strong influence upon the OM symmetry terms extracted in the spherical OM analysis. No effect of this type was considered in the present analysis of neutron scattering by the lithium isotopes because the previously-cited

Hartree-Fock calculations[32] gave practically no difference in deformation for ^{6}Li and ^{7}Li.

An analogous effect might occur in the extraction of CM symmetry terms by the comparison of neutron and proton scattering from the same nucleus if deformations of the neutron and proton mass distributions in the nucleus are slightly different. Such an effect would be most important for a nucleus like ^{9}Be, where the nuclear deformation is large enough to substantially affect the elastic scattering through coupling it to discrete inelastic scattering channels.

An effect of this type was sought in nucleon scattering by ^{9}Be at 13 MeV. The geometric and spin-orbit parameters of the proton CC analysis by Votava et al. for that energy were taken, and the real and imaginary well depths were adjusted to best fit the present 13 MeV data for neutron elastic scattering from ^{9}Be and scattering to the 2.43-MeV state. The fits obtained were only slightly worse than those shown in fig. 31. The parameter adjustments required were $V_p - V_n = 5.4$ MeV and $W_p - W_n = 2.8$ MeV.

Eq. 4.5 were solved for v_s and w_s using the real and imaginary potential adjustments given above. Standard values for the Coulomb-term coefficients of $v_c = 0.4$ MeV and $w_c = 0.0$ MeV were used. The results were $v_s = 20 \pm 3$ MeV and $w_s = 13 \pm 4$ MeV. These values for the symmetry coefficients are in satisfactory agreement with the standard values and with the results from the comparison of neutron scattering from the lithium isotopes.

Further, it is of interest that this agreement was achieved without the necessity of using nonstandard values for the Coulomb coefficients v_c and w_c. Thus, it appears important in some cases to include the effects on the elastic scattering of strong coupling to inelastic states in order to properly extract CM symmetry terms using the present technique.

CHAPTER V

SUMMARY

An extensive set of elastic and discrete inelastic neutron scattering data were obtained in the energy region 7-14 MeV for four p-shell elements. Spherical optical model analyses were performed for the ^{6}Li, ^{7}Li, and ^{9}Be data and the symmetry terms in the real and imaginary potential depths were investigated. Coupled channels calculations were performed for the elastic and inelastic scattering data for ^{9}Be to investigate strong-coupling effects on the extraction of symmetry terms and to compare deformation parameters for neutron and proton projectiles. Coupled channels calculations were also performed for the ^{12}C data to extend the results of a previous study.

The values found for the symmetry terms from the ^{6}Li-^{7}Li analysis were in agreement with previous work in light and heavy mass regions. The symmetry terms from comparison of neutron and proton scattering from ^{9}Be could be brought into similar agreement with previous work either by allowing non-standard values for the Coulomb-correction terms in the well depths or by taking into account strong-coupling effects.

There exist other possibilities for the studying of nuclear structure and reactions using the present neutron scattering data. Development of a different type of CC

treatment for the light isotopes studied here is under consideration. The calculations would use α-cluster wave functions for describing the nuclear states rather than rotational wave functions. This would permit a study of α-clustering in light nuclei. Also planned is an R-matrix analysis of the ^{12}C data with background phase shifts taken from the present CC calculations. This may add to the current knowledge of the ^{12}C level scheme.

APPENDIX I

DETECTOR RELATIVE EFFICIENCY DETERMINATION

Neutron differential cross sections obtained in the present work were normalized to the $^1H(n,n)^1H$ differential cross section. The method required knowledge of the relative efficiency of the neutron detector $\mathcal{E}(E)$ for neutron energies between 2 and 15 MeV. A measurement of this quantity was made using the same experimental geometry as used in the scattering studies so that detector shielding and collimation effects and neutron attenuation in the sample-to-detector air column would be implicitly included. Twenty-six efficiency points were measured in the energy interval and a polynomial fit to the data was generated. An approximate expression for the error on the efficiency ratio $\mathcal{E}(E_1)/\mathcal{E}(E_2)$ was obtained directly from the data using a numerical technique. This appendix describes the experimental method, data reduction techniques, and results.

The detector relative efficiency was determined by measuring the response function of the detector to neutrons from the $D(d,n)^3He$ reaction. An incident deuteron energy of 12.3 MeV was chosen for the experiment. There are two reasons for this choice. At that deuteron energy the entire 2 to 15 MeV neutron energy range could be covered by varying the neutron detector angle between 0° and 160°. More importantly, the $D(d,n)^3He$ differential cross section is accurately known at

that energy from the measurements of Drosg and Drake[38] and Jarmie and Jett[39]. The data of Jarmie and Jett, having normalization uncertainty less than 1%, was converted to $D(d,n)^3He$ data and used to renormalize the $D(d,n)^3He$ data of Drosg and Drake. The results were fit with a Legendre polynomial series and tables of lab cross sections were obtained from the fit.

In order to perform the efficiency measurements, only minor changes were required in the experimental apparatus used in the scattering studies: The shadow bar was removed. An extender was inserted in the beam pipe to position the gas cell at the center of rotation of the detector. The monitor detector collimator was reoriented to the view the gas cell at its new position. Finally, the neutron count rate was reduced to acceptable levels by lowering the frequency of the auxiliary chopper (hence the pulse repetition rate) by a factor of from 2 to 8.

Experimental procedure was similar to the scattering runs. The electronic bias was set at the ^{137}Cs Compton edge and carefully monitored. Time-of-flight spectra were taken for a series of 26 main detector angles chosen to give about 0.5 MeV steps in neutron energy. This set of data was repeated for a consistency check. Additional spectra were taken to check the zero of the goniometer table. These were for angles of 5°, 10°, 15°, and 20°, both left and right of the beam direction. No significant zero offset was detected.

Main and monitor time-of-flight spectra were analysed following the procedure for treating scattering difference spectra. After main D(d,n)He group yields were normalized to the same arbitrary monitor count, the two angular distributions taken were found to be consistent and were averaged. The resulting set of normalized yield vs. angle data was converted to relative efficiency vs. energy data through division by the appropriate laboratory D(d,n)^{3}He cross section value. Neutron energies were determined from the kinematics of the D(d,n)^{3}He reaction. The results are shown in fig. 10.

A smooth fit to the data was obtained for use in eq. 3.2. The data set was broken into two subsets: one containing data for energies below 6 MeV and one containing the higher energy data. A polynomial was fit to each data subset. The two curves matched smoothly at the 6-MeV break point. The solid curve shown in fig. 10 is the result of the fitting procedure.

The error on the relative efficiency function was estimated to be 2.5% at each of the data points. This estimate included counting statistics, estimated errors from background subtraction of main and monitor yields, and estimated error on the D(d,n)^{3}He cross section.

The quantity of interest for the reduction of the scattering data is the ratio of efficiency values for two neutron energies, $\mathcal{E}(E_1)/\mathcal{E}(E_2)$. A numerical technique was used

to estimate the error on this quantity directly from the experimental data. A set of 10,000 curves were generated using a random number algorithm but subject to restrictions that each curve be smooth and pass within experimental error of all data points. The smoothness condition was insured by using a cubic spline interpolation routine to produce the curves. For pairs of energies (E_1, E_2), $\varepsilon(E_1)/\varepsilon(E_2)$ was calculated from each curve and the error Δ on the quantity was estimated from the standard deviation about the mean value. A good approximation to the numerical error estimate is

$$\Delta = \begin{cases} 2.5\% & \text{for } \delta > 1 \text{ MeV} \\ 2.5\,\delta\,\% & \text{otherwise} \end{cases} \qquad (A1.1)$$

where δ is the absolute difference between E_1 and E_2 in MeV.

In summary, the relative efficiency of the main neutron detector, including effects of the collimation and shielding system and neutron attenuation in the sample-to-detector air column was measured in an auxiliary experiment. A smooth fit to the data for use in reducing scattering data was generated and error estimates were made.

APPENDIX II

MONTE CARLO DATA CORRECTION METHODS

The derivation of point geometry neutron angular distributions from experimental(finite geometry) angular distributions involves the inversion of a complicated multi-dimensional integral expression. A numerical technique employing the Monte Carlo method was used to correct the present data. This appendix details the problem, describes a computational technique for its solution, and discusses the development and operating characteristics of the computer program used to make the calculations.

Problem Detail

In a neutron scattering experiment, neutrons having a finite spread in their energies are incident on the sample from the neutron source. These scatter through a finite range of angles to the detector volume. In addition, multiple scattering and attenuation effects distort the measured cross sections. What is measured is an effective average differential cross section for scattering of neutrons of average energy E to some average angle θ. This may be calculated as follows:

$$\frac{d\sigma_c}{d\Omega}(E,\theta) = \frac{\sum_{t=t_1}^{t_2} N(E,\theta,t,\Delta t)}{F(E)\,\Omega\,\varepsilon(E')} \quad . \qquad (A2.1)$$

The symbols appearing in eq. A2.1 are as follows:

$N(E,\theta,t,\Delta t)$ — Normalized time-of-flight spectrum, defined as the average number of neutrons per source pulse scattered by the sample and detected in time bin Δt at time t after the pulse left the source

t_1, t_2 — Limits of the time "window" for the arrival of the elastically- or inelastically-scattered neutron groups at the detector

Ω — Detector solid angle

$\varepsilon(E')$ — Efficiency of the detector at the energy of the scattered neutron group of interest E'

$F(E)$ — Average incident neutron flux per source pulse occurring in the sample in the absence of attenuation by the sample material

F(E) is an average over all possible neutron production and scattering sites.

$$F(E) = \int dE_o\, F_o(E_o) \iiint n_s\, d^3r_s \iiint V^{-1} d^3r_1\, \frac{d\sigma_s}{d\Omega}(E_o,\phi)\, r_{s1}^{-2} \qquad (A2.2)$$

$F_o(E_o)$ — Flux of charged particles (number/normal area) per unit energy per beam pulse in the pulsed beam which induces the neutron-producing reaction

n_s	Nuclear density of the target material upon which the beam is incident
$\vec{r}_s, \vec{r}_1, r_{s1}$	Points in the active source volume, in the scatterer, and distance between them
ϕ	Angle that the line through $\vec{r}_s$ and $\vec{r}_1$ makes with the beam direction
V	The sample volume

The average energy E may be calculated from

$$E = \int dE_o\, F_o(E_o) \iiint n_s\, d^3r_s \iiint V^{-1} d^3r_1 \frac{d\sigma_s}{d\Omega}(E_o,\phi)\, r_{s1}^{-2} E_1 / F(E) . \qquad (A2.3)$$

Here, E_1 is the energy of neutrons produced at angle ϕ in the reaction of beam particles of energy E_o in the source. An expression for the average scattering angle θ will be given below.

The time-of-flight spectra $N(E,\theta,t,\Delta t)$ of eq. A2.1 are sums of contributions from single, double, and higher order scattering processes in the sample.

$$N(E,\theta,t,\Delta t) = \sum_{i=1}^{\infty} N_i(E,\theta,t,\Delta t) \qquad (A2.4)$$

The various terms on the right in eq. A2.4 are

$$N_1(E,\theta,t,\Delta t) = \int dt_o\, f(t_o) \int dE_o\, F_o(E_o)$$
$$\iiint n_s\, d^3r_s \iiint n\, d^3r_1 \frac{d\sigma_s}{d\Omega}(E_o,\phi)\; r_{s1}^{-1} \exp\{-\Sigma(E_1)\, d_1\}$$
$$\iint d\Omega \frac{d\sigma_1}{d\Omega}(E_1,\theta_D) \exp\{-\Sigma(E_D)\, d_D\}\; \mathcal{E}(E_D),$$

$$N_2(E,\theta,t,\Delta t) = \int dt_o\, f(t_o) \int dE_o\, F_o(E_o)$$
$$\iiint n_s\, d^3r_s \iiint n\, d^3r_1 \frac{d\sigma_s}{d\Omega}(E_o,\phi)\; r_{s1}^{-1} \exp\{-\Sigma(E_1)\, d_1\}$$
$$\iiint n\; d^3r_2 \frac{d\sigma_1}{d\Omega}(E_1,\theta_1)\, d_{12}^{-2} \exp\{-\Sigma(E_2)\, d_2\}$$
$$\iint d\Omega \frac{d\sigma_2}{d\Omega}(E_2,\theta_D) \exp\{-\Sigma(E_D)\, d_D\}\; \mathcal{E}(E_D),$$

$$\ldots,$$

$$N_i(E,\theta,t,\Delta t) = \int dt_o\, f(t_o) \int dE_o\, F_o(E_o)$$
$$\iiint n_s\, d^3r_s \iiint n\, d^3r_1 \frac{d\sigma_s}{d\Omega}(E_o,\phi)\; r_{s1}^{-1} \exp\{-\Sigma(E_1)\, d_1\}$$
$$\iiint n\; d^3r_2 \cdots \iiint n\; d^3r_i \frac{d\sigma_{i-1}}{d\Omega}(E_{i-1},\theta_{i-1})\, d_i^{-2} \exp\{-\Sigma(E_i)\, d_i\}$$
$$\iint d\Omega \frac{d\sigma_i}{d\Omega}(E_i,\theta_D) \exp\{-\Sigma(E_D)\, d_D\}\; \mathcal{E}(E_D),$$

$$\ldots \qquad \text{(A2.5)}$$

The symbols used in eqs. A2.5 and not already defined are as follows:

$f_o(t_o)dt_o$	Average fraction of each neutron source pulse produced in the time interval dt_o at time t_o (approximated by a gaussian distribution)
n	Sample nuclear density
$\exp\{-\Sigma(E')d'\}$	Flux attenuation factor for energy E' neutrons after moving distance d' through the sample material($\Sigma = n\sigma_T$)
d_i	Distance traveled by a neutron in the sample to the i-th scattering site from the previous site or from the sample face for i=1
d_D	Distance from the final scattering site to the sample face in the direction of the detector
E_i	Neutron energy before the i-th scattering process
θ_i	Angle between the directions of a neutron before and after the i-th scattering process
E_D	Neutron energy at the detector following the final scattering
θ_D	Angle for the final scattering
$\frac{d\sigma_i}{d\Omega}$	Elastic or inelastic differential cross section for the i-th scattering process

In general, the various integration limits for the $N_i(E,\theta,t,\Delta t)$ expressions are fixed by the requirement that the total flight time for neutrons from source to detector fall in

bin Δt at time t. In practice, however, the sample-to-detector distance is much greater than any sample dimension or the source-to-sample distance. This allows the neutron flight time for other that the sample-to-detector distance to be neglected. In that case, all the volume integrations in eq. A2.4 extend over the whole sample or source volumes and the limits of the t_o and E_o integrations are fixed by the requirement that the time-of-flight for a fixed flight distance be within Δt of time t, i.e.,

$$|t - \{t_o + T(E_D)\}| \leq \Delta t. \qquad \text{(A2.6)}$$

Here, $T(E_D)$ is the flight time of energy E_D neutrons from sample to detector and t_o is chosen from the time distribution of the source neutrons.

An expression for the average angle θ in the previous equations may now be given using the symbols defined already.

$$\theta = [\sum_{t=t_1}^{t_2} \int dt_o f(t_o) \int dE_o F_o(E_o) \iiint n_s d^3r_s \iiint n \, d^3r_1 \frac{d\sigma_s}{d\Omega}(E_o, \phi) \, r_{s1}^{-1} \exp\{-\Sigma(E_1) d_1\} \iint d\Omega \frac{d\sigma_1}{d\Omega}(E_1, \theta_1) \exp\{-\Sigma(E_D) d_D\} \varepsilon(E_D) \theta_D] / [\sum_{t=t_1}^{t_2} N_1(E, \theta, t, \Delta t)]. \qquad \text{(A2.7)}$$

The time summations cover the time of arrival of the group of interest at the detector.

Solution Method

Now that terms have been defined, the problem of correcting neutron scattering data may be put precisely. Eqs. A2.1, A2.2, A2.4, and A2.5 express the finite geometry angular distribution (known from experiment) as a function of the point geometry differential cross section near energy E (quantity desired) and total, differential elastic and inelastic cross section values for lower energies (assumed known). The problem is to invert this equation to obtain the point-geometry cross section.

An iterative method has been adopted to perform the calculation. The technique is in large part the same as that of the computer programs used by Kinney[15] and by Velkley et al.[14]. However, modification of the technique was necessary to reflect details of the present experimental conditions. Briefly the method is as follows. The experimental data for the lowest energy is corrected first. It is assumed that elastic (and, if appropriate, inelastic) cross section values are known at all necessary lower energies. Trial corrected elastic and inelastic distributions are assumed. These may be the measured angular distributions; however, angular distributions approximately attenuation corrected using the "disc approximation" of Kinney[15] provide a better trial. This correction estimate is discussed in section III in connection with the polyethylene scatterer, but the generalization to other samples is straightforward.

Monte Carlo calculations simultaneously determine the time-of-flight spectra (A2.4, A2.5) for all experimental detector positions, as well as the average flux (A2.2), energy (A2.3), and scattering angles (A2.7). The details of the Monte Carlo calculations will be outlined below. After spectra have been obtained, the groups of interest are summed over time windows set to correspond to the time windows actually used in reducing the scattering data. Eq. A2.1 is used to convert the sums to angular distributions for comparison with the actual experimental data.

A correction to the trial point-geometry cross section is made angle by angle based upon the ratio of experimental to calculated cross sections and the Monte Carlo calculation is repeated. Iteration continues in this fashion until there is no decrease in a convergence criterion defined as

$$\chi^2 = \sum_{i=1}^{N} \{[\frac{d\sigma_c}{d\Omega}(\theta_i) - \frac{d\sigma_E}{d\Omega}(\theta_i)]/\Delta(\theta_i)\}^2, \qquad (A2.8)$$

where $\frac{d\sigma_E}{d\Omega}$, $\frac{d\sigma_c}{d\Omega}$, and Δ are, respectively, the elastic experimental differential cross section, the calculated differential cross section, and the experimental error. When convergence occurs, the correction factors are taken to be

$$C(E,\theta) = \frac{d\sigma_c}{d\Omega}(E,\theta) / \frac{d\sigma_F}{d\Omega}(E,\theta), \qquad (A2.9)$$

where $\frac{d\sigma_F}{d\Omega}$ is the last trial angular distribution.

Monte Carlo Calculation of Spectra

Some detail of the Monte Carlo programming for the calculation of the time-of-flight spectra and other quantities are of interest. For each program pass, a point $\vec{r}_s$ in the active source volume and a point $\vec{r}_1$ in the sample volume are chosen using a pseudo random number generator. Beam particle energy E_o and time of source reaction t_o are randomly chosen from within gaussian distributions representing experimental conditions. Next the angle of incidence ϕ and energy E_1 at the sample site are calculated. From these and the stored elastic and inelastic cross section values, contributions to the sums pertinent to the calculation of F(E) (A2.2) and E (A2.3) are made. Next, for each type of scattering process, elastic or inelastic, and each experimental detector position, the scattering angle to a randomly chosen point on the detector face θ_D and the energy E_D, efficiency $\varepsilon(E_D)$, and time of arrival t for a neutron at the detector are calculated. These are used to calculate contributions to the sums for the single scattering spectrum (A2.5) and the average scattering angle (A2.7).

At this point in the calculation, a decision is made as to whether a multiple scattering event also will be calculated in the program pass. The decision process is important because it controls the relative accuracy for which the spectra for single, double, triple, and higher-order events will be calculated. What is done is to choose a second point in space lying within a sphere of radius R centered on the first scattering site and enclosing the sample. Its direction in space relative to the first site is chosen randomly, but its distance from that site is picked from an inverse-square distribution. If the new point lies within the sample volume, it is taken as a second scattering site.

A specific type of scattering process is assumed at the first scattering site based upon the relative cross sections for each possibility--elastic or inelastic. Scattering to the second site is calculated and followed by scattering to each detector angle as before. A contribution to the N_2 sum is made. Next, the possibility for an additional scattering process is allowed, and so on. Whenever a newly selected point fails to fall within the sample volume, the current program pass is terminated and a new one is begun at the source.

Some aspects of the selection of next scattering sites are noteworthy. The selection of finite R rather than $R \rightarrow \infty$, as was the case in the codes used by Kinney and Velkley et al., permits the calculation of relatively greater numbers of multiple events. This gives better accuracy on the calculated

correction factors for a given number of analog neutron histories. The small expense of including a "weight" for the probability that the neutron will not escape the sphere of radius R is incurred. Selecting the distance between scattering sites in the sample from an inverse-square distribution, rather than a uniform one, permits one to exclude the d_i^{-2} "weights" appearing in eqs. A2.5. Such weights vary widely over pairs of points in the sample, resulting in poor statistical accuracy on the calculations of multiple scattering events.

Program passes for the calculation of the spectra are run in batches of 1000. Running averages and standard deviations are kept for the sums over the various scattering groups in the calculated spectra. Whenever the standard deviations on the running averages fall below 1% of the average for all detectors, calculation is terminated.

Program Characteristics

The computer program for performing the iterative Monte Carlo technique was coded in the FORTRAN IV language for running on an IBM 370-165 computer. Approximately 250 thousand bytes of storage was required for the program and large elastic and inelastic differential cross section tables containing angular distribution values in .02 steps in the cosine of the scattering angle for up to 80 energies. Run time was approximately 4 min/calculation when the Monte Carlo spectra calcula-

tion required 10,000 program passes to reach the 1% accuracy level. Typically 2 iterations following the initial calculation were required to achieve convergence.

The method described here allowed correction of neutron scattering data for finite geometry and multiple scattering effects to be made with only minor approximations. Improvements over previous, similar codes include improved statistical accuracy in equivalent computer time; use of a vastly increased library of cross section tables in order to calculate various interaction probabilities more exactly; and, most important for use with light elements, the effect of kinematic and Q-value energy losses upon measured spectra is included exactly. As used to correct the present data, the statistical uncertainty on the correction of the data for the effects described was always insignificant compared to other uncertainties inherent in the data.

APPENDIX III

LEGENDRE POLYNOMIAL COEFFICIENTS

The coefficients a_ℓ in the Legendre polynomial series which best describes the present neutron differential cross section data are given in this appendix. Tables A-D contain the coefficients vs. energy from the fits to the ^{6}Li, ^{7}Li, ^{9}Be, and ^{12}C data, respectively.

TABLE A

LEGENDRE POLYNOMIAL COEFFICIENTS FOR
NEUTRON SCATTERING BY ^{6}Li

E_n	7.47	8.96	9.96	10.95	12.04	12.94	13.94
				Elastic			
a_0	87.0	86.9	81.9	81.0	75.7	72.3	74.1
a_1	151.9	164.2	162.3	166.5	161.3	156.8	163.3
a_2	164.0	176.2	175.6	182.7	180.9	174.5	182.6
a_3	110.8	124.1	130.3	138.6	145.7	140.1	145.1
a_4	51.4	54.9	64.3	70.2	82.2	75.7	76.3
a_5	11.5	11.8	19.4	21.0	34.0	27.6	26.6
a_6	6.7	5.1	10.2	8.2	16.6	10.6	8.9
a_7	4.0		5.5		5.8	2.9	1.5
a_8					1.8		
				Inelastic(2.18-MeV state)			
a_0	12.2	10.2	8.5	8.6	7.7	6.3	6.5
a_1	5.6	5.0	3.4	4.0	5.5	4.1	4.2
a_2	-1.5	-1.0	-0.1	-1.7	0.7	0.4	0.8
a_3				-4.4			
a_4				-1.1			

TABLE B

LEGENDRE POLYNOMIAL COEFFICIENTS FOR
NEUTRON SCATTERING BY ^{7}Li

E_n	6.97	7.97	8.96	9.96	10.95	12.04	12.94	13.94
Elastic plus Inelastic(0.478-MeV)								
a_0	132.1	122.4	112.3	108.0	99.5	93.6	90.4	84.7
a_1	183.0	180.8	179.1	187.0	178.2	174.1	177.2	170.5
a_2	208.2	196.1	195.8	199.6	189.2	190.6	193.2	187.6
a_3	147.1	143.3	138.5	152.2	145.4	154.6	156.9	154.5
a_4	56.8	57.0	57.7	65.4	61.8	75.7	77.5	80.2
a_5	5.6	4.9	-0.0	9.0	6.5	19.6	18.9	20.8
a_6	3.4		-1.7	4.3	0.2	9.9	5.6	6.9
Inelastic(4.63-MeV state)								
a_0			16.9	14.7	13.1	11.9	11.0	8.5
a_1			6.4	4.7	5.5	5.4	7.6	4.7

TABLE C

LEGENDRE POLYNOMIAL COEFFICIENTS FOR
NEUTRON SCATTERING BY ^{9}Be

E_n	6.97	7.97	8.96	9.96	10.95	12.04	12.94	13.94
				Elastic				
a_0	93.0	91.8	91.4	90.5	85.1	83.3	81.2	81.1
a_1	169.7	172.4	176.5	182.2	175.2	174.9	175.0	177.5
a_2	195.4	199.2	205.9	212.8	207.1	204.6	206.3	209.8
a_3	142.0	149.5	161.9	172.9	174.2	172.7	177.2	182.6
a_4	54.2	60.9	73.5	85.0	93.5	93.2	100.6	107.9
a_5	11.4	11.3	13.5	20.4	24.9	27.1	32.0	37.5
a_6	2.6	2.6	1.9	5.9	6.7	7.8	9.5	12.0
				Inelastic(2.43-MeV state)				
a_0	24.1	21.6	18.3	18.6	15.2	13.6	11.4	12.1
a_1	6.3	7.4	7.2	9.1	8.3	9.3	7.3	8.8
a_2	-0.0	0.1	-0.6	1.5	1.3	1.7	1.0	1.7
a_3	7.2	5.0	3.6	2.3	-0.4	0.8	1.2	1.2

TABLE D

LEGENDRE POLYNOMIAL COEFFICIENTS FOR
NEUTRON SCATTERING BY ^{12}C

E_n	8.97	9.20	9.56	9.97	10.22	10.69	10.96	11.17
				Elastic				
a_0	52.6	58.4	51.9	50.9	47.9	54.0	68.4	62.9
a_1	47.4	82.2	77.5	80.3	69.0	87.1	129.0	111.1
a_2	65.5	107.3	101.0	100.0	86.3	112.2	163.3	140.5
a_3	95.3	130.4	108.3	105.5	93.1	114.6	154.7	137.0
a_4	24.7	68.6	60.0	49.7	35.8	53.7	85.7	81.2
a_5	-9.4	26.0	15.6	-0.3	-8.0	16.0	29.4	22.7
a_6		6.0		-2.6	-0.8	9.5	8.0	12.4
					0.7	1.9		3.8
				Inelastic(4.44-MeV state)				
a_0	26.6	24.4	27.8	24.6	23.6	29.4	29.1	25.4
a_1	-0.6	-3.2	18.0	20.2	10.2	15.2	18.8	16.9
a_2	20.0	21.9	28.6	13.8	12.4	28.8	35.9	28.8
a_3	7.5	-0.4	7.6	2.8	2.9	13.0	7.0	6.9
a_4	1.8	3.6	0.5	4.6	3.2	4.8	6.2	10.6

TABLE D--Continued

E_n	11.74	11.96	12.49	12.95	13.94	14.43	14.93
				Elastic			
a_0	65.6	72.8	65.4	77.6	72.8	70.6	75.0
a_1	100.8	120.4	96.5	127.0	125.3	118.5	147.3
a_2	126.9	149.9	129.2	162.0	155.9	162.1	178.6
a_3	133.9	161.3	139.5	172.0	156.4	150.9	181.7
a_4	73.7	99.7	84.6	111.2	105.7	123.1	145.7
a_5	21.8	39.5	25.5	49.4	28.8	49.6	68.6
a_6	13.6	15.1	12.9	18.2	18.3	27.9	42.9
a_7	2.7			5.8	4.3	6.0	20.0
a_8							6.8
				Inelastic(4.44-MeV state)			
a_0	21.8	21.1	17.1	20.1	20.1	16.8	13.6
a_1	15.9	19.5	10.5	8.9	9.1	10.5	12.1
a_2	25.0	25.0	19.8	29.4	20.1	22.0	13.9
a_3	7.2	5.7	5.5	7.4	3.3	0.5	0.0
a_4	1.5	1.3	2.3	4.2	-0.4	1.0	-0.6

LIST OF REFERENCES

1. F. O. Purser, D. W. Glasgow, H. H. Hogue, J. C. Clement, G. Mack, K. Stelzer, J. R. Boyce, D. H. Epperson, S. G. Buccino, P. W. Lisowski, S. G. Glendinning, E. G. Bilpuch, H. W. Newson, and C. R. Gould, Nuclear Cross Sections and Technology: Proceedings of a Conference, eds. R. A. Schrack and C. D. Bowman, NBS Special Publication 425, Vol. II (Washington: U. S. Government Printing Office, 1975), p. 866.

2. D. W. Glasgow, F. O. Purser, H. Hogue, J. C. Clement, K. Stelzer, G. Mack, J. R. Boyce, D. H. Epperson, S. G. Buccino, P. W. Lisowski, S. G. Glendinning, E. G. Bilpuch, H. W. Newson, and C. R. Gould, Nucl. Sci. Engineer. 61 (1976) 521.

3. F.D. Becchetti, Jr. and G.W. Greenlees, Phys. Rev. 182 (1969) 1190.

4. C.M. Perey and F.G. Perey, Atomic Data and Nucl Data Tables 13 (1974) 293.

5. R.A. Watson, P.P. Singh, and R.F. Segel, Phys. Rev. 182 (1969) 977.

6. Taro Tamura, Revs. Mod. Phys. 37 (1965) 679.

7. Taro Tamura, "Computer Program Jupitor-I for Coupled-Channel Calculations," Oak Ridge National Laboratory Report No. ORNL-4152, 1967.

8. H. W. Newson, E. G. Bilpuch, F. O. Purser, J. R. Boyce, and T. B. Clegg, Nucl. Instr. Meth. 122 (1974) 99.

9. D.W. Glasgow, D.E. Velkley, J.D. Brandenberger, M.T. McEllistrem, G.I. Harries, H.J. Hennecke, D.B. Brertenbecher, C.P. Poirier, J.C. Manthuruthie, W.A. Anderson, A.K. Hyder, Jr. and M.D. Centala, Nucl. Instr. Meth. 114 (1974) 541.

10. D.W. Glasgow, F.O. Purser, J.C. Clement, G. Mack, K. Stelzer, J.R. Boyce, D.H. Epperson, H.H. Hogue, E.G. Bilpuch, H.W. Newson, and C.R. Gould, Nuclear Cross Sections and Technology: Proceedings of a Conference, eds. R.A. Schrack and C.D. Bowman, NBS

Special Publication 425, Vol. I(Washington: U.S. Government Printing Office, 1975) p. 99.

11. J. C. Hopkins and G. Breit, Nucl. Data Tables A9(1971)137.

12. G. L. Morgan, Oak Ridge National Laboratory, private communication.

13. R. E. Textor and V. V. Verbinski,"05S: A Monte Carlo Code for Calculating Pulse-Height Distributions Due to Monoenergetic Neutrons Incident on Organic Scintillators," Oak Ridge National Laboratory Report no. ORNL-4160,1968.

14. D.E. Velkley, J.D. Brandenberger, D.W. Glasgow, and M.T. McEllistrm, Nucl. Instr. Meth. 129(1975)231.

15. W.E. Kinney, Nucl. Instr. Meth. 83(1970)15.

16. C.A. Engelbrecht, Nucl. Instr. Meth. 93(1971)103.

17. C.A. Engelbrecht, Nucl. Instr. Meth. 80(1970)187.

18. S.A. Cox, Nucl. Instr. Meth. 56(1970)245.

19. W. P. Bucher and C. E. Hollandsworth, U. S. Army Ballistics Research Laboratories, Aberdeen Proving Ground, Maryland, unpublished; C. E. Hollandsworth, private communication.

20. G. C. Wick, Atti Acad. d'Ital.13(1943) 1203.

21. Leona Stewart, Los Alamos National Laboratory, private communication.

22. G. Haouat, J. Lachkar, J. Sigaud, Y. Patin, and F. Cocu, "Differential Cross section Measurements for Carbon Neutron Elastic and Inelastic Scattering from 8.0 to 14.5 MeV," Physique Nucleaire Center d'Etudes de Bruyeres-le-Chatel, France, to be published.

23. R.J. Eastgate, W.J. Thompson, and R.A. Hardekoff Computer Phys. Commun. 5(1973)69.

24. P. Schwandt, Nuclear Physics Laboratory, Indiana University (TUNL version by E.-H. Choi and W.J. Thompson, Department of Physics, University of North Carolina at Chapel Hill).

25. Harold Knox, Roger White, and R. O. Lane, University of Ohio Accelerator Laboratory, to be published; Harold Knox, private communication.

26. J.K. Dickens, T.A. Love, and G.L. Morgan, "Gamma-Ray Production due to Neutron Interactions with Fluorine and Lithium for Incident Neutron Energies between 0.55 and 20 MeV: Tabulated Differential Cross Sections," Oak Ridge National Laboratory Report No. ORNL-TM-4538, 1974.

27. H.J. Votava, T.B. Clegg, C.J. Ludwig, and W.J. Thompson, Nucl. Phys. A 204 (1973) 529.

28. H.J. Votava, "Proton Scattering for ^{9}Be Between 6 and 30 MeV," Ph.D. dissertation, University of North Carolina at Chapel Hill, 1972.

29. F. G. Perey, Phys. Rev. 131 (1963) 745.

30. J. S. Nodvik, C. B. Duke, and M. A. Melkanoff, Phys. Rev. 125 (1962) 975.

31. Robert W. Peele, Phys. Rev. 105 (1957) 1312.

32. H.C. Lee and R.Y. Cusson, Ann. Phys. 72 (1972) 353.

33. H. Reber and G. W. Schweimer, "Improved Version of Tamura's Code for Coupled Channel Calculation: Jupitor Karlsruhe Version," Kernforschungzentrum Karlsruhe Report No. KFK-1333, 1970.

34. C.A. Grin, C. Joseph, C.Y. Wong and T. Tamura, Phys. Lett. 25B (1967) 387.

35. V.A. Madsen, V.R. Brown, and J.D. Anderson, Rev. Phys. Lett. 34 (1975) 1398.

36. W.J. Thompson, University of North Carolina at Chapel Hill, private communication.

37. J. Lachkar, M. T. McEllistrem, G. Haouat, Y. Patin, J. Sigaud, and F. Cocu, Phys. Rev. C (1976) 933.

38. M. Drosg and D.M. Drake, "Absolute Differential Cross Sections for Neutron Production by the ^{2}H(d,n)^{3}He Reaction with E from 6 to 17 MeV and by the ^{3}H(p,n)^{3}He Reaction with E from 6 to 16 MeV," Los Alamos Scientific Laboratory Report No. LA-5732-MS, 1974.

39. Nelson Jarmie and J.H. Jett, Phys. Rev. C 16 (1977) 15 and private communication.